Coastline Mapping and Change Detection Using One-Meter Resolution Satellite Imagery

Ron Li
The Ohio State University

Ohio Sea Grant College Program
Technical Bulletin Series
Publication OSHU-TB-037
1999

Ohio Sea Grant College Program
The Ohio State University
1314 Kinnear Road
Columbus, Ohio 43212-1194
614/292-8949
Fax: 614/292-4364

www.sg.ohio-state.edu/

This publication (OHSU-TB-037) is a result of work that was supported, in part, by the Ohio Sea Grant College Program (project R/NP-1) from the National Oceanic and Atmospheric Administration (NOAA grant NA46RG0482), U.S. Department of Commerce. Support is also provided by the Ohio Board of Regents, The Ohio State University, Ohio State University Extension, and participating universities. The Ohio Sea Grant College Program is administered by The Ohio State University.

COASTLINE MAPPING AND CHANGE DETECTION USING ONE-METER RESOLUTION SATELLITE IMAGERY

Annual Project Report

(March – December 1998)

Submitted to

Sea Grant / NOAA

By

Principal Investigator: Dr. Ron Li
Researchers: Dr. G. Zhou, A. Gonzalez, J.-K. Liu, Dr. F. Ma and Y. Felus

Department of Civil & Environmental Engineering and Geodetic Science
The Ohio State University

Co-PIs
L. Lapine, National Geodetic Survey, NOAA
M. Lockwood, Office of Coastal Survey, NOAA
N. J. Schmidt and C. Fowler, Coastal Service Center, NOAA

December 1998

Table of Contents

PART II. GIS AND SPATIAL ANALYSIS

Coastline Mapping and Change Detection Using One-Meter Resolution Satellite Imagery

1. Introduction

1.1 Project summary

The project started in March 1998 and will last for two years. This project report covers the period of March – December 1998. The project is on schedule and has produced a significant progress in the reported period, which includes

- A journal paper published in Photogrammetric Engineering and Remote Sensing (Li 1998),
- An oral presentation at Symposium of Commission III of the International Society of Photogrammetry and Remote Sensing, July 6 - 10, 1998, Columbus, Ohio,
- Two Master of Science theses on the project research topic (Gonzalez 1998, Liu 1998),
- Development of a software system for simulating high-resolution satellite imagery,
- Development of the first version of a photogrammetric bundle adjustment system for processing one-meter resolution satellite imagery,
- Completion of DGPS survey of the test range at Madison County, Ohio for testing the new one-meter resolution satellite imagery capability, and
- Completion of tests of the developed software using two data sets, one from an airborne hyperspectral High Resolution Stereo Cameras (HRSC) developed by Germany Space Agency (DLR), and the other from the German MOMS-02P system on board of Russian Space Station MIR. Both systems are three-line sensor system similar to the one-meter resolution satellite sensor IKONOS-I of SpaceImaging in US.

The above project achievement guarantees a basis for the research in the second project year.

Project members are

Principal Investigator: Dr. Ron Li

Post-doctoral fellow: Dr. G. Zhou and F. Ma

Graduate assistants: Y. Felus and Z. Tu

Graduate students: A. Gonzalez and J.-K. Liu (thesis research based on the project research topic and data)

1.2 Background

As populations and economic activities increase in coastal zones, coastline mapping and coastline change detection become critical to safe navigation, coastal resource management, coastal environmental protection, and sustainable coastal development and planning. An investigation into interrelationships among various causes and impacts of coastline changes is necessary before any objective and scientific decisions related to coastal zone policies, engineering projects, and coastal management can be made. Coastline mapping/monitoring and GIS spatial analysis are key technologies for such as investigations.

Coastline mapping is traditionally carried out by using conventional field surveying methods. Recent development in Global Positioning Systems (GPS) technology has stimulated a great interest in its application in large-scale coastline mapping. Land vehicle based mobile mapping technology uses GPS receivers and a beach vehicle to trace water marks along the coastlines (Shaw and Allen 1995 and Li 1997). Aerial photogrammetry and LIDAR (Light Direction and Ranging) depth data have been used to map regional and national coastlines (Slama et al. 1980, Ingham 1992). GPS technology has also been applied to provide orientation information to enhance aerial photogrammetric triangulation (Lapine 1991, Merchant 1994 and Bossler 1996).

The new generation of commercial one-meter resolution satellite imagery will open a new era for digital mapping (Fritz 1996, Li 1998). Several American companies scheduled launches of their high-resolution satellites, for example EarlyBird (3m resolution, launched in early 1998 and failed two-way communication) and QuickBird (1m/4m) from EarthWatch Inc. and OrbView-1 (1m/2m) of Orbital Science Corporation. SpaceImaging EOSAT announced that IKONOS-1 (1 meter) was going to be launched from California's Vandenburg Air Force Base at the end of 1998. We were able to access digital imagery of HRSC (10cm) from German Space Agency and MOMS-02P (17meter) from German Space Agency.

It is expected that IKONOS-I will provide an absolute planimetric accuracy of 12m and a vertical accuracy of 8m without ground control points (GCPs). With the addition of GCPs, the system can reach a planimetric accuracy of 2m and a vertical accuracy of 3m. This level of accuracy is considered sufficient to support the generation of most national mapping products (Li 1998). The geometry of three-line sensors that is also used by most commercial high-resolution satellite imaging systems has been researched by a few researchers. Ebner et al. (1991) simulated geometry and estimated accuracy of MOMS-02/D2. Ebner and Strunz (1988) investigated the accuracy of obtained ground points using a DTM as control information. Ebner et al. (1992) finished their simulation study on influences of the precision of observed exterior orientation parameters, the type and density of GCPs, camera inclination across flight direction, and simultaneous adjustment of two crossing strips with different intersection angles on the theoretical accuracy of the point determination. The desired height accuracy of about 5m can be achieved by the simultaneous adjustment of two (or more) crossing strips within the overlapping area. Fraser and Shao (1996) did similar work evaluating the accuracy of ground points when employing different control point configurations, numbers of orientation images and orders of interpolation functions using a control field in Australia. Habib and Beshah (1997) did their simulation study for an airborne Panoramic Linear Array Scanner. They concentrated on evaluating the effects of different numbers of GCP's and different combinations of images. Fritsch et al. (1998) reported their recent result of processing MOMS-02P data that supplies similar accuracy as MOMS-02/D2.

1.3 Organization of the report

This report presents technical approaches and achievements of the following aspects:

Part I. Data processing for coastline mapping

- Extended mathematical model for bundle adjustment of three-line sensor data including imagery, GPS/INS data, and GCPs and checkpoints.
- DGPS survey for acquiring geodetic coordinates of GCPs, which includes control field design and landmark layout, GPS field surveying, data processing and accuracy evaluation.
- Simulation of IKONOS-I mapping geometry to estimate attainable geometric accuracy and to give recommendations on various configurations for ground point determination.
- Development of the first version of bundle adjustment software for the extended model.

- Processing of HRSC and MOMS-02P data.

Part II. GIS and spatial analysis

- Discussion of data types and transformation and conversion needed in order to handle the data.
- Procedures developed to analyze erosion, coastline changes, and predict future coastline positions.
- Concepts and preliminary analysis results of erosion causes and their relationships.

PART I. DATA PROCESSING FOR COASTLINE MAPPING

2. Photogrammetric Model of Bundle Adjustment for IKONOS-I

2.1 Some metric characteristics of IKONOS-I

The geometric configuration of IKONOS-I is depicted in Figure 1. It applies the push-broom principle. A single linear array is mounted in the focal plane of a lens with a 10m focal length, which is orthogonal to the direction of flight. In the push-broom imaging mode, a continuous succession of the one-dimensional image is electronically sampled in such as way that an entire linear array is read out during the integration time. Travelling at 7 km per second with an altitude of 680 km, the IKONOS-I pitches forward 26° and begins collecting data. It then pitches to nadir and collected data over the same ground area. After collection at nadir, the satellite pitches aft at 26° and collects the same area for the third time (Parker 1997). Such a configuration provides a so-called in-track stereo model. Stereo pairs created from fore-, nadir-, and aft-looking ensure high quality collections because images are acquired in almost same ground and atmospheric conditions. The stereo imaging collections cover a swath approximately 11 km wide. Stereo pairs have a convergence angle of 26° or 52°.

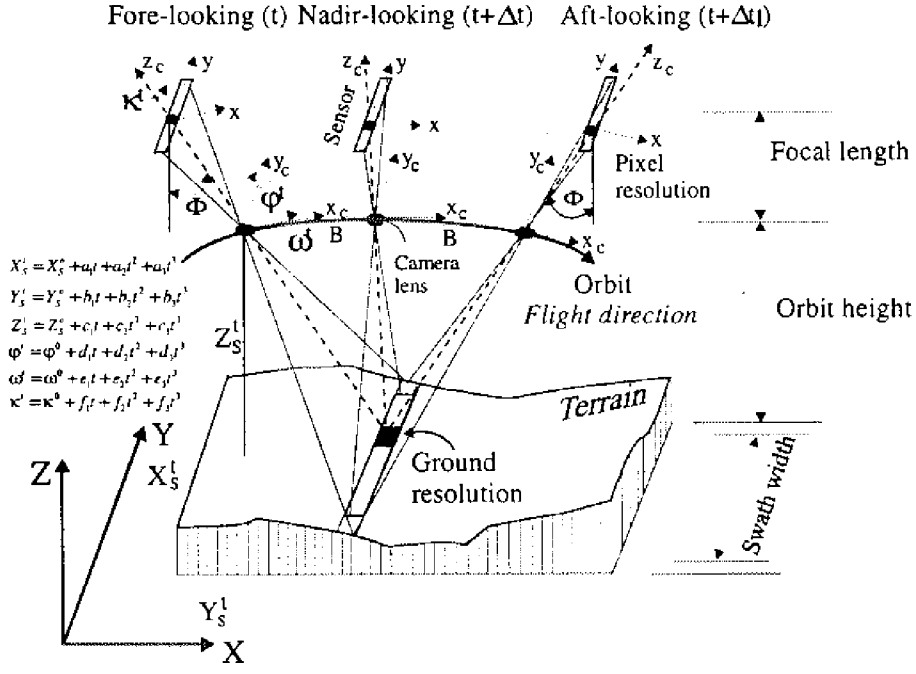

Figure 1. Geometric imaging configuration of IKONOS-I

The imaging geometry of IKONOS-I is similar to those of other push-broom scanners such as space-borne MOMS-02/D2 and MOMS-2P or airborne HRSC that implemented real three-line stereo geometry. The perspective geometry is only valid on the sensor line. Special characters of IKONOS-I, in comparison to other similar systems, are:

- This system is based on a new optical system: a push-broom camera with a very long focal length (10m), which is folded to two meters through the use of a mirror system. It was designed to capture both panchromatic images with one-meter resolution and multispectral images with four-meter resolution. The multispectral bands are listed in Table 1.
- In addition to along-track stereo capability, the satellite will be able to pivot in orbit to collect cross-track images at distance of 725km on either side of the ground track. Due to the satellite's 680km altitude, imagery will maintain at least a one-meter ground sample distance (GSD) with 350km for either side of nadir (Corbley 1996).
- The system is equipped with GPS antennas and three digital star trackers to maintain precise camera position and attitude. A rigid satellite platform was built to reduce the motion vibration of the platform and to contribute to the integrity of the line-of-sight determination. The satellite will revolve around the Earth in a sun synchronous polar orbit, which will allow it to traverse the planet every 98 minutes, crossing the equator at the same time (around 10.30 am) in every orbit (Folchi 1996).

Parameters	**Panchromatic**	**Multispectral**
Resolution (Nadir GSD)	0.82m	4m
Spectral bandwidth (μm)	0.45-0.9	0.45-0.52
		0.52-0.60
		0.63-0.69
		0.76-0.90

Table 1. Bandwidths of IKONOS-I (Fritz 1996)

2.2 Photogrammetric Model of Bundle Adjustment for Linear Array CCD Sensors

2.2.1 Interior orientation

Interior orientation transforms screen coordinates (i and j in Figure 2) into image coordinates (x and y in Figure 3), and corrects for lens distortion (symmetric and tangential) and CCD array curvature distortion. Thus the following tasks should be performed.

- Define the screen coordinate system and image coordinate systems,
- Apply the principal offset that should be estimated from a laboratory or in-flight based calibration, and
- Correct various distortions.

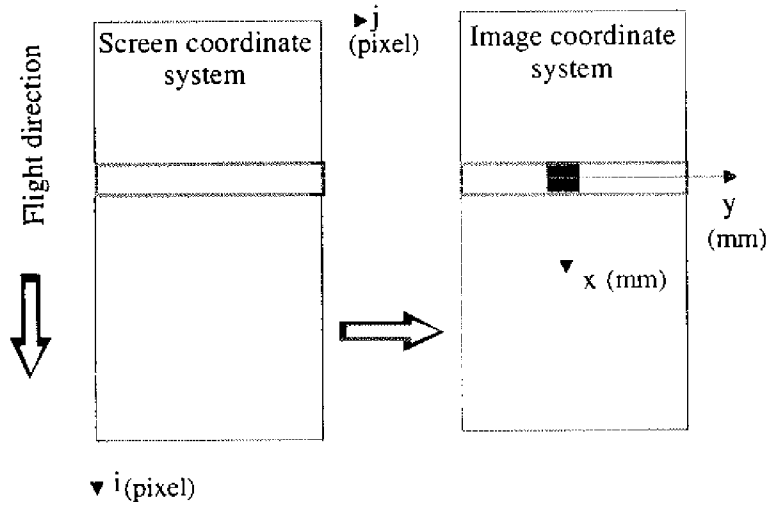

Figure 2. Screen and image coordinate system

2.2.2 Transformation from image to reference coordinate system

Each of the fore-, nadir- and aft-looking array has its own image coordinate system (x_c, y_c and z_c, right-handed). An image reference coordinate system (x_R, y_R and z_R, right-handed) is defined to unify image coordinates from all three arrays. The transformation from an image coordinate system to the reference coordinate system involves a translation (dx, dy, dz) and three rotations (ω, ϕ, κ) (Figure 3). We define a counterclockwise rotation angle as positive.

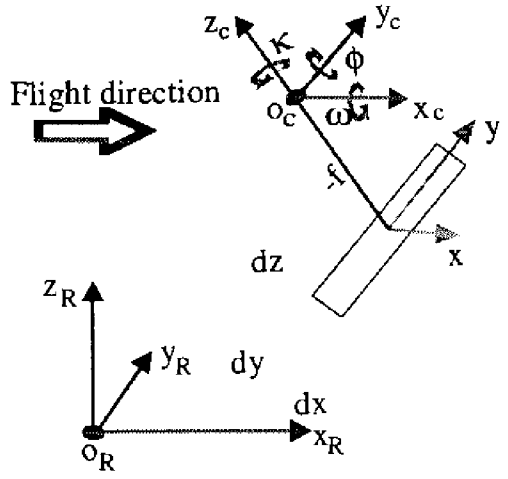

Figure 3. From image coordinate to image reference coordinate system

The transformation equation is

$$\begin{pmatrix} x_R \\ y_R \\ z_R \end{pmatrix} = R_c^R \begin{pmatrix} x_c \\ y_c \\ z_c \end{pmatrix} + \begin{pmatrix} dx \\ dy \\ dz \end{pmatrix} \tag{1}$$

where

$$\begin{pmatrix} x_c \\ y_c \\ z_c \end{pmatrix} = \begin{pmatrix} x \\ y \\ -f \end{pmatrix} \tag{2}$$

$$R_c^R = \begin{pmatrix} \cos\varphi\cos k & \cos\omega\sin k + \sin\omega\sin\varphi\cos k & \sin\omega\sin k - \cos\omega\sin\varphi\cos k \\ -\cos\varphi\sin k & \cos\omega\cos k - \sin\omega\sin\varphi\sin k & \sin\omega\cos k + \cos\omega\sin\varphi\sin k \\ \sin\varphi & -\sin\omega\cos\varphi & \cos\omega\cos\varphi \end{pmatrix} \tag{3}$$

R_c^R is an orthogonal matrix, i.e. $(R_R^c)^T = (R_R^c)^{-1}$.

2.2.3 Collinearity equations

For any image point within a CCD array, its image reference coordinates are (x_R, y_R, z_R). The coordinates of the exposure center of the array in the ground coordinate system at the imaging epoch t

are ($X_s(t)$, $Y_s(t)$, $Z_s(t)$). The corresponding ground point coordinates are (X_G, Y_G, Z_G). The collinearity condition states that all these three points must be on the same line:

$$x_R = z_R \frac{r_{11}(X_G - X_S(t)) + r_{12}(Y_G - Y_S(t)) + r_{13}(Z_G - Z_S(t))}{r_{31}(X_G - X_S(t)) + r_{32}(Y_G - Y_S(t)) + r_{33}(Z_G - Z_S(t))}$$

$$y_R = z_R \frac{r_{21}(X_G - X_S(t)) + r_{22}(Y_G - Y_S(t)) + r_{23}(Z_G - Z_S(t))}{r_{31}(X_G - X_S(t)) + r_{32}(Y_G - Y_S(t)) + r_{33}(Z_G - Z_S(t))} \quad (4)$$

where R_G^R is a rotation matrix from the ground coordinate system to the reference coordinate system and is defined by

$$R_G^R = \begin{pmatrix} \cos\varphi\cos k & \cos\omega\sin k + \sin\omega\sin\varphi\cos k & \sin\omega\sin k - \cos\omega\sin\varphi\cos k \\ -\cos\varphi\sin k & \cos\omega\cos k - \sin\omega\sin\varphi\sin k & \sin\omega\cos k + \cos\omega\sin\varphi\sin k \\ \sin\varphi & -\sin\omega\cos\varphi & \cos\omega\cos\varphi \end{pmatrix} \quad (5)$$

The rotation angles $\varphi(t)$, $\omega(t)$ and $k(t)$ are defined for each CCD array at the epoch t. Depending on types of observations, coordinates and parameters may be treated as knowns and unknowns differently in various situations.

2.2.4 Navigation data as exterior orientation parameters

IKONOS-I carries navigation equipment of GPS receivers and star trackers that can provide positions (X_s, Y_s, Z_s) and attitudes (ω, ϕ, κ) of the CCD arrays if appropriate calibrations are performed. Since the navigation data have lower data collection rate, they are not acquired for every image line. Those lines with the navigation data are called Orientation Lines (OLs). Exterior orientation parameters of OLs are introduced at certain time intervals. Navigation data at OLs can be used as their exterior orientation parameters. Previous investigations based on simulated orbit data showed that a 3rd order polynomial function can exactly approximate exterior orientation parameter changes (Wu 1986, Ebner et al. 1992). Exterior orientation parameters of lines between OLs are computed by a polynomial interpolation:

$$X_S(t) = a_0 + a_1 t + a_2 t^2 + a_3 t^3$$

$$Y_S(t) = b_0 + b_1 t + b_2 t^2 + b_3 t^3$$

$$Z_S(t) = c_0 + c_1 t + c_2 t^2 + c_3 t^3$$

$$\varphi_S(t) = d_0 + d_1 t + d_2 t^2 + d_3 t^3$$

$$\omega_S(t) = e_0 + e_1 t + e_2 t^2 + e_3 t^3$$

$$\kappa_S(t) = f_0 + f_1 t + f_2 t^2 + f_3 t^3 \qquad (6)$$

The parameter t may be time beginning at a certain epoch or image line number from a certain orbit position. All three images will be referenced to the same t. The unknown coefficients in Equation (6) can be determined either independently or in a bundle adjustment.

2.2.5 Observation equations

At this time we assume that the interior orientation parameters are available, for example, from calibration. Observations include GCPs, checkpoints, unknown ground points, and navigation data.

GCPs

GCPs have known ground coordinates and measured image coordinates. Unknowns include exterior orientation parameters, that means, coefficients of the polynomials of Equation (6). After linearization of Equation (4), we have the linearized equations

$$\begin{aligned} v_{GCP}^{x} = {} & \beta_{11} da_0 + \beta_{12} db_0 + \beta_{13} dc_0 + \beta_{14} dd_0 + \beta_{15} de_0 + \beta_{16} df_0 + \\ & \beta_{17} da_1 + \beta_{18} db_1 + \beta_{19} dc_1 + \beta_{110} dd_1 + \beta_{111} de_1 + \beta_{112} df_1 + \\ & \beta_{113} da_2 + \beta_{114} db_2 + \beta_{115} dc_2 + \beta_{116} dd_2 + \beta_{117} de_2 + \beta_{118} df_2 + \\ & \beta_{119} da_3 + \beta_{120} db_3 + \beta_{121} dc_3 + \beta_{122} dd_3 + \beta_{123} de_3 + \beta_{124} df_3 + l_{GCP}^{x} \end{aligned}$$

$$\begin{aligned} v_{GCP}^{y} = {} & \beta_{21} da_0 + \beta_{22} db_0 + \beta_{23} dc_0 + \beta_{24} dd_0 + \beta_{25} de_0 + \beta_{26} df_0 + \\ & \beta_{27} da_1 + \beta_{28} db_1 + \beta_{29} dc_1 + \beta_{210} dd_1 + \beta_{211} de_1 + \beta_{212} df_1 + \\ & \beta_{213} da_2 + \beta_{214} db_2 + \beta_{215} dc_2 + \beta_{216} dd_2 + \beta_{217} de_2 + \beta_{218} df_2 + \\ & \beta_{219} da_3 + \beta_{220} db_3 + \beta_{221} dc_3 + \beta_{222} dd_3 + \beta_{223} de_3 + \beta_{224} df_3 + l_{GCP}^{y} \end{aligned} \qquad (7)$$

where

$$l_{GCP}^{x} = -x_R + z_R \frac{r_{11}(X_G - X_S^0(t)) + r_{12}(Y_G - Y_S^0(t)) + r_{13}(Z_G - Z_S^0(t))}{r_{31}(X_G - X_S^0(t)) + r_{32}(Y_G - Y_S^0(t)) + r_{33}(Z_G - Z_S^0(t))}$$

$$l_{GCP}^{y} = -y_R + z_R \frac{r_{21}(X_G - X_S^0(t)) + r_{22}(Y_G - Y_S^0(t)) + r_{23}(Z_G - Z_S^0(t))}{r_{31}(X_G - X_S^0(t)) + r_{32}(Y_G - Y_S^0(t)) + r_{33}(Z_G - Z_S^0(t))}$$

The coefficients β_{11} to β_{224} are partial derivatives of Equation (4) with respect to the polynomial parameters and are defined in Appendix I.

Unknown ground points and check points

For unknown ground points we want to measure the image points and to estimate the ground coordinates through the bundle adjustment. In cases of checkpoints, we measure image coordinates and calculate ground coordinates in order to compare to the calculated and known ground coordinates. Compared to GCPs, the additional unknowns are the ground coordinates.

$$
\begin{aligned}
v_M^x = {} & \gamma_{11}da_0 + \gamma_{12}db_0 + \gamma_{13}dc_0 + \gamma_{14}dd_0 + \gamma_{15}de_0 + \gamma_{16}df_0 + \\
& \gamma_{17}da_1 + \gamma_{18}db_1 + \gamma_{19}dc_1 + \gamma_{110}dd_1 + \gamma_{111}de_1 + \gamma_{112}df_1 + \\
& \gamma_{113}da_2 + \gamma_{114}db_2 + \gamma_{115}dc_2 + \gamma_{116}dd_2 + \gamma_{117}de_2 + \gamma_{118}df_2 + \\
& \gamma_{119}da_3 + \gamma_{120}db_3 + \gamma_{121}dc_3 + \gamma_{122}dd_3 + \gamma_{123}de_3 + \gamma_{124}df_3 + \\
& \gamma_{125}dX + \gamma_{126}dY + \gamma_{127}dZ + l_M^x \\
v_M^y = {} & \gamma_{21}da_0 + \gamma_{22}db_0 + \gamma_{23}dc_0 + \gamma_{24}dd_0 + \gamma_{25}de_0 + \gamma_{26}df_0 + \\
& \gamma_{27}da_1 + \gamma_{28}db_1 + \gamma_{29}dc_1 + \gamma_{210}dd_1 + \gamma_{211}de_1 + \gamma_{212}df_1 + \\
& \gamma_{213}da_2 + \gamma_{214}db_2 + \gamma_{215}dc_2 + \gamma_{216}dd_2 + \gamma_{217}de_2 + \gamma_{218}df_2 + \\
& \gamma_{219}da_3 + \gamma_{220}db_3 + \gamma_{221}dc_3 + \gamma_{222}dd_3 + \gamma_{223}de_3 + \gamma_{224}df_3 + \\
& \gamma_{225}dX + \gamma_{226}dY + \gamma_{227}dZ + l_M^y
\end{aligned}
\tag{8}
$$

where

$$
l_M^x = -x_M + z_R \frac{r_{11}(X - X_S(t)) + r_{12}(Y - Y_S(t)) + r_{13}(Z - Z_S(t))}{r_{31}(X - X_S(t)) + r_{32}(Y - Y_S(t)) + r_{33}(Z - Z_S(t))}
$$

$$
l_M^y = -y_M + z_R \frac{r_{21}(X - X_S(t)) + r_{22}(Y - Y_S(t)) + r_{23}(Z - Z_S(t))}{r_{31}(X - X_S(t)) + r_{32}(Y - Y_S(t)) + r_{33}(Z - Z_S(t))}
$$

Similarly, the coefficients γ_{11} to γ_{227} are explained in Appendix I.

Navigation data as observations

The exposure center coordinates at OLs from GPS can be treated as observations:

$$
\begin{pmatrix} v_{GPS}^{X_1} \\ v_{GPS}^{X_2} \\ \vdots \\ v_{GPS}^{X_{N_3}} \end{pmatrix} = \begin{pmatrix} 1 & t_1 & t_1^2 & t_1^3 \\ 1 & t_2 & t_2^2 & t_2^3 \\ & & \vdots & \\ 1 & t_{N_3} & t_{N_3}^2 & t_{N_3}^3 \end{pmatrix} \begin{pmatrix} da_0 \\ da_1 \\ da_2 \\ da_3 \end{pmatrix} + \begin{pmatrix} X_S^0(t_1) - X_{GPS}^1 \\ X_S^0(t_2) - X_{GPS}^2 \\ \vdots \\ X_S^0(t_{N_3}) - X_{GPS}^{N_3} \end{pmatrix}
$$

$$
\begin{pmatrix} v_{GPS}^{Y_1} \\ v_{GPS}^{Y_2} \\ \vdots \\ v_{GPS}^{Y_{N_3}} \end{pmatrix} = \begin{pmatrix} 1 & t_1 & t_1^2 & t_1^3 \\ 1 & t_2 & t_2^2 & t_2^3 \\ & & \vdots & \\ 1 & t_{N_3} & t_{N_3}^2 & t_{N_3}^3 \end{pmatrix} \begin{pmatrix} db_0 \\ db_1 \\ db_2 \\ db_3 \end{pmatrix} + \begin{pmatrix} Y_S^0(t_1) - Y_{GPS}^1 \\ Y_S^0(t_2) - Y_{GPS}^2 \\ \vdots \\ Y_S^0(t_{N_3}) - Y_{GPS}^{N_3} \end{pmatrix}
$$

$$
\begin{pmatrix} v_{GPS}^{Z_1} \\ v_{GPS}^{Z_2} \\ \vdots \\ v_{GPS}^{Z_{N_3}} \end{pmatrix} = \begin{pmatrix} 1 & t_1 & t_1^2 & t_1^3 \\ 1 & t_2 & t_2^2 & t_2^3 \\ & & \vdots & \\ 1 & t_{N_3} & t_{N_3}^2 & t_{N_3}^3 \end{pmatrix} \begin{pmatrix} dc_0 \\ dc_1 \\ dc_2 \\ dc_3 \end{pmatrix} + \begin{pmatrix} Z_S^0(t_1) - Z_{GPS}^1 \\ Z_S^0(t_2) - Z_{GPS}^2 \\ \vdots \\ Z_S^0(t_{N_3}) - Z_{GPS}^{N_3} \end{pmatrix} \tag{9}
$$

Also, observations for rotation angles are

$$
\begin{pmatrix} v_{INS}^{\varphi_1} \\ v_{INS}^{\varphi_2} \\ \vdots \\ v_{INS}^{\varphi_{N_3}} \end{pmatrix} = \begin{pmatrix} 1 & t_1 & t_1^2 & t_1^3 \\ 1 & t_2 & t_2^2 & t_2^3 \\ & & \vdots & \\ 1 & t_{N_3} & t_{N_3}^2 & t_{N_3}^3 \end{pmatrix} \begin{pmatrix} dd_0 \\ dd_1 \\ dd_2 \\ dd_3 \end{pmatrix} + \begin{pmatrix} \varphi_S^0(t_1) - \varphi_{INS}^1 \\ \varphi_S^0(t_2) - \varphi_{INS}^2 \\ \vdots \\ \varphi_S^0(t_{N_3}) - \varphi_{INS}^{N_3} \end{pmatrix}
$$

$$
\begin{pmatrix} v_{INS}^{\omega_1} \\ v_{INS}^{\omega_2} \\ \vdots \\ v_{INS}^{\omega_{N_3}} \end{pmatrix} = \begin{pmatrix} 1 & t_1 & t_1^2 & t_1^3 \\ 1 & t_2 & t_2^2 & t_2^3 \\ & & \vdots & \\ 1 & t_{N_3} & t_{N_3}^2 & t_{N_3}^3 \end{pmatrix} \begin{pmatrix} de_0 \\ de_1 \\ de_2 \\ de_3 \end{pmatrix} + \begin{pmatrix} \omega_S^0(t_1) - \omega_{INS}^1 \\ \omega_S^0(t_2) - \omega_{INS}^2 \\ \vdots \\ \omega_S^0(t_{N_3}) - \omega_{INS}^{N_3} \end{pmatrix}
$$

$$
\begin{pmatrix} v_{INS}^{k_1} \\ v_{INS}^{k_2} \\ \vdots \\ v_{INS}^{k_{N_3}} \end{pmatrix} = \begin{pmatrix} 1 & t_1 & t_1^2 & t_1^3 \\ 1 & t_2 & t_2^2 & t_2^3 \\ & & \vdots & \\ 1 & t_{N_3} & t_{N_3}^2 & t_{N_3}^3 \end{pmatrix} \begin{pmatrix} df_0 \\ df_1 \\ df_2 \\ df_3 \end{pmatrix} + \begin{pmatrix} k_S^0(t_1) - k_{INS}^1 \\ k_S^0(t_2) - k_{INS}^2 \\ \vdots \\ k_S^0(t_{N_3}) - k_{INS}^{N_3} \end{pmatrix} \tag{10}
$$

All these heterogeneous data of position and attitude should combine into equations 8 and 9 after being transformed into a common coordinate system.

2.2.6 Weights

The weight of the i-th observation is defined as

$$p_i = \sigma_o^2 / \sigma_i^2 \tag{11}$$

where σ_0^2 is unit weight variance and σ_i^2 is variance of the i-th observation. Assume that we take the variance of image coordinates as σ_0^2, it is about 0.5 pixel. σ_i^2 changes with types of observations and imaging systems. For IKONOS-I, σ_0^2 corresponds to 6μm. If the variance of exposure center is $9m^2$ and that of rotation angles is 4 (arc second)^2, the weights are

Image coordinate of GCP: $p_i^{GCP} = \dfrac{0.006^2(mm^2)}{0.006^2(mm^2)} = 1.0$

Image coordinate of checkpoint: $p_i^{M} = \dfrac{0.001^2(mm^2)}{0.001^2(mm^2)} = 1.0$

Orbit coordinate of OL: $p_i^{GPS} = \dfrac{0.006^2(mm^2)}{3.0^2(m^2)} = 4.0e-6\,(mm^2/m^2)$

Rotation angle of OL: $p_i^{\omega,\phi,\kappa} = \dfrac{0.006^2(mm^2)}{2^2(Sec^2)} = 117\,(mm^2/\deg^2)$

The weights should be updated by variances computed in each iteration of the adjustment.

2.2.7 Adjustment computation

Observation equations

Suppose that we have N_1 OLs, N_2 GCPs, and N_3 unknown/check points. One stereo pair is considered. The observation equations are

Navigation data

$$\underset{3N_1\times 1}{V_{GPS}} = \underset{3N_1\times(24+3N_3)}{A_1} \cdot \underset{(24+3N_3)\times 1}{\delta X} + \underset{3N_1\times 1}{L_1} \qquad \underset{3N_1\times 3N_1}{P_1^{GPS}}$$

$$\underset{3N_1\times 1}{V_{\omega,\phi,\kappa}} = \underset{3N_1\times(24+3N_3)}{A_2} \cdot \underset{(24+3N_3)\times 1}{\delta X} + \underset{3N_1\times 1}{L_2} \qquad \underset{3N_1\times 3N_1}{P_2^{INS}}$$

GCPs

$$V_{GCP}_{4N_2\times 1} = A_{3}_{4N_2\times(24+3N_3)} \cdot \delta X_{(24+3N_3)\times 1} + L_{3}_{4N_2\times 1} \qquad P_{3}^{GCP}_{4N_2\times 4N_2}$$

Unknown/check points

$$V_{M}_{4N_3\times 1} = A_{4}_{4N_3\times(24+3N_3)} \cdot \delta X_{(24+3N_3)\times 1} + L_{4}_{4N_3\times 1} \qquad P_{2}^{M}_{4N_3\times 4N_3}$$

The combined observation equation is

$$V_{(3N_1+3N_1+4N_2+4N_3)\times 1} = A_{(3N_1+3N_1+4N_2+4N_3)\times(24+3N_3)} \cdot \delta X_{(24+3N_3)\times 1} + L_{(3N_1+3N_1+4N_2+4N_3)\times 1} \tag{12}$$

where

$$V = \begin{pmatrix} V_{GPS}_{3N_1\times 1} \\ V_{\omega,\phi,\kappa}_{3N_1\times 1} \\ V_{GCP}_{4N_2\times 1} \\ V_{M}_{4N_3\times 1} \end{pmatrix}, \qquad \delta X = \begin{pmatrix} \delta X_1 \\ {}_{24\times 1} \\ \delta X_2 \\ {}_{3N_3\times 1} \end{pmatrix}, \qquad L = \begin{pmatrix} L_1 \\ {}_{3N_1\times 1} \\ L_2 \\ {}_{3N_1\times 1} \\ L_3 \\ {}_{4N_2\times 1} \\ L_4 \\ {}_{4N_3\times 1} \end{pmatrix}$$

The least squares solution is given by

$$\delta X_{(24+3N_3)\times 1} = -N^{-1}_{(24+3N_3)\times(24+3N_3)} \cdot C_{(24+3N_3)\times 1} \tag{13}$$

where

$$N_{(24+3N_3)\times(24+3N_3)} = A^{T}_{(24+3N_3)\times(3N_1+3N_1+4N_2+4N_3)} \cdot P_{(3N_1+3N_1+4N_2+4N_3)\times(3N_1+3N_1+4N_2+4N_3)} \cdot A_{(3N_1+3N_1+4N_2+4N_3)\times(24+3N_3)}$$

$$C_{(24+3N_3)\times 1} = A^{T}_{(24+3N_3)\times(3N_1+3N_1+4N_2+4N_3)} \cdot P_{(3N_1+3N_1+4N_2+4N_3)\times(3N_1+3N_1+4N_2+4N_3)} \cdot L_{(3N_1+3N_1+4N_2+4N_3)\times 1}$$

$$P_{(3N_1+3N_1+4N_2+4N_3)\times(3N_1+3N_1+4N_2+4N_3)} = \begin{pmatrix} P_1^{GPS}_{3N_1\times 3N_1} & & & \\ & P_2^{\omega,\phi,\kappa}_{3N_1\times 3N_1} & & \\ & & P_3^{GCP}_{4N_2\times 4N_2} & \\ & & & P_4^{M}_{4N_3\times 4N_3} \end{pmatrix}$$

The structures of the observation equations can be found in Appendix II.

The solutions are estimated through an iterative process. In each iteration increments for all unknowns are obtained and used to update the approximations for the next iteration.

2.2.8 Accuracy evaluation

The standard deviations of the unit weight and unknowns are typically used to evaluate quality of the adjustment and the accuracy of adjusted unknowns. The standard deviation of the unit weight σ_0 is computed by

$$\sigma_0 = \sqrt{\frac{V^T PV}{r}} \tag{14}$$

where V is residual vector and r is redundancy of the observation equation. The covariance matrix of the unknown/check points is computed by

$$\sigma_{X_i} = \sigma_0 N^{-1}{}_{X_{ii}} \tag{15}$$

where $N^{-1}{}_{X_{ii}}$ denotes the partial matrix of inverse of the normal matrix related to the unknown coordinates of checkpoints.

In addition, the root-mean square (RMS) error of checkpoints is usually computed independently as a measure of external accuracy. It is calculated by

$$RMS_{x,y,z} = \sqrt{\frac{\Delta^T \Delta}{3n}} \tag{16}$$

where Δ is the difference of known and estimated coordinates of checkpoints and n is number of checkpoints used.

2.2.9 Implementation

The first version of the bundle adjustment program has been implemented in C programming language on a Silicon Graphics O2/UNIX system. Figure 4 gives the configuration and modules of the system.

3. DGPS Survey of the Test Range

3.1 Control network design and landmark layout

The High Altitude Test Range is located in Madison County in Central Ohio. It consists of approximately 21 ground target points placed specifically for photogrammetric purposes. The network is situated in a flat area approximately 16x11 km, centered at latitude 39°56'24" North, and longitude 83° 24' 42" West (Li 1998). The target points are spaced at least 1km apart and distributed in a generally east-west direction. All target points are painted with concentric circles, a one-meter flat white circle and a three-meter flat black circle as background, centered on a monument. The network is illustrated in Figure 5 and a target is shown in the inset. The network has also three control points from higher-order NGS networks.

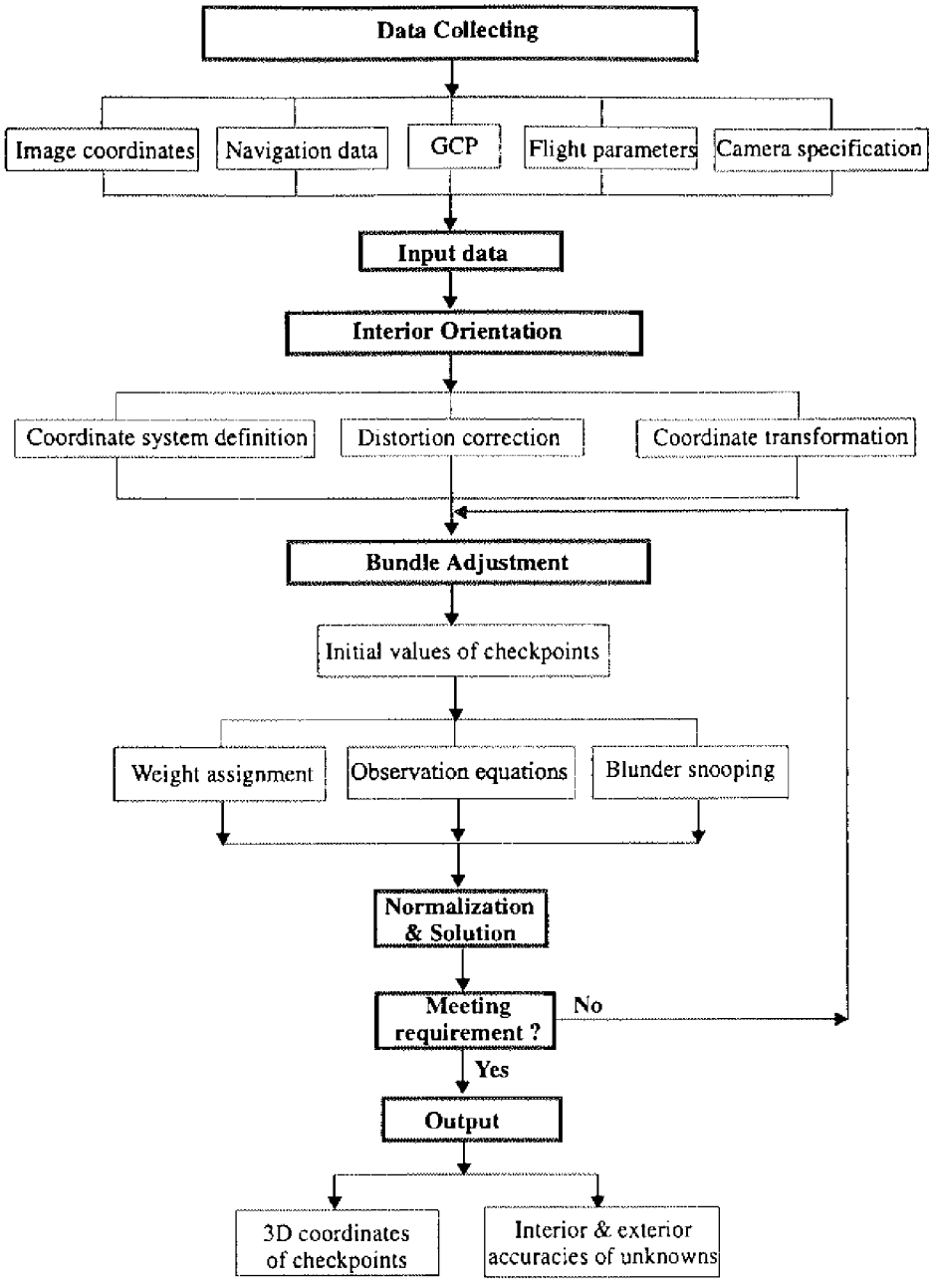

Figure 4. Implementation of the bundle adjustment program

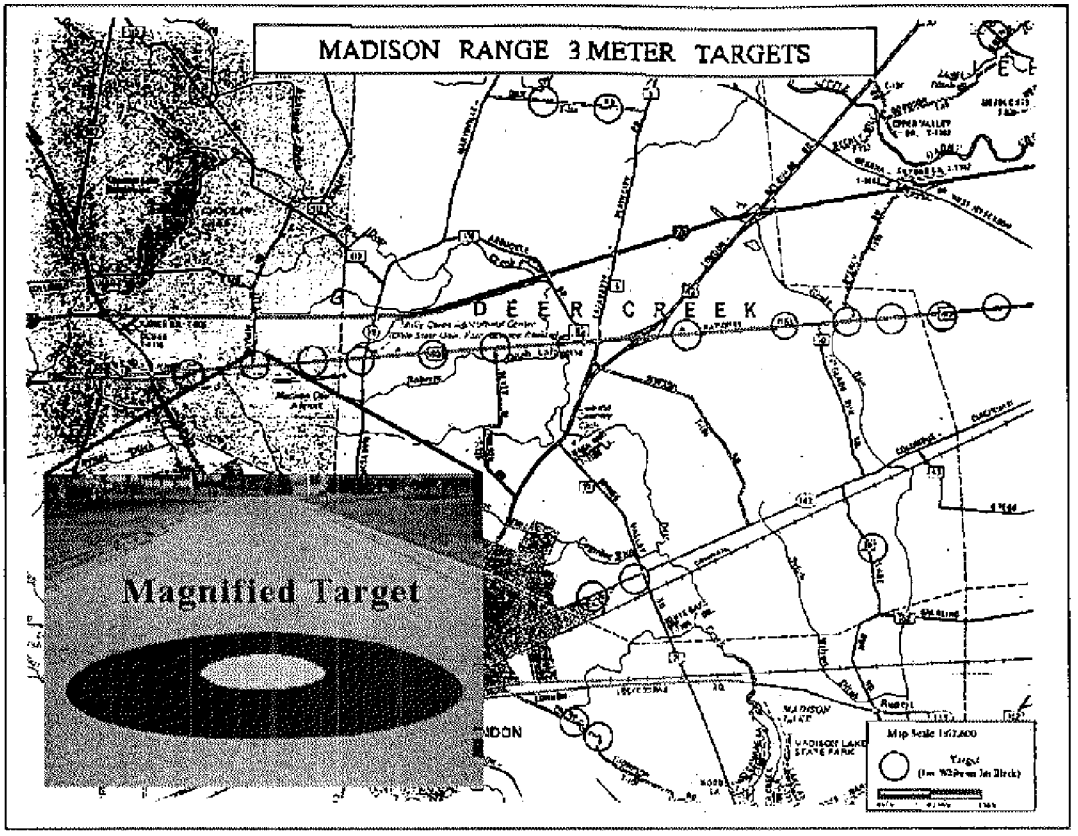

Figure 5. Control network and ground targets at Madison County

3.2 GPS field survey

We used three dual-frequency GPS receivers, one Trimble 4000SSE and two Trimble 4000SSI. The GPS survey consisted of 22 baselines spanning 21 control points and the 3 higher-order control points. 23 checkpoints and 5 feature points were also surveyed for the purpose of checking the attainable accuracy from the satellite imagery. The field survey work is divided into 3 steps:

- Tie all the unknown points to the higher-order NGS networks in the neighborhood with baselines, observed for a period no less than one-hour with at least four satellites visible and sampled at 1 second epochs. The precision dilution of position (PDOP) is equal to or less than 6. 22 baselines are completed in this step.

- Survey the known points using Fast Static mode with the second-order *B* station MAD-1 at Madison County Airport as a reference. All points were observed at least 8 minutes using a ground type antenna attached to a pole with the height fixed at 1.80 meters. During this stage we surveyed 14 points a day.
- Survey 23 checkpoints and five features on the ground in kinematic mode, again using MAD-1 as the reference station. Features like the Madison County airport, selected bridges and road intersections were observed with at least four satellites visible. These observations required points one half day.

We collected simultaneous observations at another reference station, located at the office of aerial engineering, Ohio Department of Transportation, in Columbus as a backup in the event of lost data at any of the other reference stations.

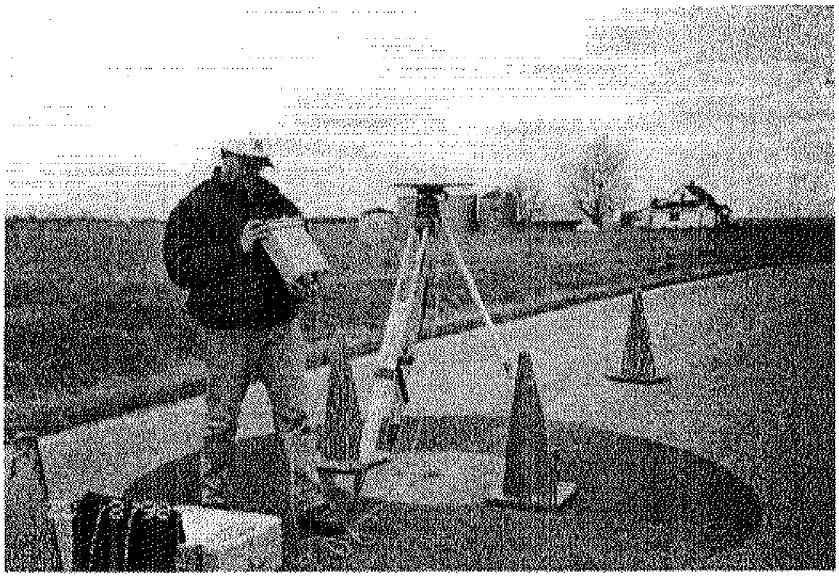

Figure 6. GPS field survey

At the end of each session, the data was downloaded from the receivers to the computer. In total, the survey was completed in 5 continuous days to determine coordinates of 21 high altitude target points, and 20 ground feature points (see figure 6).

3.3 GPS data processing

Once the survey was complete, on the same day we processed the baselines in order to obtain the vectors between the stations, using the GPS Survey software from *Trimble*. First the baselines forming the geodetic network were processed. Results from this part were the GPS solution, mostly the fixed solution "SSF", since none of the vectors was larger than 20 kilometer. Then the rest of the baselines, collected in Fast Static and Kinematic mode, were processed and saved in a separate project for other purposes. All baselines were successfully computed with satisfactory results (no baselines were computed with the data collected from ODOT reference station). Afterward, the solution files were exported into the least squares adjustment program "TRIMNET", also from *Trimble*, for further post-processing. This least squares adjustment provided estimates of the consistency of the GPS survey. All closures were less than 20 cm.

Next, a minimally constrained three-dimensional adjustment was applied, with the point *"Bolton-0"* as the reference station. This first adjustment was carried out to detect the internal precision and consistency of the field observations. All baselines were considered equally precise: 10 mm plus 1 ppm in horizontal and 10 mm plus 2ppm in vertical. All computations were carried out in the WGS-84 datum. The adjustment contained 22 baselines, with 70 observation equations, 31 unknowns, and 39 degrees of freedom. The standard deviation of unit weight was 0.736. Then we computed the coordinates for those points surveyed in Fast Static and Kinematic mode. Point S-20 was excluded because of one bad observations session. All other vectors were acceptable, based on the same criterion of RMS and percentage of rejection. With the geographic coordinates computed from the adjustment, geoid undulation (N) at each point was computed using the program "GEOID96" from NGS/NOAA. This value was algebraically added to the ellipsoidal height (h) in order to obtain the points orthometric elevation. The estimated standard deviation for the geoid undulation determination was around 0.08m.

Finally the geographic coordinates in the WGS-84 datum were obtained, and transformed into UTM, using programs from NOAA.

3.4 Accuracy Evaluation

The adjustment results indicate that point accuracy can attain standard deviations better than 0.02m, 0.02m, and 0.10m in X, Y and Z respectively. This level of accuracy is comparable with geodetic accuracy standard for Order C (1.0cm plus 10 ppm). Comparing the coordinates obtained in this survey against the coordinates reported by ODOT for points surveyed in Fast Static mode, we can see that they are similar, with the exception of point H-7. The differences are due to the fact that the previous coordinate values for points in the test range were determined in a local system. Tables 2 and 3 summarize the final coordinates for points in the geodetic network in geographic and UTM, zone 17 respectively. Table 4 presents the UTM coordinates for those feature points measured in kinematic mode.

For more detailed information about the GPS survey, refer Gonzalez (1998).

4. Simulation Study for Accuracy Estimation

To get an objective estimation of attainable geometric accuracy for coastline mapping, a simulation study has been conducted based on technical specifications of imaging sensors, orbit parameters, and varying numbers and distributions of GCPs. In addition, simulated satellite images are generated using the above mentioned specifications and a set of georeferenced aerial images of the Madison Test Range acquired by AIMS (Airborne Integrated Mapping System) developed by Center for Mapping of the Ohio State University.

4.1 Data used for the simulation study

Additional IKONOS-I specifications

Additional technical specifications listed in Table 5 are used in the simulation study.

Point ID	Latitude				Longitude				Ellip. H (m)
	dd	mm	ss.sssss		dd	mm	ss.sssss		
BLT- 0	39	53	29.61351	N	83	9	15.22023	W	239.280
MAD-1	39	56	0.26571	N	83	28	3.54038	W	294.120
H - 34	39	53	41.34586	N	83	36	17.08141	W	326.165
H – 5	39	56	4.30506	N	83	28	33.58297	W	297.329
H – 6	39	56	18.02108	N	83	23	31.79701	W	274.596
H – 7	39	56	23.02482	N	83	21	51.53036	W	268.347
H – 8	39	56	24.32378	N	83	21	24.87177	W	267.893
H – 9	39	56	25.30921	N	83	21	5.21788	W	266.929
H – 10	39	56	26.10118	N	83	20	49.11860	W	265.138
H – 11	39	56	27.41007	N	83	20	23.19705	W	263.863
H – 12	39	54	12.48774	N	83	21	13.06961	W	262.302
H – 13	39	54	1.53448	N	83	27	53.60308	W	289.445
H – 14	39	54	11.79728	N	83	30	29.33158	W	307.967
H – 102	39	53	47.34290	N	83	21	8.98974	W	261.117
H – 103	39	54	0.20682	N	83	24	28.20443	W	275.605
H – 104	39	54	3.57538	N	83	24	17.49158	W	273.794
H – 105	39	58	5.33472	N	83	28	28.72085	W	287.880
H – 106	39	58	18.35841	N	83	20	25.35505	W	263.509
M – 1	39	58	4.86102	N	83	27	15.44200	W	285.893
S – 20	39	56	2.55896	N	83	29	5.98618	W	299.321
S – 34	39	56	6.25170	N	83	27	51.16078	W	292.098
S – 41	39	56	7.84124	N	83	27	16.13181	W	286.509
S – 57	39	56	11.39818	N	83	26	0.54729	W	279.453
S – 63	39	56	12.67671	N	83	25	32.69480	W	277.794

Table 2. Geographic coordinates in WGS-84 for Points at Madison Co. high altitude test range from the GPS survey

Points	East UTM (X)	Std. Dev.	North UTM(y) m	Std. Dev	Ellip. h(m)	Std. Dev	Geoid N (m)	Orth. H (m)	Std. Dev	Remark
BLT-0	315817.420	---	4417942.666	...	239.280	...	-33.259	272.60	...	NGS Ord.A
Mad-1	289146.050	---	4423281.686	...	294.120	...	-32.922	327.00	...	NGS Ord.A
H-34	277305.242	--.	4419331.081	...	326.165	...	-32.914	359.08	...	NGS Ord.A
H-5	288436.36	0.013	4423426.00	0.014	297.33	0.020	-32.93	330.3	0.089	Fast Static
H-6	295611.33	0.006	4423653.47	0.007	274.60	0.017	-32.95	307.5	0.089	
H-7	297995.35	0.018	4423744.30	0.011	268.35	0.025	-32.96	301.3	0.090	Fast Static
H-8	298629.16	0.016	4423767.61	0.019	267.89	0.020	-32.96	300.8	0.089	Fast Static
H-9	299096.45	0.016	4423785.68	0.019	266.93	0.018	-32.96	299.9	0.089	Fast Static
H-10	299479.22	0.014	4423800.04	0.015	265.14	0.010	-32.96	298.1	0.089	Fast Static
H-11	300095.52	0.016	4423824.23	0.018	263.86	0.016	-32.97	296.8	0.089	Fast Static
H-12	298802.06	0.013	4419695.07	0.016	262.30	0.019	-32.86	295.2	0.089	
H-13	289280.81	0.004	4419614.06	0.005	289.45	0.019	-32.84	322.3	0.089	
H-14	285591.24	0.004	4420033.54	0.005	307.97	0.018	-32.85	340.8	0.089	
H-102	298878.52	0.007	4418917.18	0.009	261.12	0.022	-32.84	294.0	0.090	
H-103	294157.78	0.016	4419439.98	0.017	275.61	0.018	-32.84	308.4	0.089	Fast Static
H-104	294415.00	0.016	4419536.99	0.018	273.79	0.023	-33.00	306.6	0.089	Fast Static
H-105	288655.34	0.004	4427154.80	0.005	287.88	0.034	-33.04	320.9	0.090	
H-106	300134.10	0.007	4427246.66	0.009	263.51	0.022	-33.00	296.5	0.093	
M-1	290393.55	0.004	4427092.13	0.004	285.89	0.021	-32.92	318.9	0.090	
S-20	287665.68	0.017	4423393.55	0.018	299.32	0.021	-32.93	332.2	0.090	Fast Static
S-34	289445.02	0.015	4423458.14	0.019	292.10	0.025	-32.93	325.0	0.091	Fast Static
S-41	290277.86	0.014	4423484.23	0.017	286.51	0.022	-32.93	319.4	0.090	Fast Static
S-57	292075.01	0.016	4423544,75	0.019	279.45	0.028	-32.93	312.4	0.091	Fast Static
S-63	292737.21	0.015	4423566.17	0.017	277.79	0.024	-32.93	311.7	0.090	Fast Static

Table 3. UTM coordinates for points at Madison Co. high Altitude test Range from the GPS survey

Points	Description	X (East UTM)(m)	Y (North UTM) (m)	Elev.(m)
MAD-1	Base station	289146.1	4423281.7	327.0
S-34	Starting point at S-34	289445.0	4423458.1	325.0
S-34001	Madison Co. Airport runway (NE)	290236.4	4423221.5	320.2
S-34002	Madison Co. Airport runway (SE)	290236.7	4423201.3	320.4
S-34003	Madison Co. Airport runway (SW)	289018.2	4423160.9	329.4
S-34004	Madison Co. Airport runway (NW)	289017.7	4423183.4	329.4
S-34005	Ending Point at S-34	289445.0	4423458.1	325.0
Feat 002	S-13 - Inters. US-40 & Potee Rd.	285095.5	4423324.3	332.4
Feat 003	Bridge on Potee Rd. – SE Corner	284957.4	4423523.5	330.4
Feat 004	Bridge on Potee Rd. – SW Corner	284953.3	4423520.5	330.4
Feat 005	Bridge on Potee Rd. – NE Corner	284948.3	4423535.8	330.4
Feat 006	Bridge on Potee Rd. – NW Corner	284944.3	4423532.7	330.4
Feat 007	GCP on Bridge on Potee Rd.	284944.6	4423535.6	330.4
Feat 008	Bridge on Potee Rd. & I-70 – (SE)	284396.8	4424265.4	352.1
Feat 009	Bridge on Potee Rd. & I-70 – (SW)	284388.4	4424264.9	352.1
Feat 010	Bridge on Potee Rd. & I-70 – (NE)	284337.0	4424344.9	352.1
Feat 011	Bridge on Potee Rd. & I-70 – (NW)	284328.5	4424344.4	352.1
Feat 021	Starting point at S-41	290277.8	4423484.2	319.5
Feat 022	Bridge on Rt. 38 & I-70 (SE)	290775.7	4424125.0	323.0
Feat 023	Bridge on Rt. 38 & I-70 (NE)	290801.6	4424209.2	323.0
Feat 024	Bridge on Rt. 38 & I-70 (NW)	290791.9	4424209.5	323.0
Feat 025	Bridge on Rt. 38 & I-70 (SW)	290766.2	4424125.3	323.0
Feat 031	Inters. Glade Run Rd. & Railroad (NW)	298405.5	4420837.8	299.4
Feat 032	Inters. Glade Run Rd. & Railroad (SW)	298406.6	4420835.4	299.4
Feat 033	Inters. Glade Run Rd. & Railroad (SE)	298413.4	4420838.2	299.4
Feat 034	Inters. Glade Run Rd. & Railroad (NE)	298412.4	4420840.6	299.4

Table 4. UTM coordinates for features measured in kinematic mode

Parameter	Values
Altitude (km)	680
Inclination (deg)	98.1
Ground resolution (m)	0.82
Convergence angle (deg)	26
Pixel size (μm)	12
Swath width (km)	11

Table 5. Additional technical specifications of IKONOS-I

DEM data

A DEM of the test range in Madison County was computed from hypsographic features (contour lines) in DLG files from 7.5' USGS quad sheets, downloaded from the USGS website. ARC/INFO provided the functions to compute a DEM with 1m by 1m spacing (Figure 7).

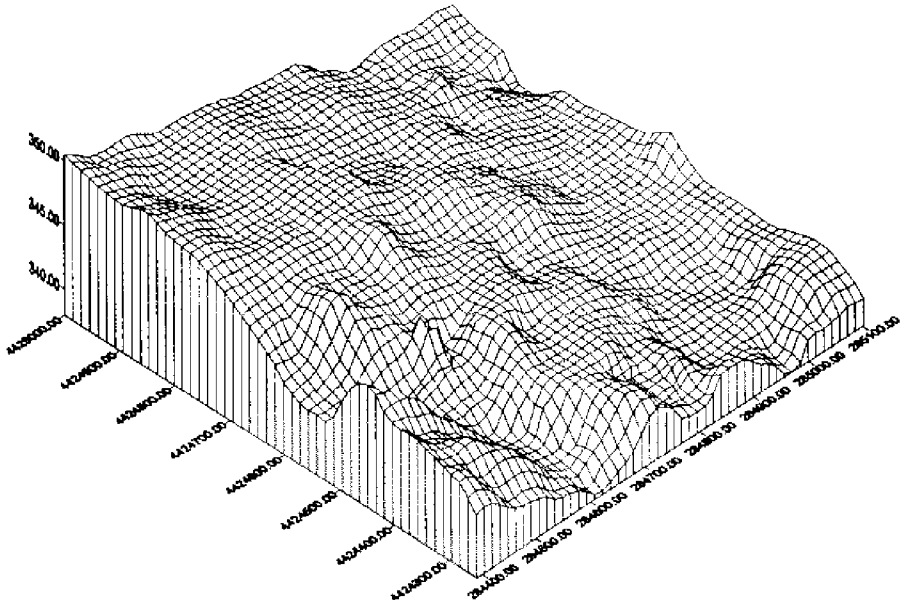

Figure 7. DEM of the test range

AIMS images

In 1997 and early 1998, the Center for Mapping of the Ohio State University carried out a test flight for direct georeferencing of aerial imagery by GPS/INS integration. The AIMS positioning component consists of two dual-frequency Trimble 4000SSI GPS receivers, and a medium-accuracy, high reliability strapdown Litton LN-100 inertial navigation system. The imaging component consists of a digital camera with a 4,096 by 4,096 pixel CCD array (60 by 60 mm imaging area resulting in a 15 micron pixel size), manufactured by Lockheed Martin Fairchild Semiconductors. The imaging sensor is integrated into a camera-back (BigShot-TM) of a regular Hasselbald 553 ELX camera body together with a supporting data acquisition interface. The camera is installed on a rigid mount together with the INS. The principal point coordinates, focal length, and lens distortion characteristics are provided by a camera calibration procedure. Figure 9 shows a frame image from AIMS.

4.2 Generation of simulated satellite images

The synthetic satellite images are generated based on the principle of "projection" and "back-projection". *Projection* is from aerial images to DEM. *Back-projection* here indicates projection from DEM onto satellite images at fore-, nadir- and back-looking angles. Therefore brightness values in the simulated satellite images are a "map" of the aerial images. Both of them share the identical DEM (Figure 8). The key steps are

- Select the field within the established geodetic network in which the aerial photography and corresponding DEM are available. Note that the exterior and interior orientation parameters of the aerial photography are known.
- Specify the number of orientation lines (OLs), exterior orientation parameters of OLs, interpolation parameters, and pointing angles at fore- nadir- and back-looking angles. Table 6 shows the simulated exterior parameters at an initial time and after 5 seconds at fore-, nadir- and back-looking.

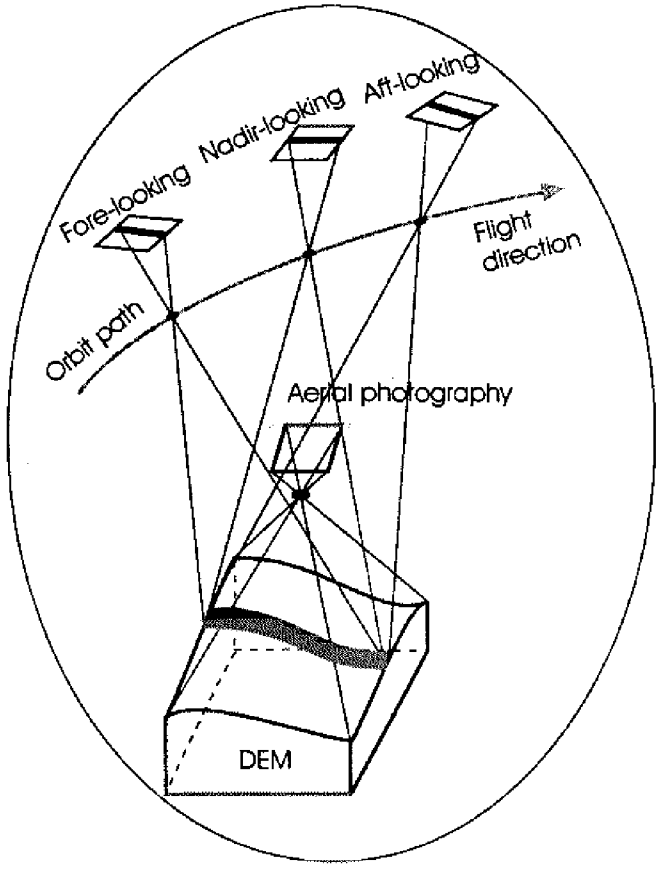

Figure 8. Simulation of satellite images from aerial images

- Calculate the brightness values of the first line of the forward-look strip. This is done at each pixel of the line, say (x_1, y_1) in the satellite image. Its corresponding ground coordinates (X_1, Y_1, Z_1) is determined by projection from the satellite image to the DEM. Furthermore, the corresponding coordinates (x'_1, y'_1) in the aerial image are determined by a projection from (X_1, Y_1, Z_1) to the aerial image. Finally, the brightness value at (x'_1, y'_1) of the aerial image is assigned to that at (x_1, y_1) of satellite image. This process is repeated for all pixels of the satellite image, so that a simulated satellite image can be produced.

Parameter	Sigma	Fore-look		Nadir-look		Aft-look	
		Initial	In 5"	Initial	In 5"	Initial	In 5"
Xs (m)	3.0	330459.91	365125.34	284315.71	318981.13	238171.49	272830.637
Ys (m)	3.0	4096476.85	4091613.07	4424815.01	4419951.12	4753153.21	4748289.39
Zs (m)	3.0	679996.87	679996.63	679996.87	679999.67	679996.87	679998.90
Omega (arc sec)	2.0	0.000020	-0.000157	0.000020	-0.006215	0.000010	-0.000633
Phi (arc sec)	2.0	0.000020	0.000022	0.000020	-0.000931	0.000010	0.00001
Kappa (arc sec)	2.0	0.139636	0.139560	0.139647	0.139749	0.139647	0.144059

Table 6. Exterior orientation parameters of a segment of a simplified orbit

In this way, we produced simulated nadir-, fore-, and aft-looking satellite images (Figures 10, 11 and 12).

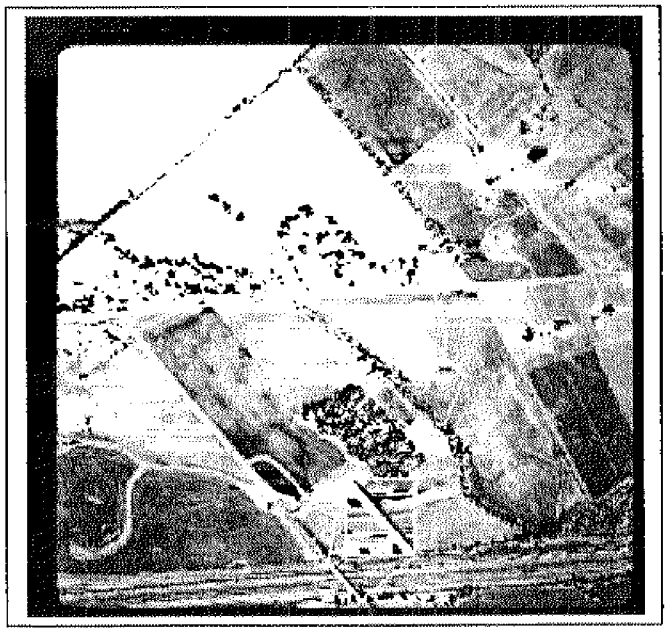

Figure 9. AIMS image (0.4m)

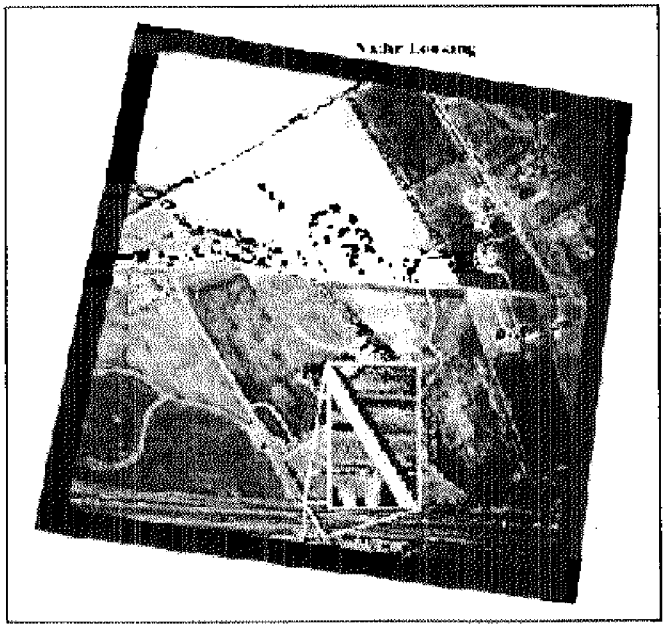

Figure 10. Simulated nadir-looking image (0.82m)

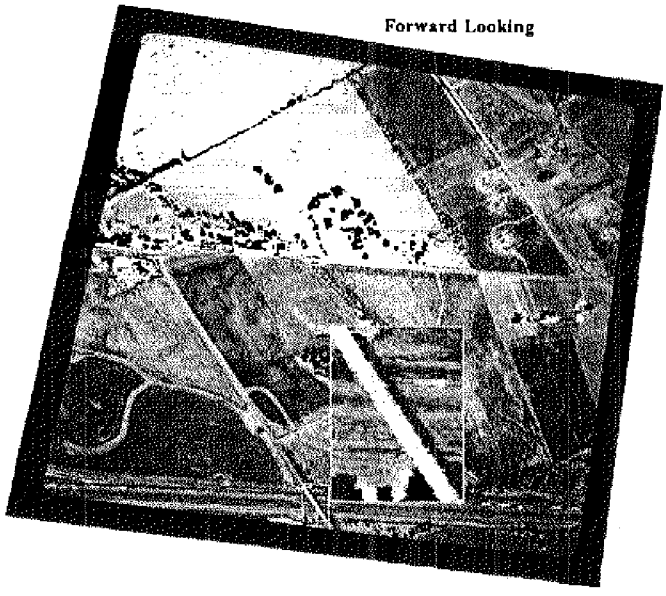

Figure 11. Simulated fore-looking image (0.82m)

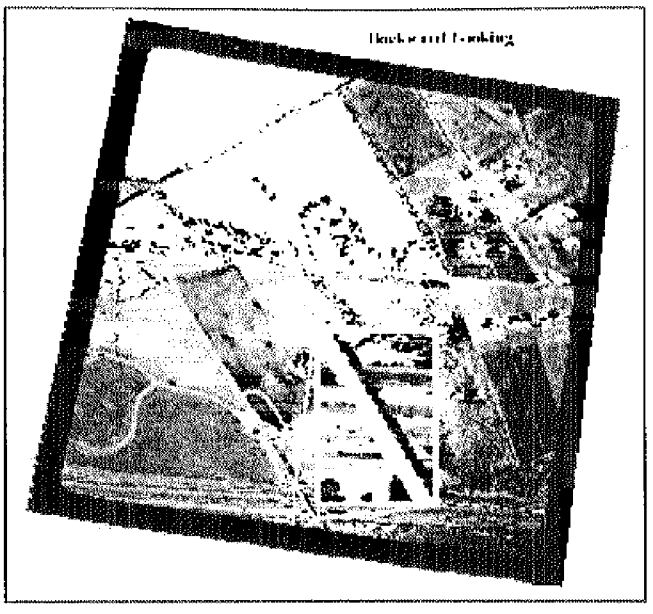

Figure 12. Simulated aft-looking image (0.82m)

4.3 Accuracy estimation

4.3.1 Accuracy versus various number of GCPs

Affects of number and distribution of GCPs on geometric triangulation accuracy using MOMS-02 have been previously studied (Ebner et al. 1992, Fraser and Shao 1996). We used technical specifications of IKONOS-I for a simulation and accuracy estimation. Again, we used 24 GCPs (21 *high altitude* ground target points plus three control points from higher-order NGS networks) and 14 checkpoints at established geodetic control network at Madison County High Attitude Range.

The simulation was conducted under the following conditions:

1) Image coordinates of the GCPs and checkpoints are computed by the collinearity equations (Equations 4).
2) We add random errors (1 sigma) to the following simulated parameters
   - Position of OLs: 3m
   - Attitude of OLs: 2 arc second
   - Measured image coordinates of GCPs and checkpoints: 0.5 pixel

The ground coordinates of 14 checkpoints are computed by a simulation program. Differences between the computed and known ground coordinates of the checkpoints are depicted in Figure 13 with a variation of numbers of GCPs used. The average planimetric and vertical error may reach 11 to 12m without GCPs, and around 2.8m with 24 GCPs. When 4 GCPs are used, the accuracy is largely improved. However, more than 4 GCP's do not contribute significantly. Thus it is not encouraged to improve the geometric accuracy by increasing the number of GCP's. This result also matches the similar study for MOMS-02 (Fraser and Shao1996, Ebner et al. 1991).

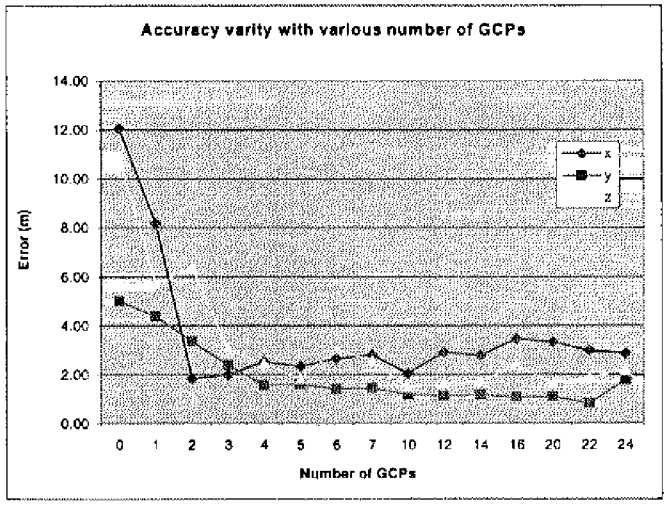

Figure 13. Accuracy of ground coordinates vs. number of GCPs

4.3.2 Accuracy versus distributions of GCPs

Figure 14 shows the GPS network. We chose 6 groups of GCPs to form 6 distributions in order to examine the impact of GCP distribution on accuracy. The 6 distributions are:

Distribution 1: a triangle consisting of points MAD-1, BLTZ-0 and H-34;
Distribution 2: a trapezoid formed by point H-34, BLTZ-0, H-105 and H-106;
Distribution 3: approximately a straight line (cross track) formed by points H-105, M-1 and H-106;
Distribution 4: Points S-20, H-5, S-34, MAD-1, S-41, S-57, S-63, H-6, H-7 and H-11 spreading in the area;
Distribution 5: Points H-34, H-14, H-13, H-12 and BLT-0 approximately on a straight line (cross
Distribution 6: Points S-20, S-34, S41 and S-57 approximately on a straight line (cross track).

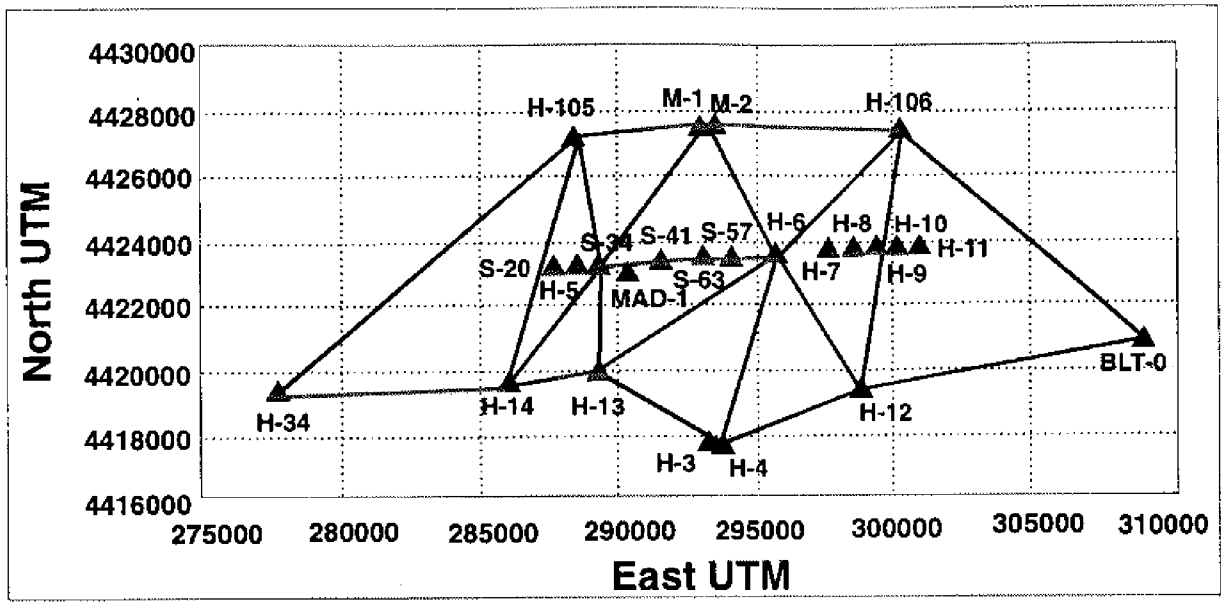

Figure 14. GCP selection in GPS geodetic network at Madison County

The GCPs of the 6 distributions are used in bundle adjustment to calculate the ground coordinates of 14 checkpoints. The accuracy versus various distributions of GCPs is depicted in Figure 15. We find that the strength of GCP distributions affects the planimetric and vertical accuracy significantly. For example, Distribution 1 and 3 have the same number of GCPs, but not distributions. The geometric accuracy for Distribution 1 achieves 1.84m and 3.43m in X and Y, 3.21 in Z, while Distribution 3 has 53.4m and 8.11m in X and Y, and 5.88m in Z. Distribution 2 and 6 present a similar situation. It is to note that GCPs distributed on a straight line across the track constitutes a weak geometric configuration (Distributions 3, 5 and 6). Thus GCP distribution is a critical key to achieve high accuracy.

4.3.3 Accuracy versus image measuring errors of checkpoints

When measuring image coordinates in a stereo pair, errors are unavoidable. The impact of these errors on ground coordinates should be assessed. Suppose that image coordinate measurement errors range from 6μm (0.5pixel) to 24μm (3pixel), and all other parameters are noise-free. The ground coordinates of 14 checkpoints are calculated. The accuracy of ground points versus errors in image coordinates of checkpoints is depicted in Figure 16. The result demonstrates that large measurement errors in image

coordinates affect geometric accuracy of ground coordinates. Indeed, the planimetric coordinate errors increase 0.5m for each error of 0.5 pixels in image coordinates.

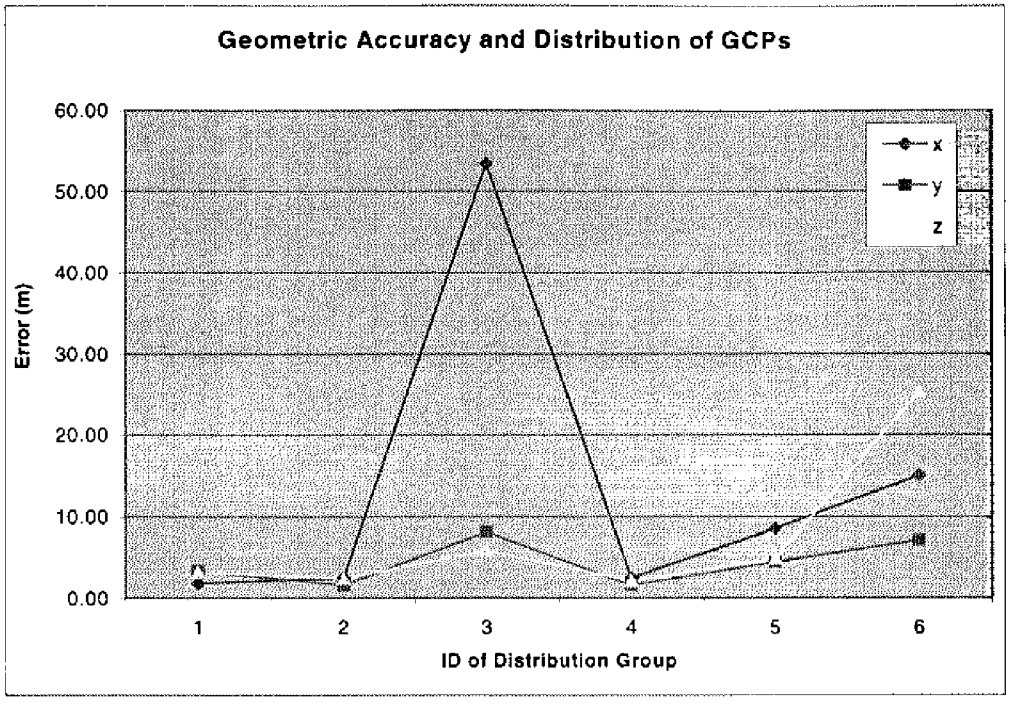

Figure 15. Accuracy vs. GCP distribution

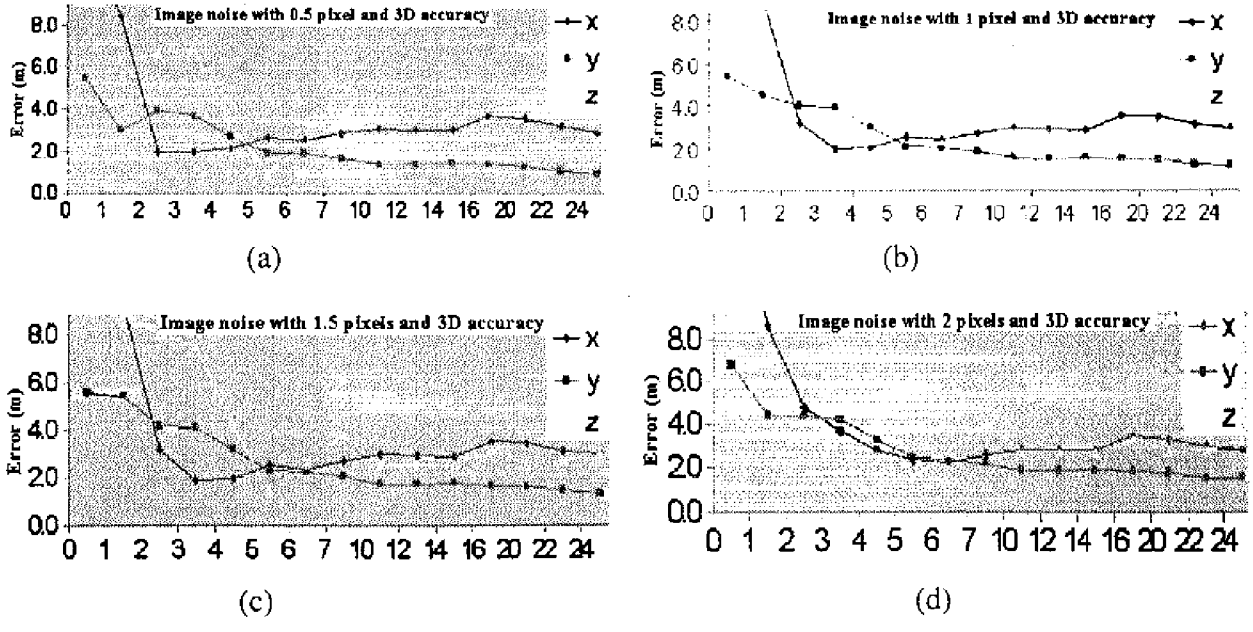

Figure 16. Accuracy versus errors in image coordinates

4.3.4 Accuracy versus errors of image coordinates of GCPs

Under the same condition as above, we examine the impact of image coordinate errors of GCPs on ground coordinate accuracy. The errors of ground coordinates for 14 checkpoints are shown in Figure 17. When image measuring errors are 5pixels, Z coordinate error reaches 7.7m and X and Y errors are around 4m even though all of 24 GCPs are taken as control information. Obviously accurately locating and measuring GCPs is helpful in improving the geometric accuracy.

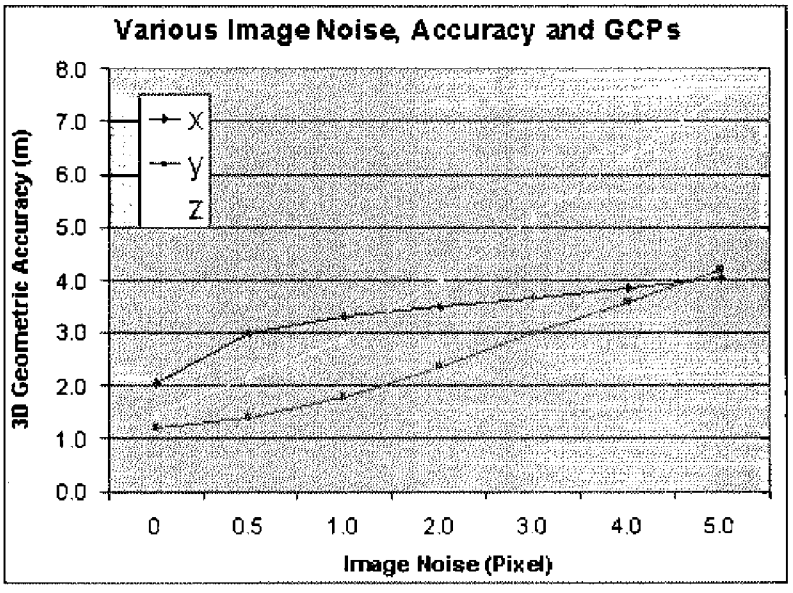

Figure 17. Accuracy versus errors of image coordinates

5. Processing of Airborne and Space Shuttle Three-line Sensor Data

5.1 Processing of Airborne HRSC data

5.1.1 High resolution stereo camera-HRSC

High Resolution Stereo Camera (HRSC) system has nine CCD lines providing multiple along-track stereo images as well as high-resolution hyperspectral information. It was designed by Institute for Planetary Exploration of DLR (Germany Aerospace Agency) in Berlin-Adlershof. The primary contractor for its production is Dornier Company in Friedrichshafen, Germany. HRSC is designed as a compact single-optic pushbroom instrument with multiple (nine) CCD sensors mounted in parallel.

Compared to previous imaging systems, a miniaturization by a factor of 5 to 10 has been achieved. The instrument consists of the camera system and the mass memory system. Depending on the actual ground track velocity the integration time of the CCD lines is adjusted in such a way that the center pixels are kept square. The ground pixel size varies depending on the current flying height. Nine superimposed image strips are acquired almost simultaneously by the forward motion of the aircraft over the terrain. More information about the system can be found in Wewel (1996).

Five of the nine CCD lines are arranged at specific viewing angles for providing stereo imaging and photometric viewing capability (Figure 18). Four of the nine CCD lines are covered with different filters for the acquisition of hyperspectral images. Table 7 lists some parameters related to stereo metric characteristics of the system.

Focal length	175 (mm)	Radiometric resolution	10 bit reduced to 8 bit
Total field of view	36° X 11.8°	Read-out frequency	450 lines/s
Number of CCD lines	9	Mass	32 kg
Stereo angles	18.9° and 12.8°	Stabilization	Zeiss T-AS stabilized platform, gyros fixed to the camera, DGPS
Pixels per CCD line	5272	Data recording	SONY high-speed tape recorder
Pixel size	7μm	Flight navigation	PC and GPS

Table 7. HRSC camera specification [http://www.ba.dlr.de/pe/HRSC/]

A raw HRSC image consists of 9 image strips (1 strip per sensor). Different image strips may have different pixel resolution depending on the commanded pixel binning which is constant during one imaging sequence.

5.1.2 The HRSC data set

DLR provided us a data set including five strips (nadir channel, stereo aft-panchromatic, stereo fore-panchromatic, photometry aft- panchromatic, and photometry fore-panchromatic), 109 GCPs in WGS-84, exterior orientation parameters for each CCD line. In this mission, the aircraft flew from southeast

to northwest with a flying height of 2,500m. The images are recorded in the VICAR format developed by JPL/NASA. Figure 19 shows the stereo aft-panchromatic strip with an area at its original scale.

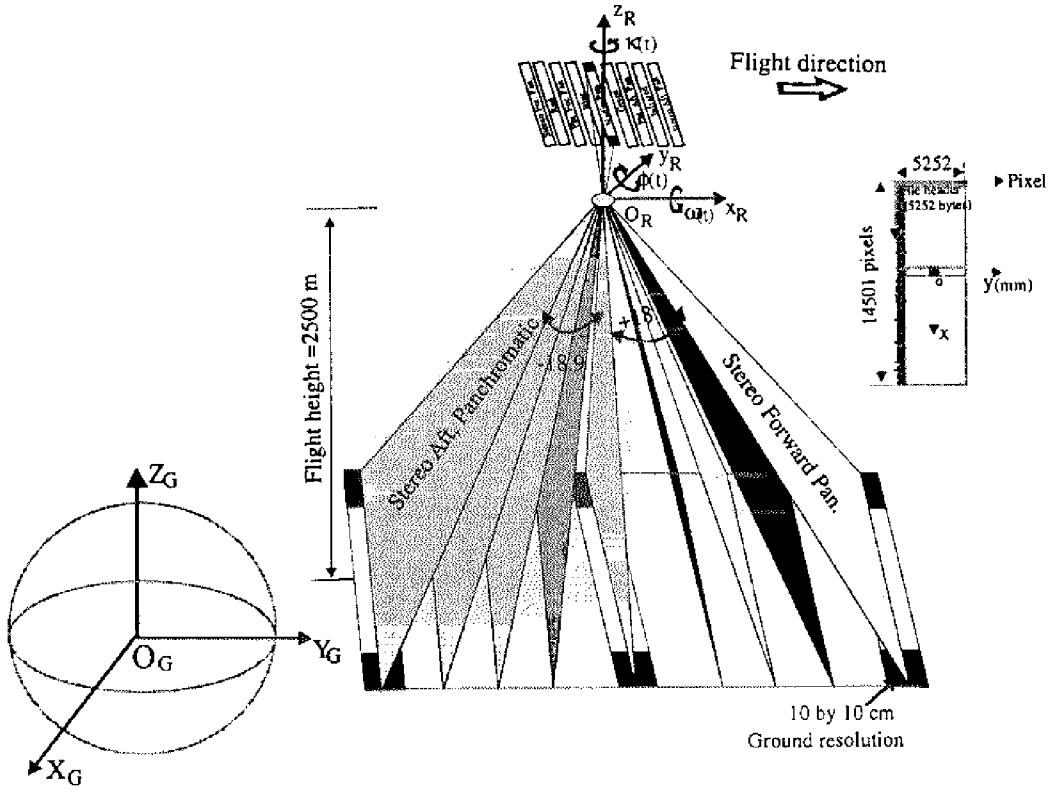

Figure 18. The principle of along-track stereo imaging system of HRSC

In this test field, 69 GCPs are covered even though 109 GCPs were laid. Unfortunately, only 49 GCPs are available since the image coordinates of other GCPs can not be identical in image. Figure 20 depicts the distribution of 49 GCPs. The image coordinates of 49 GCPs in five strips are provided.

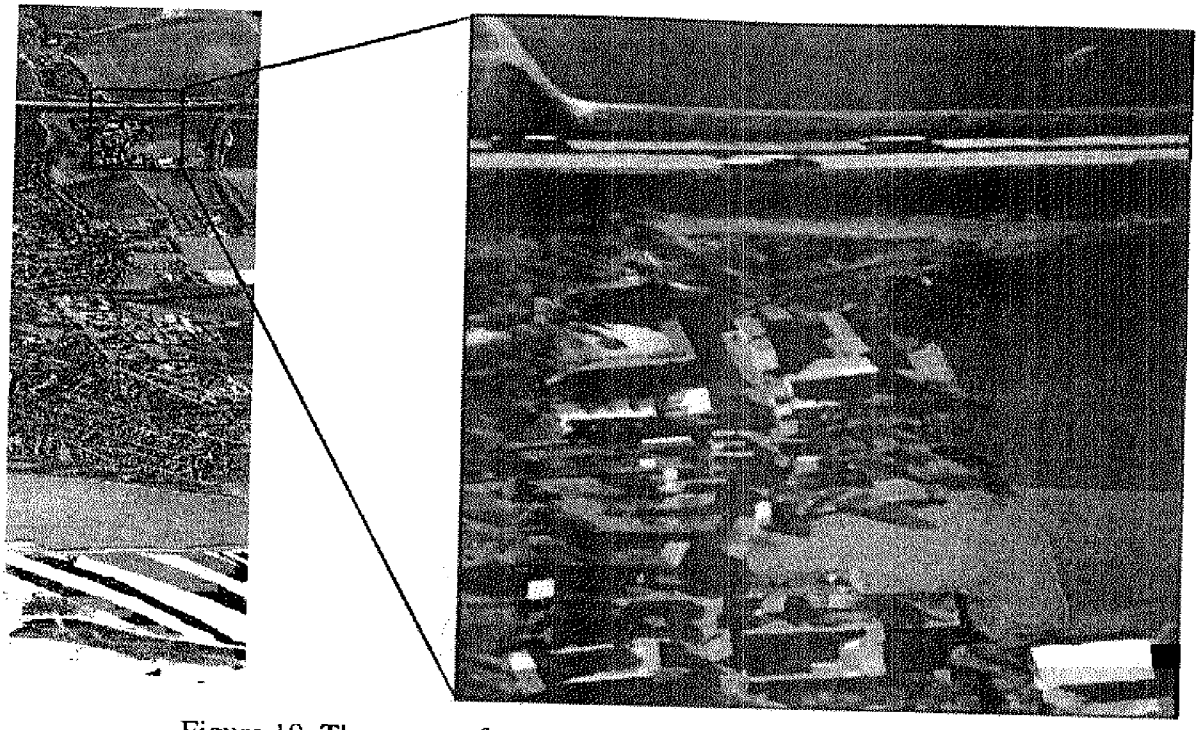

Figure 19. The stereo aft-panchromatic strip acquired by HRSC

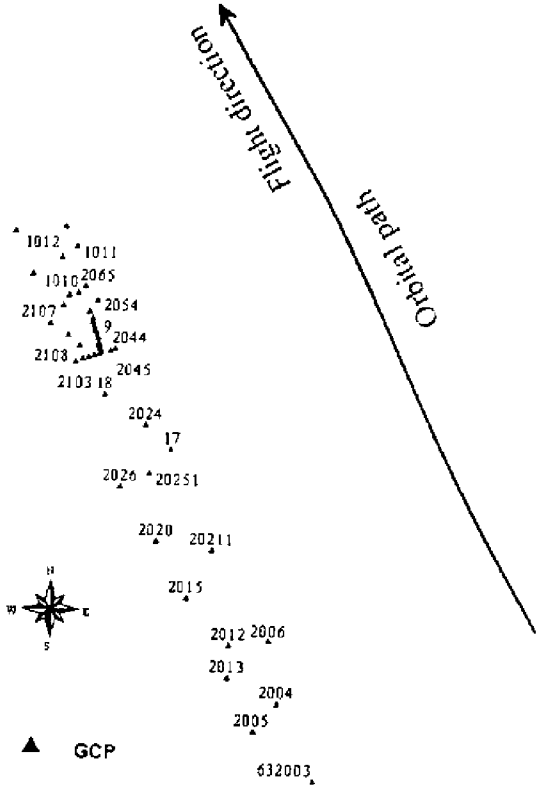

Figure 20. Distribution of GCPs

5.1.3 Data Processing and Accuracy Evaluation

5.1.3.1 Image coordinates

Three identical focal planes define the HRSC camera, each one consisting of three sensor arrays with 5184 active pixels. Together the three focal planes form one high-resolution panchromatic (clear) nadir channel, two panchromatic (clear) stereo channels with convergence angles of ±19°, four color channels at ± 3° and ± 6° and two additional channels at ± 13° for photometric purposes. Note that for HRSC only the two scan lines with convergence angles of ±19° and the nadir line will be considered for stereo aspects. Six color, or photometric, scan lines are available for interpretation purposes, multispectral applications, and for improving the photogrammetric capabilities (e.g. in steep terrain). Thus, we choose stereo fore- panchromatic (S1) and stereo aft- panchromatic (S2) to construct a stereo image pair. The geometric relationship between image coordinate and reference coordinate system is drawn in Figure 21.

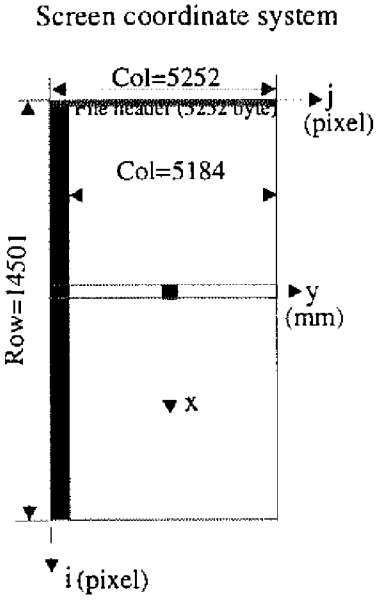

Figure 21. HRSC image strip file

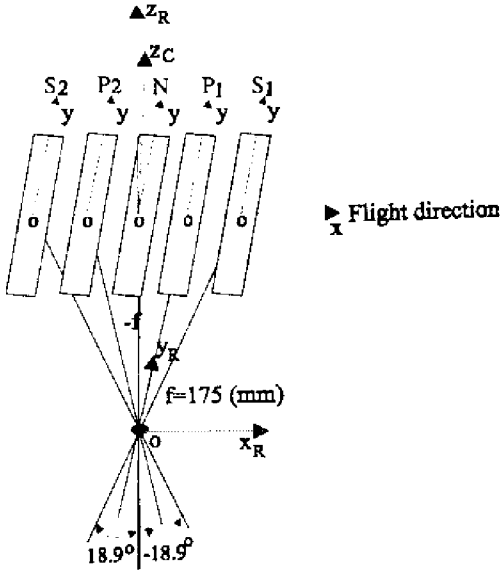

Figure 22. HRSC stereo formation

DLR performed the following tasks and provided us the results:

- Transformation from screen coordinate system to image coordinate system,
- Principal point offsets for S1 and S2, and

- Distortion rectification, including CCD curvature and lens distortion corrections.

Image coordinates of GCPs and checkpoints are provided in ASCII files.

5.1.3.2 Bundle adjustment and accuracy assessment

The geometric conditions of HRSC are quite similar to those of other pushbroom scanners such as IKONOS-I and MOMS-02. The perspective geometry is also only valid on the sensor line, whereas it is close to a parallel projection in the orbit direction. Therefore, the bundle adjustment model described in this report is appropriate. The purpose to use this data set is to test our program. We defined the camera coordinate, reference coordinate, and ground coordinate system. Various experimental strategies on checking our program and the attainable accuracy in planimetry and height are implemented. Table 8 indicates attainable geometric accuracy of 49 checkpoints versus the number of GCPs ranging from 0 to 49.

GCP	Check Points	σ_0 [μm]	σ_x [cm]	σ_y [cm]	σ_z [cm]	RMS_x [cm]	RMS_x [cm]	RMS_x [cm]
0	49	6.990	15.140	7.324	18.010	15.144	8.276	18.758
1	49	6.952	16.025	8.230	18.654	15.140	7.324	18.010
2	49	6.914	15.939	8.186	18.553	15.140	7.324	18.010
3	49	6.877	15.853	8.142	18.454	15.140	7.324	18.010
4	49	6.840	15.769	8.099	18.355	15.140	7.324	18.010
5	49	6.805	15.686	8.059	18.259	15.140	7.324	18.010
49	49	5.628	12.973	6.663	15.101	15.140	7.324	18.009

Table 8. Accuracy of ground points versus number of GCPs

The experimental results demonstrate that increasing the number of GCPs does not improve the geometric accuracy even slightly. The interior accuracy and exterior RMS appear to be same. This is because that the exterior orientation parameters of each CCD line and the image coordinates of GCPs and checkpoints are provided by DLR, and they are bundle adjustment results already. A further bundle adjustment does not improve the result. However, the result verifies the model and bundle adjustment system we have developed.

Another experiment concerns the accuracy improvement versus order of polynomial and number of orientation images. Various combinations were tried and the results are shown in Table 9. The results show that more than 10 and less than 10 orientation lines (OLs) will not be helpful to interior accuracy of ground points and will have little affect on the exterior accuracy of ground points. The order of polynomial depends on the real flight path. Our experiment shows that various orders of polynomial will have little affect on the accuracy. This may be because the flight path of this mission is an approximate straight line (Figure 20).

5.2 Processing of MOMS-2P

5.2.1 Imaging principle of MOMS-2P

The MOMS (Modular Opto-electronic Multispectral Stereo-Scanner) project started in the early 70's and was specifically designed to generate digital topographic mapping data, primarily through automated DTM extraction. The accuracy of the system, around 5m, was sufficient to generate digital orthoimages with sufficient information content and geometric accuracy to meet map specifications at 1:50,000 scale and larger (Fraser and Shao 1996). The current camera system (2nd generation) has proven that MOMS can simultaneously collect high resolution panchromatic (PAN) and multispectral (MS) images. This was demonstrated during the 2nd German Spacelab experiment (Fritsch et al. 1998). After this flight, it was slightly redesigned to operate on-board the Russian Space Station MIR for a two-year term. In May 1996 MOMS-2P was attached to the remote sensing module PRIRODA on MIR. After testing and calibration the first data collection phase started in October, 96 and lasted until April, 97. Due to several problems, mainly technical failures of the MIR space station (and also of the MOMS02 power supply), the data stream stopped for about 1 year, and only a few MOMS-2P/PRIRODA data collections were acquired between September, 96 and April, 97. Fortunately, collection of phase 2 data began in January, 98, will last until the total download of MIR, around the end of 1999 (Kornus and Lehner 1998).

Order of Polyn.	# of OLs	σ_0 [μm]	σ_x [cm]	σ_y [cm]	σ_z [cm]	RMS_x [cm]	RMS_x [cm]	RMS_x [cm]
1	5	11.756	27.109	13.924	31.561	15.143	7.3253	18.0122
	9	8.817	20.326	10.439	23.661	15.140	7.3243	18.0093
	10	**8.632**	**19.899**	**10.220**	**23.165**	**15.140**	**7.3241**	**18.0089**
	13	9.768	22.517	11.564	26.211	15.140	7.3242	18.0091
	21	10.794	24.880	12.778	28.961	15.140	7.3242	18.0091
	29	11.481	26.463	13.590	30.802	15.140	7.3242	18.0091
	73	13.384	30.846	15.841	35.904	15.142	7.3242	18.0095
2	5	17.037	39.440	20.316	137.653	15.021	7.481	32.714
	9	9.322	21.535	11.076	25.338	15.026	7.542	18.054
	10	**8.671**	**20.031**	**10.303**	**23.569**	**15.026**	**7.542**	**18.054**
	13	9.407	21.726	11.175	25.565	15.026	7.542	18.054
	21	9.845	22.735	11.694	26.754	15.026	7.542	18.054
	29	10.497	24.240	12.468	28.526	15.026	7.542	18.054
	73	11.565	26.704	13.734	31.424	15.026	7.542	18.054
3	5	5.118	11.811	6.069	13.756	15.141	7.324	18.00
	9	4.660	10.748	5.521	12.513	15.143	7.324	18.00
	10	**4.491**	**10.357**	**5.320**	**12.058**	**15.141**	**7.324**	**18.00**
	13	5.011	11.555	5.945	13.451	15.141	7.324	18.00
	21	5.397	12.441	6.389	14.482	15.141	7.324	18.00
	29	5.623	12.973	6.663	15.101	15.141	7.324	18.00
	73	6.400	14.751	7.576	17.170	15.141	7.324	18.00

Table 9. Accuracy of ground points versus the number of OLs and order of polynomial

The imaging principle of MOMS is that a three line optical-electronic scanner is placed in the focal planes of one or more objective lens. The three linear CCD arrays are designated a, b and c. The sensors are oriented perpendicular to the direction of flight. During flight the sensors continuously scan the terrain with a constant frequency, recording three images. As a consequence, three push-broom image strips cover the terrain surface. By modifying the CCD integration frequency relative to the

velocity of the camera platform, the image scale, and the size of the sensor elements, nearly square ground pixels are generated (Figure 23). In general, each object point is projected into three images. If blocks with 20% or 60% sideward overlap are used, object points are projected into as many as six to nine images. In contrast to conventional aerial photogrammetry with frame cameras, the image recording is performed in dynamic mode. A large number of successive images, which consist only of three lines form three image strips. In general, each three-line has its own set of exterior orientation parameters.

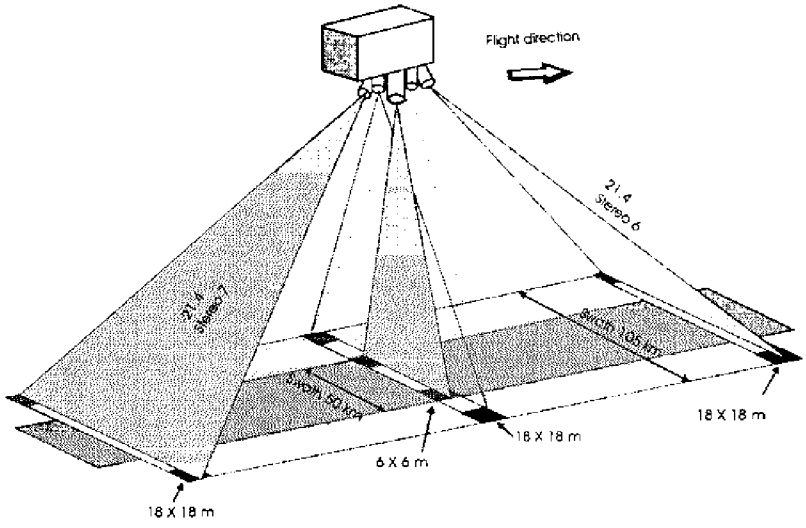

Figure 23. Imaging gerometry of MOMS-2P (Seige et al. 1998)

The optical camera system of MOMS02-P provides 4 data collection modes. Mode A uses the PAN channels 5,6,7 only, which provide 3-fold along track stereo scanning with different ground resolutions. The nadir looking HR channel (6m ground pixel size) comprises 2 arrays with 6000 sensor elements each, which are optically combined into 1 array with 9000 sensor elements. The other CCD arrays consist of 6000 sensor elements (18m ground pixel size). Mode B delivers all 4 MS data channels simultaneously (1,2,3,4). Mode C offers high resolution MS imaging (5A PAN, 2,3,4). Mode D provides simultaneous stereo and multispectral capability. From a photogrammetric point of view, automatic DTM reconstruction requires mode A using the forward and backward looking channels 6 and 7. Unfortunately, an operation error blurred the data collection of the high-resolution channels 5A and 5B making this data useless (Fritsch et al. 1998).

The main parameters of the MOMS-2P mission are listed in Table 7. In contrast to the D2 mission, the MIR orbital inclination of 51.6° also allows for imaging of industrial countries in Europe and North America. A typical scene collected from a flying height of 380 to 400 km represents an area of about 50km in width. A base-to-height-ratio of 0.8 is expected. MIR moves along a very smooth and stable orbit what causes less distortion in the imagery. Its revisit time varies between 3 and 18 days. The GSD for the stereo lenses 6, 7 is about 15-18 m, and the image strip has an extent of 2976 pixels.

Parameters	**MOMS-02/D2**	**MOMS-2P**
Camera carrier:	Space shuttle	MIR space station
Mission duration:	10 days	at least 18 months
Data storage	HDT recorder	On-board mass memory et al.
Orbital height	296 km	400 km
Orbital inclination	28.5°	51.6°
Ground pixel nadir/stereo	4.5 (HR) / 13.5 (m)	6.0 (HR) / 18.0 (m)
Swath width nadir/stereo (mode A)	37 km	50 km
Geometric camera calibration	laboratory	Laboratory, in-flight
Orbit information	TDRSS	tracking GPS
Attitude information	Shuttle-IMU	MOMS-IMU, star sensor

Table 10. Parameters of MOMS-02/D2 and MOMS-2P (Ebner et al. 1996)

5.2.2 Test field in Germany for MOMS-2P

The test site investigated in this report covers an area 178 km long and 50 km wide, comprised of scenes 27 to 30 in Figure 24, from southeast Germany to about 160 km beyond the Austrian border. The ground pixel size of the imagery is 5.9m and 17.7m at 390 km orbit height. More information is available in (Kornus and Lehner 1998).

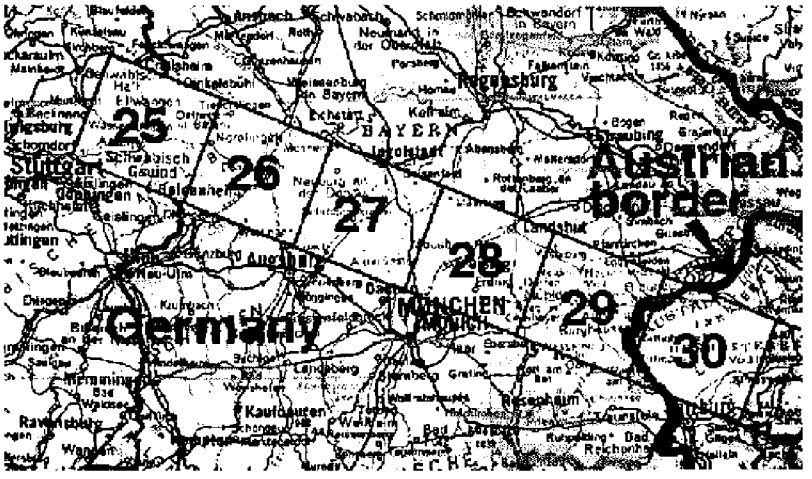

Figure 24. Geographic location of the test area (Kornus and Lehner 1998)

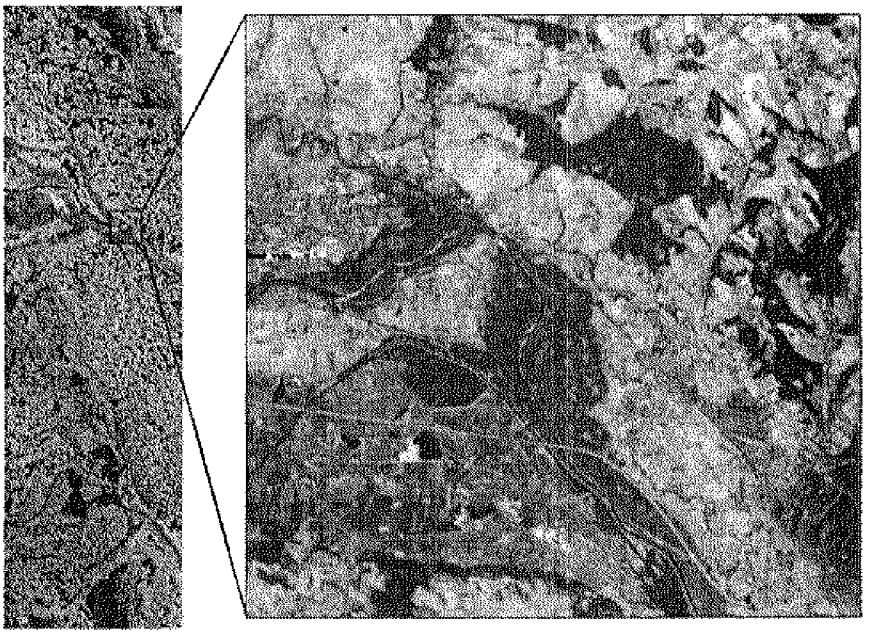

Figure 25. The fore-looking strip and an area in the original scale (GSD 17m)

5.2.3 Experimental data for MOMS-2P

5.2.3.1 Calibration data

The geometric calibration of the MOMS imaging system was performed at the laboratories of the German aerospace company DASA, where MOMS was developed and is manufactured. A rigorous model of the geometry of each CCD-array is composed of 5 parameters (Table 11):

- Principal point coordinates of each sensor (x_0, y_0),
- Rotation parameter κ of the CCD-array in the image plane,
- Deviation of the focal length df , and
- Distortion parameter K of the sensor curvature. The sensor curvature is modeled by a second order polynomial. The parameter K here indicates the along track deviation at the edges of the CCD-array at 3000 pixel distance from the array center, caused by the sensor curvature.

	Lab-calibrated Parameters				**In-flight-Parameters by photogrammetry**			
	HR5A	HR5B	ST6	ST7	HR5A	HR5B	ST6	ST7
f [mm]	660.256	660.224	237.241	237.246	-	-	237.1936	237.2509
x_0 [pixel]	0.1	0.2	-7.2	-0.5	-	-	46.7152	-10.5293
y_0 [pixel]	-0.4	0.1	8.0	19.2	-	-	-110.4370	-166.339
K_c [pixel]	-0.3	-0.4	-1.1	1.7	-	-	0.01111	-0.01153
k [mdeg]	-2.9	5.4	-1.5	-1.4	-	-	-	-

Table 11. Lab-calibrated camera parameters for MOMS-2P (Kornus 1996, 1997)

The model and the derivation of the model parameters from the calibration measurements are comprehensively described in (Kornus 1996, 1997).

5.2.3.2 Navigation data

MOMS-2P has its own navigation system, MOMS-NAV, consisting of a Motorola Viceroy GPS receiver with dual antennas and a LITEF gyro system. Table 12 lists exterior orientation parameters of OLs of the strips.

5.2.3.3 Ground control points and checkpoints

We chose 10 ground control points within the test field and along the strip. To check our results of the bundle adjustment we also selected 24 checkpoints (Figure 26). The ground coordinates of GCPs and checkpoints were obtained by topographic maps of scale 1:50,000 with an accuracy of 1.5 m in X, Y

and Z (provided by University of Stuttgart). They are in the 4th zone of Gauss-Krueger coordinate system.

ID	Xs	σ_{X_S}	Ys	σ_{Y_S}	Zs	σ_{Z_S}	φ	σ_{φ}	ω	σ_{ω}	κ	σ_{κ}
1	4387760.572	6.156	762221.663	6.176	5078269.988	6.142	40.889	0.118e-2	-6.594	0.115e-2	77.896	0.817e-2
3331	4393602.852	6.123	820523.632	6.167	5064058.878	6.093	41.005	0.102e-2	-7.087	0.103e-2	77.853	0.734e-2
6661	4399140.765	6.661	878747.392	6.167	5049413.921	6.068	41.122	0.101e-2	-7.587	0.108e-2	77.815	0.683e-2
9991	4404369.520	6.078	936890.099	6.150	5034328.615	6.045	41.237	0.991e-2	-8.083	0.994e-2	77.777	0.671e-2
13321	4409288.079	6.073	994947.086	6.142	5018807.697	6.050	41.365	0.102e-2	-8.576	0.102e-2	77.731	0.698e-2
16651	4413895.784	6.105	1052910.503	6.151	5002854.357	6.100	41.487	0.128e-2	-9.078	0.123e-2	77.697	0.759e-2
19981	4418198.597	6.124	1110782.710	6.158	4986471.512	6.121	41.598	0.185e-2	-9.570	0.125e-2	77.657	0.844e-2
23311	4422189.390	6.155	1168551.892	6.170	4969656.175	6.154	41.718	0.275e-2	-10.069	0.145e-2	77.604	0.940e-2

Table 12. Orientation parameters of OLs derived from navigation data
(Unit: meter for position parameters, degree for attitude parameters)

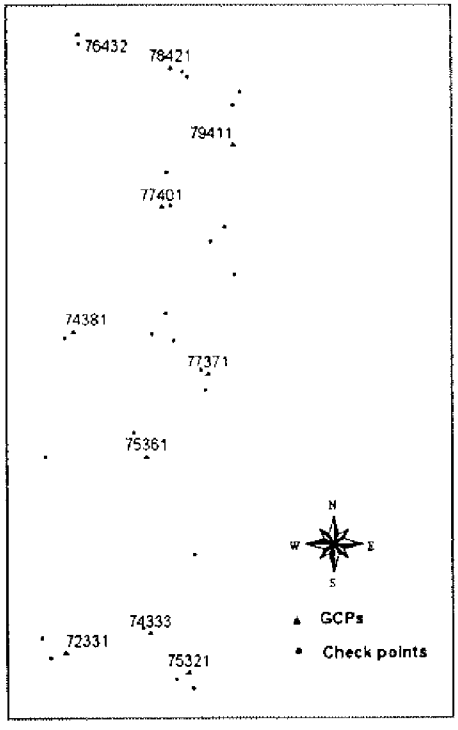

Figure 26. Distribuation of GCPs and checkpoints in the MOMS-02P test field

The above image data, navigation data of OLs, ground and image coordinates of GCPs and checkpoints are all provided to us through Institute of Photogrammetry at University of Stuttgart.

5.2.4 Bundle adjustment

5.2.4.1 Coordinate systems

Coordinate systems for bundle adjustment of MOMS-2P data are illustrated in Figure 26. The ground coordinates system $O_G - X_G Y_G Z_G$ is WGS-84. The image coordinate system $O_R - X_R Y_R Z_R$ is an image reference coordinate system, in which the x axis is defined to be parallel to the flight direction, and the y axis is orthognal to it. The image coordinate systems of fore- and aft-looking images are $O_6 - X_6, Y_6, Z_6$ and $O_7 - X_7, Y_7, Z_7$ respectively.

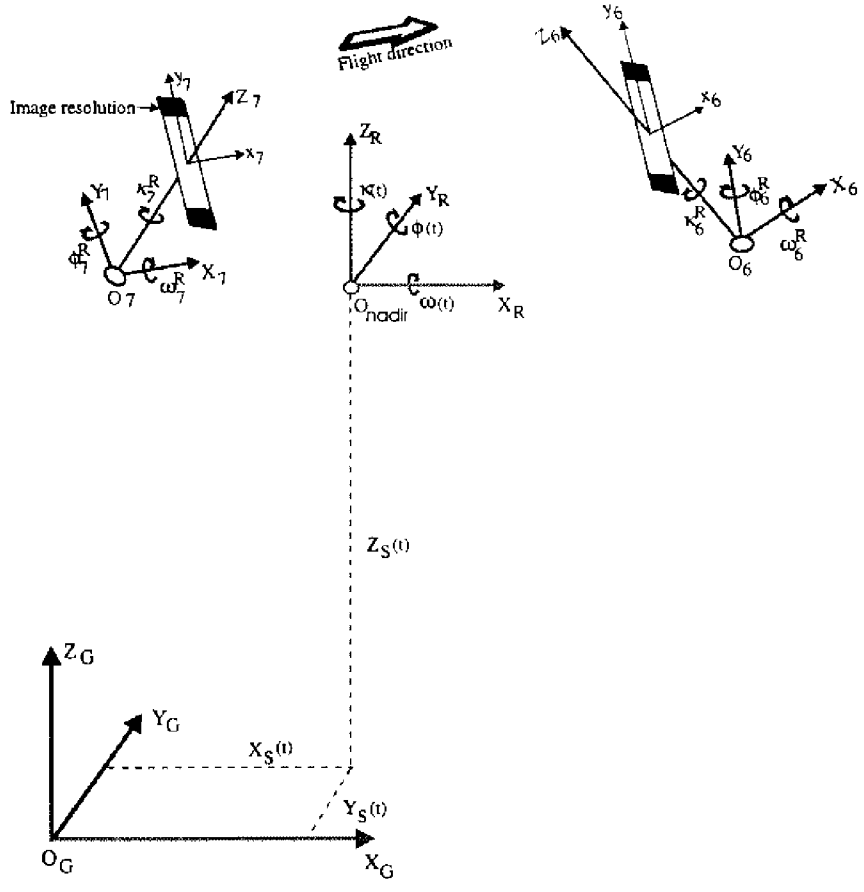

Figure 27. Coordinate systems used in bundle adjustment of MOMS-02P data

5.2.4.2 Transformation to image coordinate system

A separate image coordinate system is defined for each CCD array, which is then related to an image reference coordinate system by a 3-D transformation. For each CCD array there are a focal length f, principal point offset (x_o, y_o), and a curvature parameter K_c. In this experiment, the parameters are treated as constants and no self-calibration is performed in the bundle adjustment. The screen coordinates (i, j) are transformed to image coordinates in following steps:

- Transformation from screen coordinates to image coordinates

  $x' = 0$

  $y' = (j - column/2) * pixel\_size$

  Here $pixel\_size = 10e-3\,(mm)$

- CCD curvature correction

  $cx = k_c * y' * y'$

- Lens distortion correction: unavailable
- Final image coordinates

  $x = cx - x_0$

  $y = y' - y_0$

5.2.4.3 Access of orientation parameters at OLs from fore- and aft-looking strips

The navigation data are available at OLs and for nadir-looking strip. The fore- and aft-looking strips access the navigation data through the imaging geometry. In this data set, the first line belongs to the first line of scene 25 of the nadir-looking strip (5A and 5B). To get the correct orientation of the aft- and fore-looking strip, it is necessary to add/subtract 8600 lines respectively. Figure 28 illustrates the relationships.

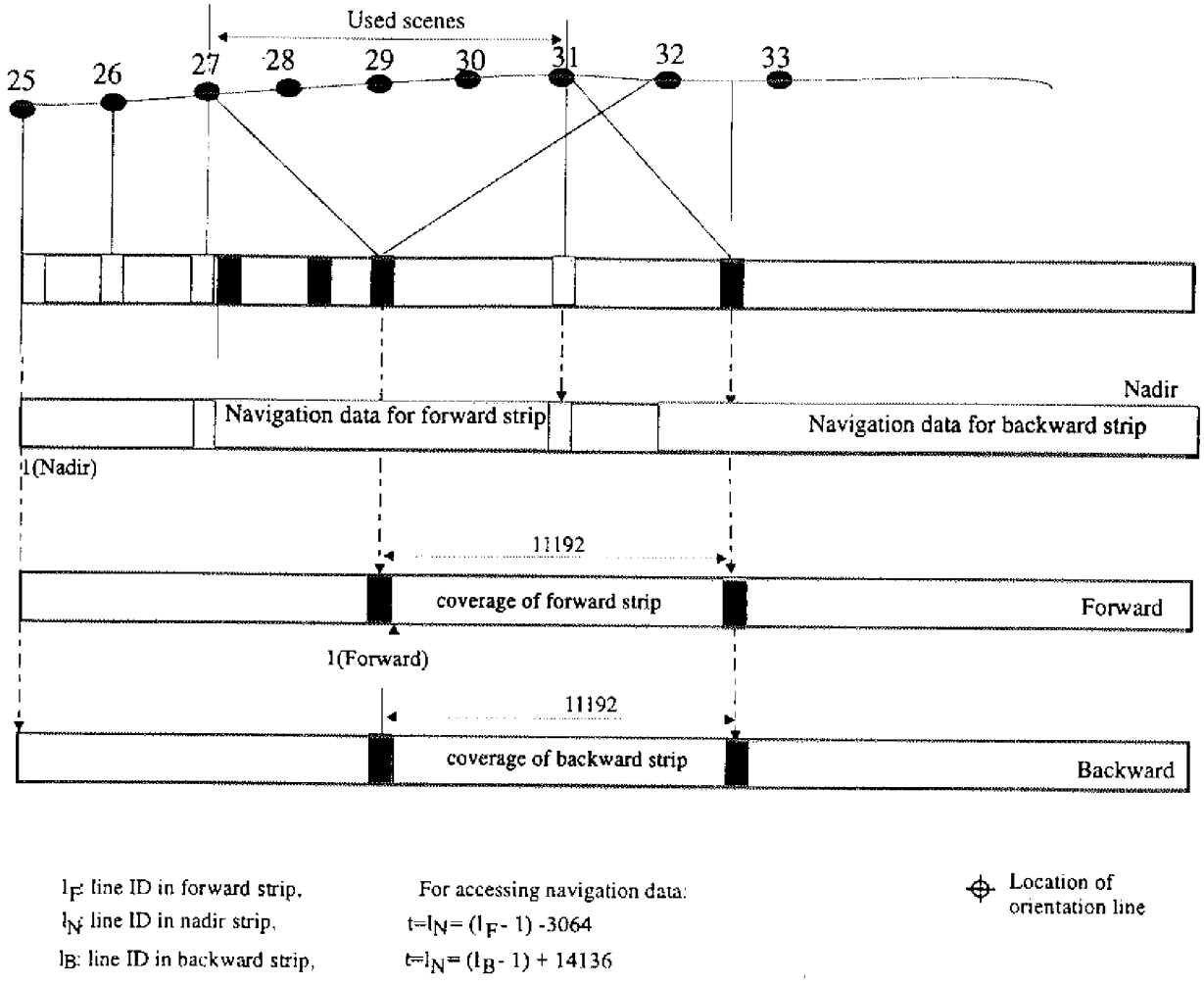

Figure 28. Access of navigation data from fore- and aft-looking strips

5.2.4.4 Transformation from Gauss-Krueger to WGS-84

The provided navigation data of OLs are in the geocentric WGS-84 coordinate system. However, the coordinates of GCPs and checkpoints are in Gauss-Krueger coordinate system with (X, Y, h). We performed a coordinate transformation from Gauss-Krueger coordinate system to WGS-84. The transformation of the (X, Y, h) coordinates to (X, Y, Z) coordinates needs the following steps:

- Transform (X, Y) coordinates in Gauss-Krueger zone 4 to geographic coordinates latitude φ and longitude λ with Bessel ellipsoid parameters,
- Calculate the geoid undulations, N, with latitude φ and longitude λ.

- Transform the height h above the geoid to ellipsoidal heights H with respect to WGS-84 using given geoid undulations, N, by H = h +N.
- Transform geographic coordinates latitude φ and longitude λ and H into geocentric WGS-84 coordinates with WGS-84 ellipsoid parameters,

5.2.4.5 Input data information

Table 13 gives an overview of all observations and their a priori standard deviations and weight assignment. These were fed into the bundle adjustment. For the entire segment of the orbit 8 OLs were employed. The distance between the OIs was 3330 image lines, corresponding to 8.2 seconds flight time. This proved to be sufficient to model the temporal course of the exterior orientation parameters. The accuracy of the coordinates of GCPs and checkpoints was assumed to be 6m in X, Y and Z, corresponding to 1 ground pixel of the HR channel. Accuracy of 6m in position and 0.11e-2°in attitude are used for orientation parameters at OLs.

Observations	Type	Prior σ	Weight assigned
24 checkpoints	Image coord.	0.5 pixel	1.0
10 GCPs	Image coord.	0.5 pixel	1.0
3 x 8 position	Ext. orient.	6.0 m	2.6e-6 (mm^2/m^2)
3 x 8 attitude	Ext. orient.	0.11e-2°	100.0 $(mm^2/\deg^2)$

Table 13. Observations and weights introduced into the bundle adjustment

5.2.4.6 Adjustment computation and accuracy

In the bundle adjustment the exterior orientation parameters are estimated only at OLs, while these between OLs are modeled by third order polynomials. The parameters and navigation data are treated as uncorrelated.

GCP	Checkpoints	RMS_X [m]	RMS_Y [m]	RMS_Z [m]
10	24	10.805	8.435	18.164

Table 14. Accuracy of ground coordinates calculated by bundle adjustment from checkpoints

Table 14 shows that accuracy of 11m for X, 8m for Y and 18m in Z was achieved as verified by 24 independent checkpoints when using 10 GCPs measured with 0.5 pixel precision (equal to 8.5m in object space). This result is close to the result reported by University of Stuttgart (11m in X and Y, and 14m in Z, Fritsch et al. 1998). It is to note that our above result was achieved by adding a 3-D offset to fore- and aft-looking exposure center respectively. They were evaluated as (–26.9μm, 1598.4μm, -80.1μm,) for fore-looking and (–80.1μm, -1805.3μm, -81.4μm) for aft-looking strip. Previous investigations indicated deviations of the camera geometry from the laboratory calibration measurements (Kornus and Lehner 1998). However, the deviation is not significant. Since this is our first computational result of the data set, more efforts will be made to clear this point.

PART II. GIS AND SPATIAL ANALYSIS

6. Coastline Erosion and Change Detection

6.1 Erosion in Lake Erie area

6.1.1 Background

Coastal erosion is a problem throughout the U.S., occurring both on the east and west coasts, the Gulf shore, and the Great Lakes. Many factors act together to influence coastal erosion (Platt 1998). These include the depth of water bodies, their alignment with prevailing winds, change of water levels, coastline geology, and the effects of human activities. Coastline erosion may cause problems when its development approaches (Li 1998), for example, a residential area. The shape of the coastline may be changed as a result of coastline erosion. Moreover, the environment of the coastal zone can be influenced by the coastline change.

The coastal zone supports a wide range of unique habitats and species (Maslen et al. 1996). The coastline status is crucial to human beings, wildlife, and property in these areas. Coastal zone managers, emergency management officials, and coastal property owners need to be aware of the potential risks to coastal property before, during, and after severe storms and hurricanes. As new sensors become available and new technologies are focused on the problems of hazard mitigation in the coastal zone, a wealth of data are being generated which will permit volumetric analyses of recent landform morphology along the coast. These data can provide high spatial and temporal resolution forms for modeling the most recent changes (Dusen 1997). GIS techniques are widely used to analyze different characteristics of the landscape. Applications can be categorized as planning or management, process modeling, inventory, and assessment. In addition, they offer basic supporting functions for a modern GIS package. Within these categories, a spatial analysis through the use of GIS enables end-users to have information for decision-making. The modernized coastal erosion management is one of these applications.

Data involved in coastline change are diverse, including spatial data, time series data, social and economic data, and multimedia information (Li 1998). The spatial data are coastline positions, topographic data, bathymetric data, parcel data, etc. The social economic data are integrated with spatial data to support decision-making from census data or city planning maps. The time series data, for instance, wind and wave observations, can be integrated with spatial data through the locations of

sensors. GIS can make it possible for the integration of spatial data, time series data, and social economic data to develop a coast-based GIS database.

6.1.2 Land-eating Lake Erie

Erosion is defined as the gradual wearing away of the earth's surface by the natural forces of wind and water. For billions of years, oceans have been altering the earth's coastlines through erosion. The constant action of winds, waves and ice flows has also affected the coastline of Lake Erie and the other Great Lakes up to the present day (Ohio Coastal Management Program 1997).

Lake Erie, the great body of fresh water forming Ohio's north coast, is the fourth largest of the five Great Lakes. Lake Erie provides an unlimited water supply to communities along its shore, is an unmatched recreational and sport-fishing area, and provides significant quantities of sand and gravel for construction. On the other hand, Lake Erie is also a dynamic body of water noted for the ferocity of its storm waves and the havoc they wreak along the lakeshore. Waves, currents, shore erosion, and flooding are all problems that must be dealt with in coastal areas (Hansen 1997). About 95% of Ohio's Lake Erie shore (Figure 29) is eroding and nearly 2,500 structures are within 50 feet of destruction. The Ohio Geological Survey estimates that more than 3,200 acres of Ohio's Lake Erie shore have been lost to erosion since the 1870s. Due to these severe erosion problems, economic losses exceed tens of millions of dollars per year (Ohio Geology Survey 1993).

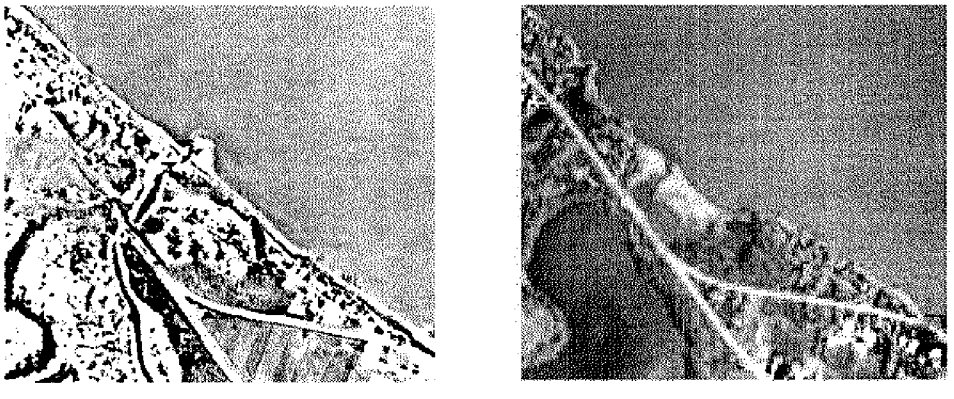

(a) Old Woman Creek - 1962 (b) Old Woman Creek – 1997

Figure 29. An example of erosion in Lake Erie Area

6.1.3 Influencing Factors of erosion

Primarily, it is the force of waves and gravity that cause erosion. On the coast, the forces of erosion are embodied in waves, currents, and wind. Surface water flow and freeze-thaw cycles may also play a role. Not all of these forces may be present at any particular location. Erosion is a natural process. However, it can be influenced both adversely and beneficially by human activity. Some of the factors that may influence the forces of coastal erosion are discussed below (US Army Corps of Engineers 1993).

6.1.3.1 Coastal geomorphology

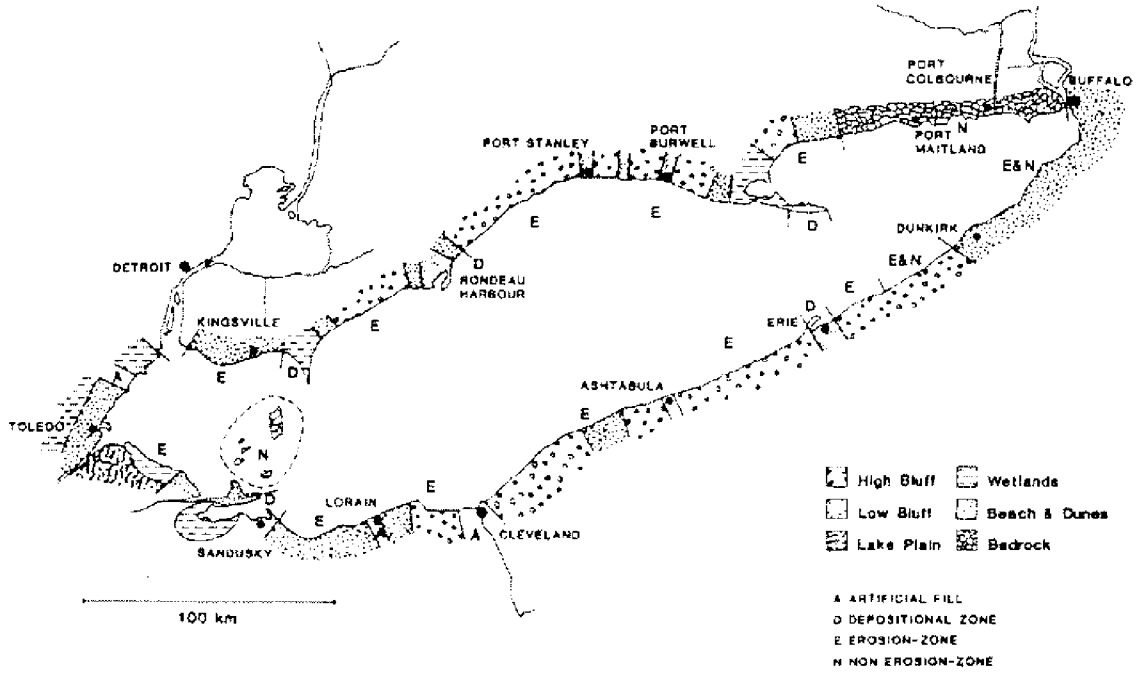

Figure 30. Erodibility of Lake Erie coastline (Herdendorf and Bolsenga 1993)

Geomorphology is the general form of the earth's surface and the changes that occur to it. The coastal geomorphology of Lake Erie region is of glacial origin. Figure 30 shows that there are a variety of general shore types in Lake Erie region: high and low rocky bluffs, low flood plains and coastal marshes, high and low sand/till bluffs, sand dunes, and artificial coastlines. Among the eroded shore types, the two most common ones are sand/till bluffs and sand dunes (Herdendorf Bolsenga 1993). Unfortunately, easily eroded banks of glacial till and lacustrine sediments characterize most of Lake

Erie's shores, while fewer reaches are composed of resistant bedrock bluffs (northeastern Lake Erie coast). Figure 31 presents a cross section view of a typical beach profile showing significant features and related terms. The erosion process occurs within an area roughly from the bluff crest out into the near shore to a water depth of about 30 feet.

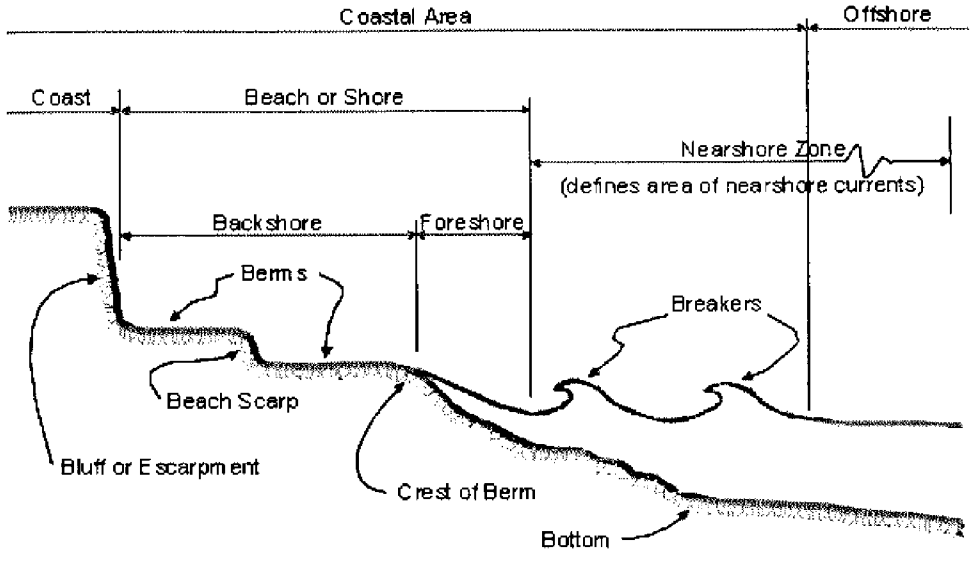

Figure 31. Beach profile and definition of the near shore (US Army Corps of Engineers 1993)

6.1.3.2 Waves

Any casual observer of Lake Erie knows that its water is constantly in motion. Forces associated with waves are the primary agencies of erosion on the coastal area, and waves are created by the wind (Trenhaile 1997). The energy in a wave is related to meteorological factors such as wind speed and duration and is also determined by topographic and hydrographic factors such as distance, or fetch, over which the winds blow, and by the depth of water in the area where the waves are generated. The most dramatic erosion often occurs during storms, partially because the highest energy waves are generated under storm conditions. In addition, storms often produce short-term shifts in lake-levels as water is pushed from one side of a lake to the other, called "setup". The effect of storms is also influenced by wave duration and return frequency.

Wave climate describes the wave characteristics that prevail in a particular region. From hour to hour, day to day, and season to season, meteorological, and thus wave, conditions can vary significantly.

However, when averaged over longer periods of years and decades, both weather and wave climate remain about the same. As a result, since waves are the primary erosion agent, erosion and recession rates will also remain about the same when averaged over longer time periods (US Army Corps of Engineers, 1993).

6.1.3.3 Lake levels

Natural lake-level changes can be divided into three types (CHS 1996): short term (changes within a few days or less), medium term or seasonal (changes within a year), and long term (changes over a few years or more). Short-term changes are due mostly to wind-stress buildup and barometric pressure changes. These changes can cause lake-level fluctuations on the order of 2 to 3 feet for the west shore of Lake Erie. Medium-term changes are lake-wide in effect and are caused primarily by differences in rate of runoff, evaporation, and evapotranspiration (Carter and Guy 1980). A typical seasonal cycle for Lake Erie shows a high in June or July and a low in January or February; the mean difference in elevation between the high and low water stages is about 1.2 feet. Significant long-term changes are caused largely by major changes in the weather within the Great Lakes basin. Weather changes affect precipitation, which, along with secondary factors such as evaporation and runoff, causes long-term changes in the Lake Erie. The record high water levels in Lake Erie of 1952, again during 1972-1973 and once in 1985, have contributed greatly to increased erosion of the shores (Herdendorf et al. 1993).

Because water depth partially influences how and where waves will interact with the coastal area, lake-levels may have an influence on coastal erosion, though they do not cause it. On Lake Erie, the lake-level has no significant effect on any of the forces that cause coastal erosion. Variation in lake levels, whether short or long term, has little effect on the creation of waves, which are the primary erosion agents. Most waves are generated far offshore in deep water where such relatively small water level variations are insignificant (US Army Corps of Engineers 1993). As long as the long-term meteorological and hydrographic factors that determine wave energy remain the same, the long-term erosion rate would remain essentially unchanged. The lake level does, however, have an effect on where wave energy is dissipated on the beach profile, and thus may affect bluff recession rates over short time periods. The lake level is only one of many factors influencing coastal erosion and recession. Up to now, the relative importance of lake-levels compared to the other influencing factors has not been quantified. Observations suggest that along most of the coast, storm duration and return

frequency, and sediment supply have much more influence on coastal erosion and recession than lake-levels.

6.1.3.4 Littoral transport and sand supply

Erosion is part of a greater process known as littoral transport. Littoral transport is the movement of material by waves and currents on the coastline. The material being transported is primarily sand and gravel, with a small percentage of silt-sized particles and rocks. The source of nearly all the sand that is in the littoral transport system of Lake Erie is from the erosion of the bluffs and dunes (US Army Corps of Engineers 1993). Rivers carry very little material.

Littoral transport occurs along the coastline, as well as into the lake and onto the shore. With respect to sand supply, a given length of coastline may have a surplus, be in balance, or have a deficit in its sand supply budget. A sand supply would be in balance for a particular area if the amount of sand leaving the area was being replaced by an equal amount of sand arriving from adjoining areas. Over a short time period, erosion may occur followed by a build-up of sand (accretion), but over the long term, the area would be in a state of "dynamic equilibrium". A large reduction in the sand supply, or a long-term reduction in supply to an area, creates a deficit in the sand budget that must be balanced, usually by increased erosion. Sand supplies influence erosion by supplying the material that builds and maintains beaches, offshore bars, and the general beach profile. These features dissipate wave energy and the absence of these features, where they would normally be present, and usually results in increased erosion.

6.1.4 Study area

As Figure 32 shows, the study area for coastline change analysis extends along the south shore of Lake Erie from Cranberry Creek on the east to Sheldon March State Natural Reserve on the west (mainly the Huron reach). Analysis was completed in all areas where data were deemed by state coastal geologists to be sufficient for realistically estimating long-term coastline change rates. One of the reasons for choosing this area is that both the tabulated recession rate tables from 1973 to 1990 and the coastal erosion area maps are available. This reach covers nearly 10 miles of shore. Cottage associations and

trailer courts occupy the shore zone between Cranberry Creek and Old Woman Creek, and Huron, the only urban area, occupies the remaining of the reach west of Old Woman Creek.

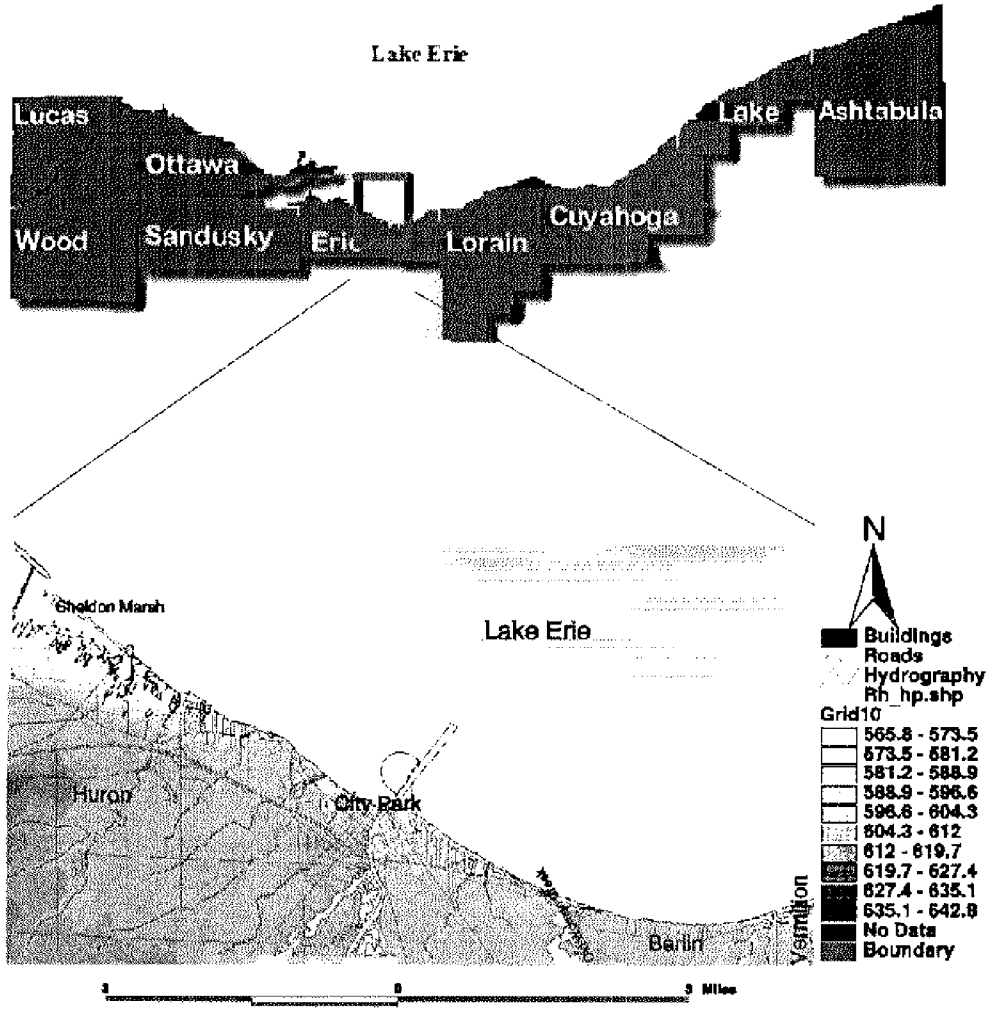

Figure 32. Study area

6.2 Data preparation

Several sources of data are used in this research. This alone demonstrates one of the well-recognized reasons for using GIS – the integration of disparate data sets. Considering the factors that may influence the forces of coastal erosion and the nature of applications of GIS, there are four primary sources in this case. Bear in mind, not all data sets will be used for data analysis, some of them are for meeting the requirements of cartographic designs and map presentation.

6.2.1 Historical Coastline data

Currently, historic linear data provide us with the ability to assess future changes in the shape of the coastline by reviewing historic snapshots of the coastline. The long-term rates of change provide mangers and property owners with a clearer picture of the potential hazards confronting coastal development (Dusen 1997).

First of all, the tabulated recession rate data between 1973 to 1990 for study area in digital form was acquired from the Ohio Department of Natural Resources (ODNR). Recession rates were determined by comparing the position of bluff lines shown on 1:10,000-scale U.S. Lake Survey charts and more recent 1:12,000 to 1:4,800 scale aerial photographs from the 1930's to 1990 (Mackey and Guy 1994). Bluff-line positions from these charts and photographs were transferred to 1:2,400-scale enlargements of aerial photographs taken in 1990. Positions of the transferred lines were then digitized along approximately 7000 shore-normal transect spaced 30 meters apart. Secondly, ODNR also provides Lake Erie Coastal Erosion Area Maps, which are part of the results from Ohio Coastal Management Program. These maps have been revised from the preliminary identification of Lake Erie coastal erosion areas released on September 30, 1996. These maps also show the location of the digital transects and recession lines for 1973 and 1990, respectively.

Coastal erosion studies have long employed aerial photography, so historical aerial photographs should be available for deriving the long-term recession rate. An aerial photographic search conducted for the study area located in Erie County of Ohio is shown in Table 15. In order to accumulate data for monitoring long term coastline changes, aerial photographs of coastline should be taken every 5 years (Li 1995). The photographs should have at least 60% along shore overlap so that the 3D coastline can be extracted from the photographs by stereo photogrammetric processing. For coastline segments eroded serially, larger scale aerial photographs should be taken more frequently, for example every 1-3 years. The larger scale photographs may also be used for other purposes such as coastal zone topographic mapping, beach profiling, and erosion interpretation. Besides, for very small sites, total stations and GPS receivers may be used to capture the coastline periodically and compare the coastline changes.

Date	Mission #	Frame Numbers	Scale
4/29/97	9710913	014, 015	1: 19.2K
6/14/73	5258	1: 001, 002	1: 24K
3/28/68	3881	22:575 through 579 23:580 through 583	1: 4.8K 1: 4.8K
1/25/62	2207	4: 097 through 100	1: 9.6K
11/23/60	1740	1: 001 through 003	1: 9.6k
7/29/58	1104	3: 042 through 045	1: 9.6K
3/05/49	198v	8: 078 through 087	1: 4.8K

Table 15. Aerial photographic search result for the study area located in Lake Erie

6.2.2 Bathymetric data

Bathymetry of Lake Erie exceeding in detail any previous Bathymetry, is available from NGDC (NOAA National Geographical Data Center) in Arc/Info™ format. The Bathymetry was compiled using all good quality historic hydrographic sounding data collected since 1903 from the NOAA National Ocean Service and its predecessor agency for Great Lakes Surveying, the Army Corps of Engineers, and the Canadian Hydrographic Service.

Digital sounding data combined with sounding data archived only on paper were used in the compilation. Tracking density ranges from about 125 meters to 500 meters for near shore areas and 500 meters to 2500 meters for the open lake regions. For the study area, the sounding lines are less than 500 meters apart. Coordinate system transformation is necessary while integrating other layers. The bathymetric data horizontal datum is not consistent since it is a compilation from many sources but it is in geographic coordinate system, i.e. latitude and longitude. We transformed the horizontal coordinate system using Arc/Info Projection tool, from geographic coordinate system DD to Zone 17 of UTM (NAD 1927) to fit with USGS data. The vertical information is referenced to the low water

datum for Lake Erie. The adopted mean low water datum is 570.5 feet above the mean sea level. Using Arc/Info we convert the depth Z to height using

$$\text{Height} = 570.5 - Z \tag{17}$$

Bathymetric data are crucial to structure design, hydrological modeling, and coastline change monitoring. The data acquisition is usually very expensive. The accuracy of the bathymetry files that we got is low and therefore in the next phase of the project we will try to get data with higher accuracy.

6.2.3 Topographic data

Though there is no definitive map base regarding the GIS applications of coastal zone (Maslen et al. 1996), most of the data layers are referenced to topographic maps, especially the 1:24,000 scale USGS maps. At this moment, the GIS Support Center of the Ohio Department of Administrative Services will provide access to and distribute the 1:24,000 scale Digital Line Graph (DLG) files based on the 7.5 quadrangles covering the State of Ohio. The layer categories include Boundary, Hydrography, Public Land Survey System (PLSS), Transportation, and Hypsography. All of Huron and part of Vermilion West quadrangles will be used in this research corresponding to the study area. These data cover the features on the landside of the coastline. Digital Elevation Models (DEM) describe the land terrain relief which, along with the bathymetric data and water level data, determine the coastline shape and other characteristics.

6.2.4 Time series data

While implementing coastline management based on GIS, the time dimension must also be incorporated into GIS data models even in the simplest way by recording when the data were collected and how often it is likely to get updated (Maslen et al 1996). GIS applications can model cyclical processes such as tidal current movements allowing predictions to be made for the dispersal of pollutants while 'scenario predictions' can be computed as a result of spasmodic events such as storm flooding. So, water levels, wave data, wind data, wave surface elevations (tides), river data (daily discharge), and other times series data can describe the processes affecting the coastline and the other coastal phenomena. Fortunately, these data now can be acquired from some real-time systems, e.g. the

Great Lake Forecasting System (GLFS), including water levels, wave, wind, temperature, tides etc.; Lake Erie Homepage-US Army Corps of Engineers, including water level, storm rise, outflows, weather etc. In this part of research we will take the GLFS water level files and transferred them into standard GIS input files. The water level files is updated every 24 hours, and it is basically a matrix of 209*57 height elements. This grid file is rotated 27.33° and has a 2000 meter grid interval. The reference point for this file is (40.9700012N, 82.98345182W) or (333103.82, 4537109.55) in meter in UTM.

6.2.5 Others

The changing position of the coastline, the toe of the bluff, and the top of the bluff can be quantified using the image processing software developed for the 'Remote Video Monitoring System' (http://coastal.er.usgs.gov/erie/). These terrestrial and aerial photographs are available for coastline sections of different periods. They are important for interpreting erosion status. Hardcopy photos that were taken during site visits are scanned and saved in TIFF format. The scanned images are then related to the desired features in GIS and can be displayed by clicking the corresponding segments of coastline through a using the hot link.

7. Spatial Analysis

7.1 Modeling the coastline - dynamic segmentation model

A typical coastal system may involve several tens of kilometers or more of coastline. The width of the corresponding coastline/zone (depending on how this is defined) may be no more than a kilometer or two, and any data referenced in the third dimension will only rarely exceed scales of 10-100m at most. These extremes of scale mean that polygon data structure will not give a good representation of the coast. Treating the coast as a linear entity can be performed using the conventional arc-node model whereby each line segment or arc is defined in relation to its starting and end nodes. In this model the topological relationships between features are easily preserved, an important feature for analysis of networks. However this model is inflexible with regard to handling large amount of attributes on a line. A more appropriate model is the Dynamic Segmentation model. Within the data structure a line is segmented or divided into homogenous sub-units, by recording the location of a change in attribute or an event in terms of distance along the line from a specified origin or

topological node. Attributes can be defined along a linear feature spanning many arcs or, alternatively, a single line may have multiple attributes assigned to different portions of the same arc. In the implementation of dynamic segmentation provided by Arc/Info™, the term *route* is given to any linear feature (such as highway, river, coastline, etc.), regardless of the number of arcs that make up its representation within the database. In a coastline GIS, the shore can be viewed as a route system consisting of several routes, each representing different parts of the shore (Li 1996, Bartlett et al. 1997). In our case we segmented the coastline with as close as possible to the recession rate maps supplied by ODNR from Frame No. 487 to Frame No. 008 of Erie County (Figure 33).

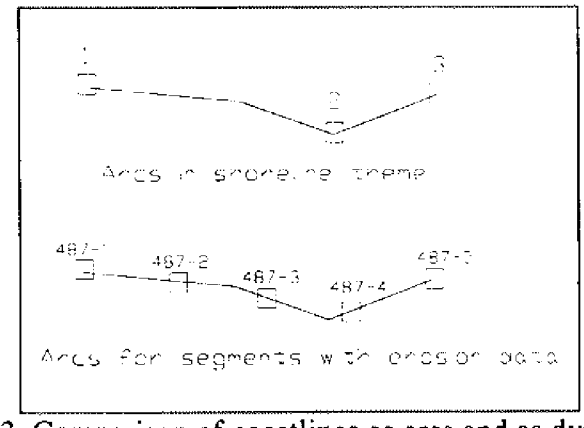

Figure 33. Comparison of coastlines as arcs and as dynamic segments

Following the creation of route-system that include route and section attribute table we linked the entire data table (recession table) to the route-line to create our coastline theme (Table 16).

ROUTELINK #	FROM	TO	FRAME	TRANS	STD	STR	YRS
1	0.000	29.438	ERI487	487- 1	16.10	0.95	17
1	29.438	58.879	ERI487	487- 2	3.40	0.20	17
1	58.879	88.318	ERI487	487- 3	42.80	2.52	17
1	88.318	117.745	ERI487	487- 4	30.30	1.78	17

Table 16. Example of a linear event table (Trans-transect number, Std-Recession distance, Str-recession rate, Yrs-elapsed years)

7.2 Prediction of coastline position

Rates of Coastline position changes are frequently employed to summarize historical coastline movements and to predict the future based on those perceived historical trends. The data used to calculate a coastline rate of change consist of a number of coastline positions recorded at one place (e.g. transects or monuments) over time.

Coastline position data sources include historical maps, maps compiled from aerial photographs and aerial photographs. Each coastline point possesses a degree of uncertainty arising from the difficulty of precisely locating the coastline datum to other sources. A rate of change statistic implicitly assumes that coastline movement is constant and uniform (i.e. linear) through the time concerned. In realty this is not the case. Further uncertainty regarding the accuracy of coastline rate of change predictions thus arises from using linear methods to summarize nonlinear, cyclic, or chaotic coastline behavior. Several methods have been used to predict beach loss as a function of time or sea level rise. Some of the non-linear methods employ complex mathematical models such as higher-order polynomials, exponential, or cyclic series. Nevertheless, the method most commonly used by coastal land planners and managers to predict future coastline changes is extrapolation of a constant rate-of-change value. The popularity of this method is due chiefly to its simplicity (Fenster et al 1993). As with any empirical technique, no knowledge of or theory regarding the sand transport system is required. Instead, the cumulative effect of all the underlying processes is assumed to be captured in the position history.

For the purpose of predicting the future coastline positions for the study area, simple methods or models have been used, such as the *End-Point Rate* (EPR) method, or *Linear Regression* (LR). Linear regression uses all the available data from many data sets to find the line, which has overall minimum, squared distance to the known points. However in the area of our search coastline data sets does not contain a statistically acceptable sample size or span an appropriate time period in order to justify the use of non-linear or LR model. Instead in this research we used a simple EPR model (Fenster et al 1993). The future coastline position for a given date is then estimated using the resulting rate (slope) and coastline position intercept:

$$\text{Coastline Position} = \text{Rate} * \text{Date} + \text{Intercept} \quad (18)$$

If we use Y to denote the predicted coastline position, X for date, B for the intercept, and m for rate of coastline movement, the above equation can be expressed as:

$$Y = mX + B \quad (19)$$

Given n coastline position observations ($Y_1, \ldots Y_n$), numbered in ascending order by date ($X_1, \ldots X_n$), the EPR rate is:

$$m_{EPR} = (Y_n - Y_1)/(X_n - X_1) \quad (20)$$

The EPR intercept is:

$$B_{EPR} = Y_1 - m_{EPR} X_1 = Y_n - m_{EPR} X_n \quad (21)$$

Since the end point line can extend beyond the most recent point (X_n, Y_n), equation (19) can be rewritten to use that position (Y_n), and the elapsed time ($X-X_n$):

$$Y_{EPR} = m_{EPR} * (X - X_n) + Y_n \quad (22)$$

We computed the future coastline positions for year 2015 using EPR model in two methods. One is using buffer operation, the second is a small application specially developed in a CAD environment. Buffer is defined as an area containing locations within a given range of a given set of features, and is useful for proximity analysis. The generation of buffer can be based on either a certain distance (constant-width) or a look-up table (variable-width) in Arc/Info™ (ESRI 1997). Then we eliminate the wrong side of buffer zone. First, we need to create a look-up table, and only two columns are needed in this table; that is, key-item and distance from input coverage. The key-item is Trans (i.e. segment number), and distance is derived from annual recession rate (feet/year) multiplied by 25 (based on 1990). Next, we performed buffer function along coastline coverage and removed lake-ward buffer zone. The EPR program runs on the coastline-coordinate file. It computes the difference between both data sets and predicts the future line.

Both methods performed well. The difference between the methods is that the buffer operation uses the recession table as an input and the program performed comparison between two given lines.

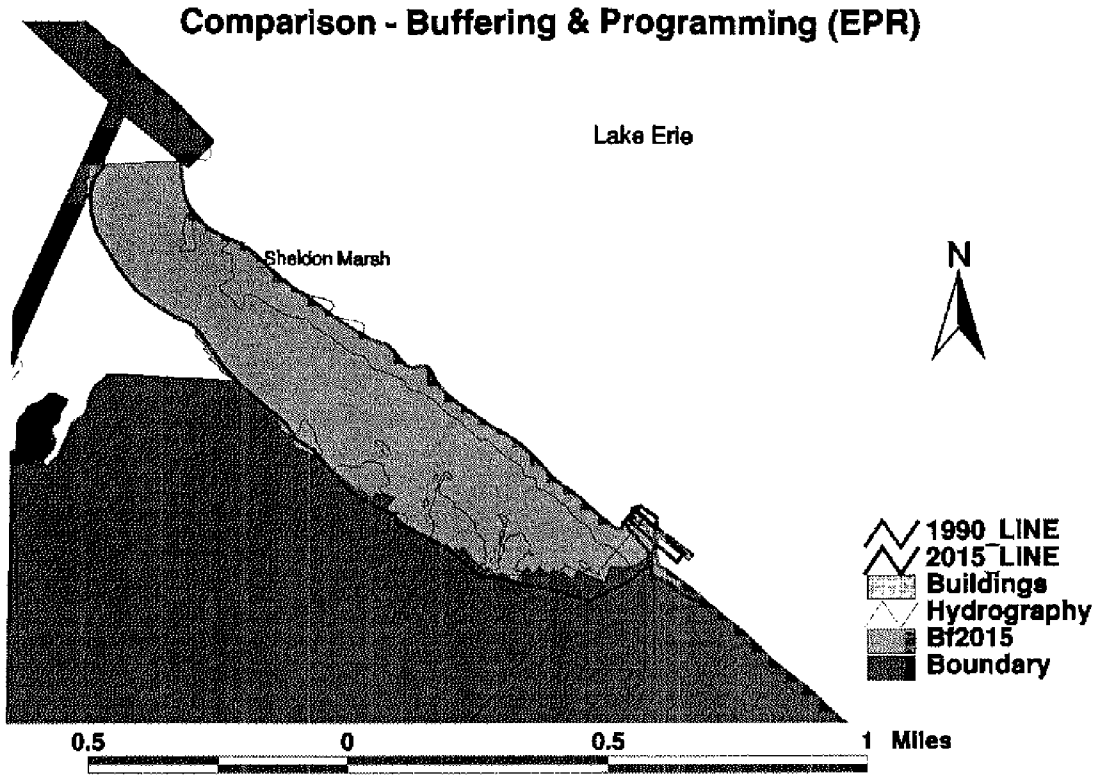

Figure 34. Comparison of buffer operation (Bf2015 zone) and EPR program (2015 line) to predict future coastline

7.3 Computation of coastline using water-level data.

Figure 35 describes a proposed method that will compute instantaneous coastline using an updated digital Coast Terrain Model (CTM) and desired water level data. There are three types of input data for this computation:

- The bathymetric data which usually remain constant. They are updated whenever new sounding data of the area is acquired, for example, by ODNR or other agencies.
- CTM that should be derived from updated aerial photographs or one-meter resolution satellite imagery. The interval of CTM updating should be corresponding to erosion rate of the area. At this stage we obtain this information from USGS 7.5 quad DLG files for developing the method. We plan to have at least two sets of satellite images, one for low water level and another for high water level.

- Water level data at desired time point will be taken from the Great Lake Forecast System. The data will be transformed to GIS. After datum transformation they will be integrated with the bathymetric data and CTM for computing the desired coastline.

All three data sets will be transformed to Arc/Info coverages. If USGS DLG is used, we will convert the contour line information into a GRID file where each pixel represents a grid point. First, the CTM and bathymetric data are combined to form an extended Grid. Once in the same datum, we will subtract the water level grid from the extended CTM grid. The interpolation for new grid points is based on Hutchinson (1996). This interpolation procedure uses an iterative finite difference method (i.e. inverse distance weighted interpolation) without losing the surface continuity of global interpolation methods (e.g. Kreiging and splines). It is essentially a discretised thin plate spline technique where the roughness penalty has been modified to allow the fitted CTM to follow abrupt changes in terrain, such as streams and ridges. The resulting grid file gives a coastline where elevation difference is 0. The last step in our process is converting the zero cells into a line coverage using the GridLine command.

7.4 An alternative way for quantifying coastline changes

In this section we present an alternative way for quantifying coastline changes based on some operations of GRID module in Arc/Info™ and implemented in ArcView™ (Figure 36).

The preparation work is to collect sets of 1973 to 1990 aerial photographs and 1:24,000-scale hard-copy maps for the study site from ODNR. Then we used a high accuracy digitizer to digitize two sets of 1973 and 1990 coastline data in AutoCAD as DXF files, respectively. Finally, we used the DXFARC command to convert the coastline data into two Arc/Info™ coverages.

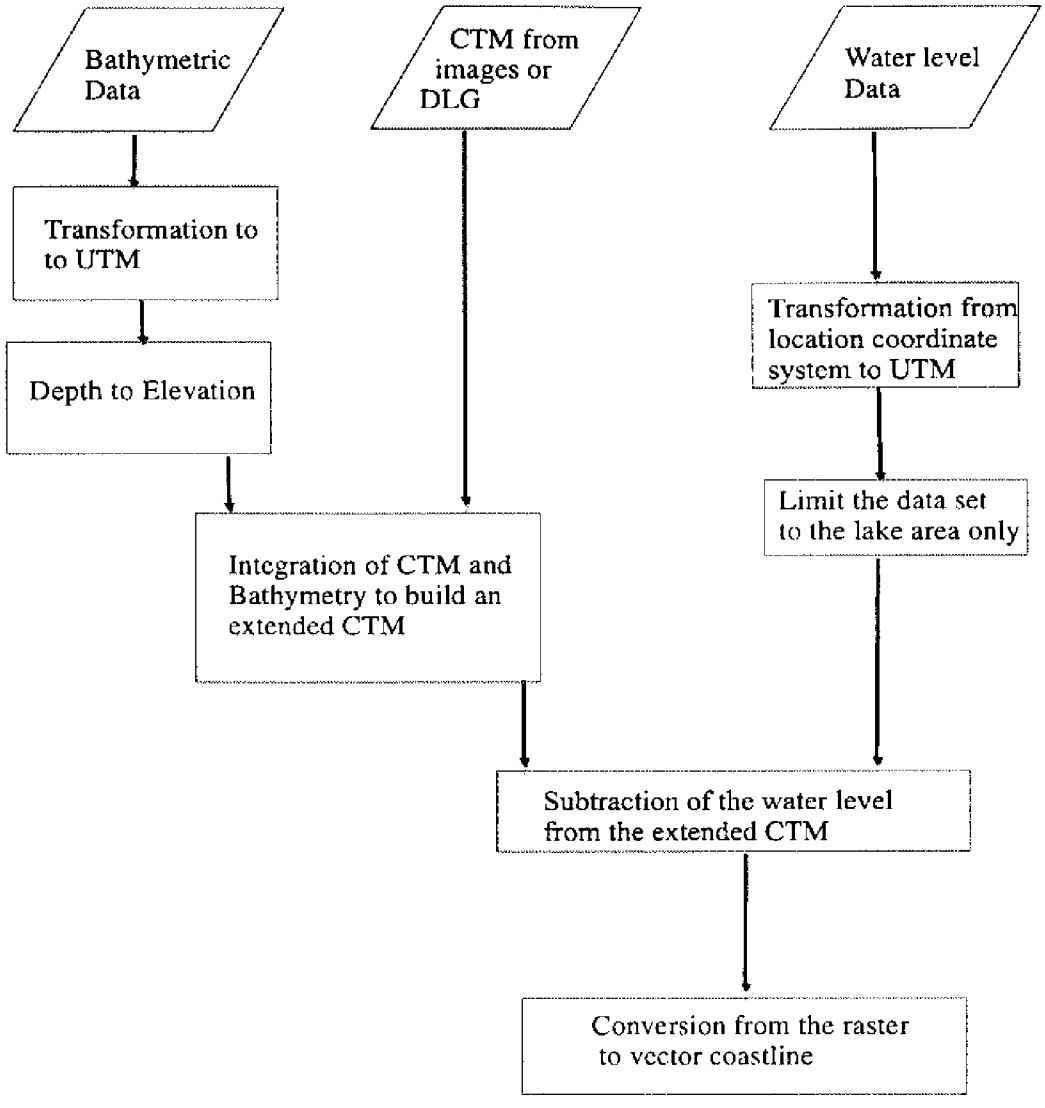

Figure 35. Computing Coastline using water-level data.

First of all, the LINEGRID command is used to convert both coastline coverages into grid coverages with one-meter cell size after topology was built up. In the resulting grids, cells which fell at the position of the 1973 or 1990 coastline were coded as "1973" and "1990", respectively. All other cells were coded as NODATA (defaults).

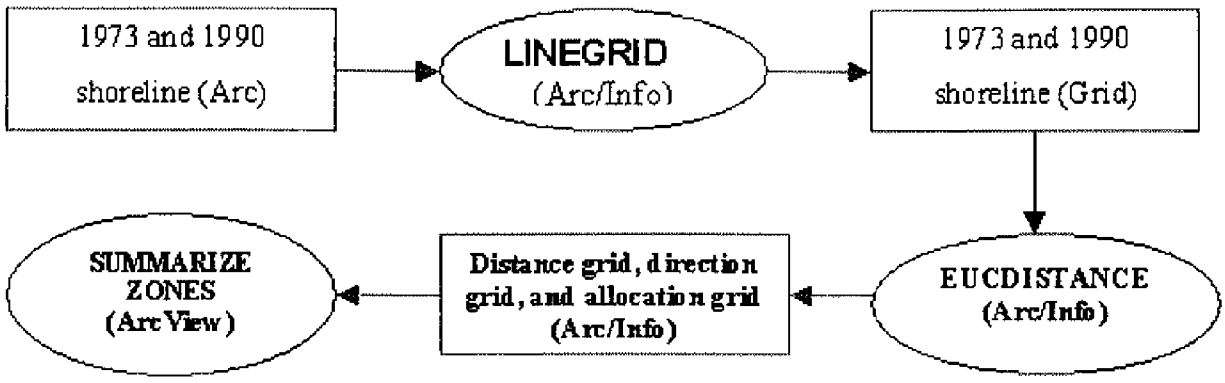

Figure 36. Procedure for quantifying coastline changes

Secondly, the EUCDISTANCE command is employed to create a new grid from the 1973 coastline grid. This function calculates the Euclidean distance of every cell in the new grid to the nearest concurrence of a specified value in the original grid (ESRI 1992). In this case, the specified value was the code "1973" in the 1973 coastline grid. The resulting grid looks like a buffer around the original 1973 coastline grid (Figure 37). Unlike a buffer polygon, this buffer was composed of individual cells, each of which contained a distance value.

	1	1			
		1			
2					

Source_Grid

=

1.0	0.0	0.0	1.0	2.0	3.0
1.4	1.0	0.0	1.0	2.0	3.0
2.2	1.4	1.0	1.4	2.2	3.2
2.0	2.2	2.0	2.2	2.8	3.6
1.0	1.4	2.2	3.2	3.6	4.2
0.0	1.0	2.0	3.0	4.0	5.0

Euc_ Distance__Grid

Figure 37. An example of EUCDISTANCE command (ESRI 1992)

The intersection between the distance grid and the 1990 coastline grid created earlier is a new grid. The intersection was done using the conditional statement: "If the coastline grid cell contains the code

"1990", put the value of the distance grid at that location in the new grid, otherwise put a NODATA value there". The result of this statement was a grid containing the distance to the nearest 1973 cell at the position of each 1990 cell.

Next, we can either use the Graph command (under Arcplot module) or import the last grid file into ArcView™ to quantify the coastline change. The second method is the one we chose for this research. Finally, importing the third grid file into ArcView™ and performing the SUMMARIZE ZONES function, we derive a table which describes the distance of coastline change from 1973 to 1990. The output results are displayed in Figure 38-39.

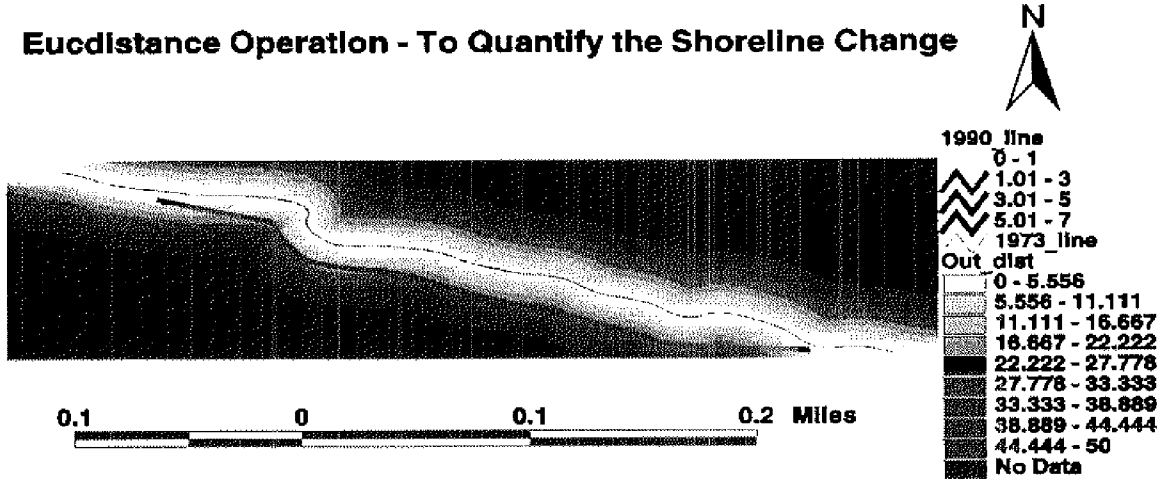

Figure 38. Euclidean distance grid of 1990 coastline

7.5 Intermediate analysis results

Many factors act together to result in erosion and some of the causes are discussed in the following sections, including geological materials, terrain slope, and effects of human activities. We will focus on the analysis of erosion causes based on the function model of GIS and present some intermediate results and output of the system. These results serve to demonstrate the tools that we have developed. However since we used test data that are available to us and the system is still in development, the results should be treated as intermediate and subject to changes. Figure 40 illustrates the linkage between parts and modules of the system.

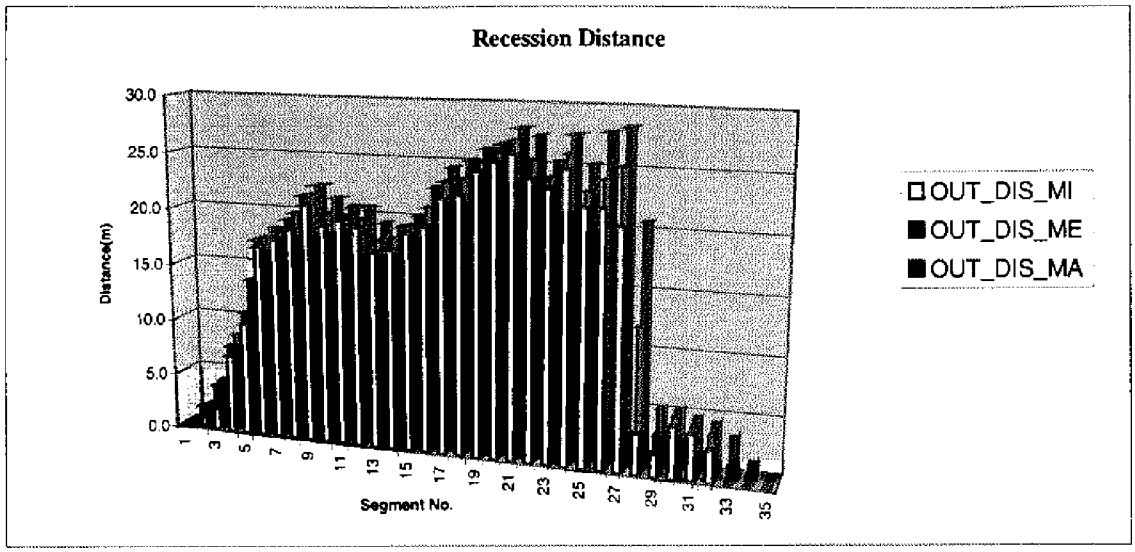

Figure 39. Recession distance of study site from 1973 to 1990

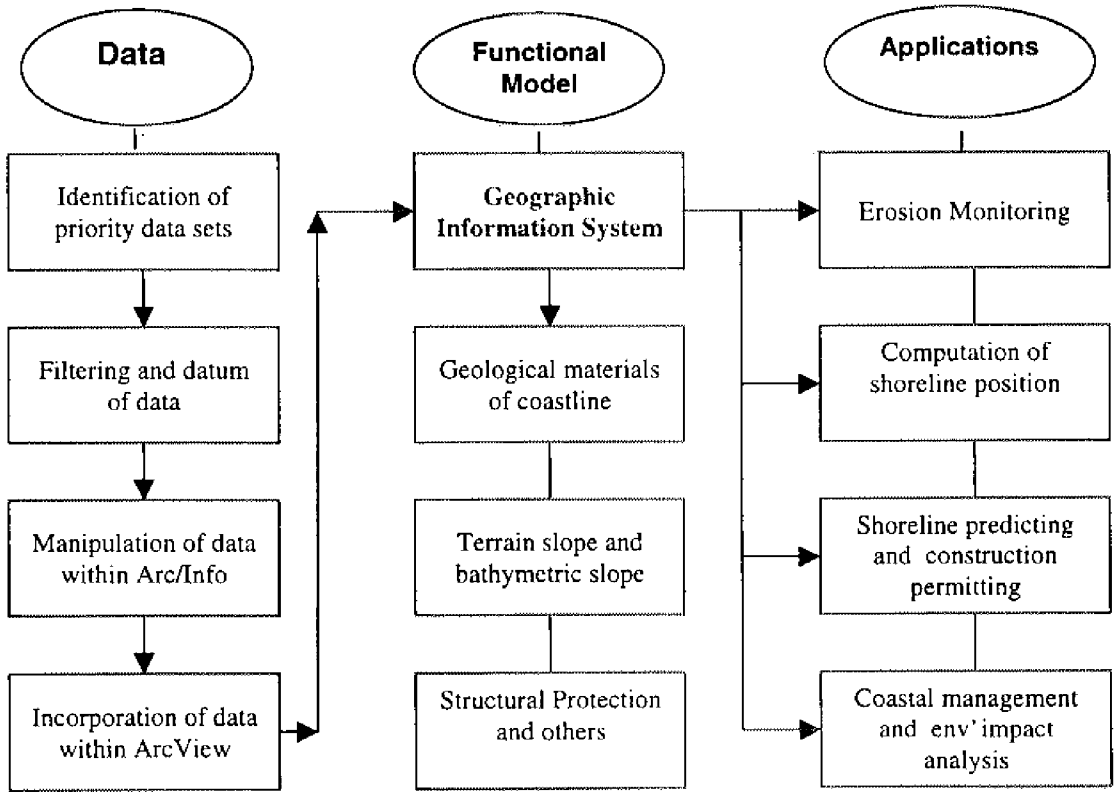

Figure 40. Linkage of data model, functional model, and applications.

7.5.1 Effect of geological materials

In addition to wave forces, coastline geology has a direct impact on erosion. According to the investigation of ONDR, 74% of the Lake Erie lakeshore is composed of easily eroded materials (e.g. sand, till, and clay). In the study area, most stretches of coastline are composed of sand/till- or clay/till-bluff and are easily eroded. The average bluff height is 25-30 feet from Cranberry Creek to Old Woman Creek, 10-15 feet from Old Woman Creek to Huron River, and 6-15 feet from Huron River to Sawmill Creek. The reaches of Sheldon Marsh are composed of sand beaches.

An event table for implementation of geological materials is shown in Table 17. The data is compiled from "Cross section of shore stratigraphy, Erie and Sandusky Counties" (Carter and Guy 1980) and "Engineering geology maps of the Ohio Coastline of Lake Erie" (Pincus 1960).

ROUTELINK#	FROM(m)	TO(m)	CATEGORY
1	0.0	5500.0	Till
1	5500.0	7628.0	Clay
1	7628.0	11279.0	Till
1	11279.0	11790.0	Clay
1	11790.0	14998.0	*Sand*

Table 17. Event table for coastline materials

Figure 41 shows a relationship between geological materials of coastline and recession rates. Where the shore is composed of till, rates are higher and have a greater range of values than where the shore is composed of clay. Along the sand spit, rates were either less than 1 feet/year or as high as 45 feet/year. Low rates occurred along the protected stable part of the spit, and high rates occurred along an unprotected unstable part of the spit (Sheldon Marsh).

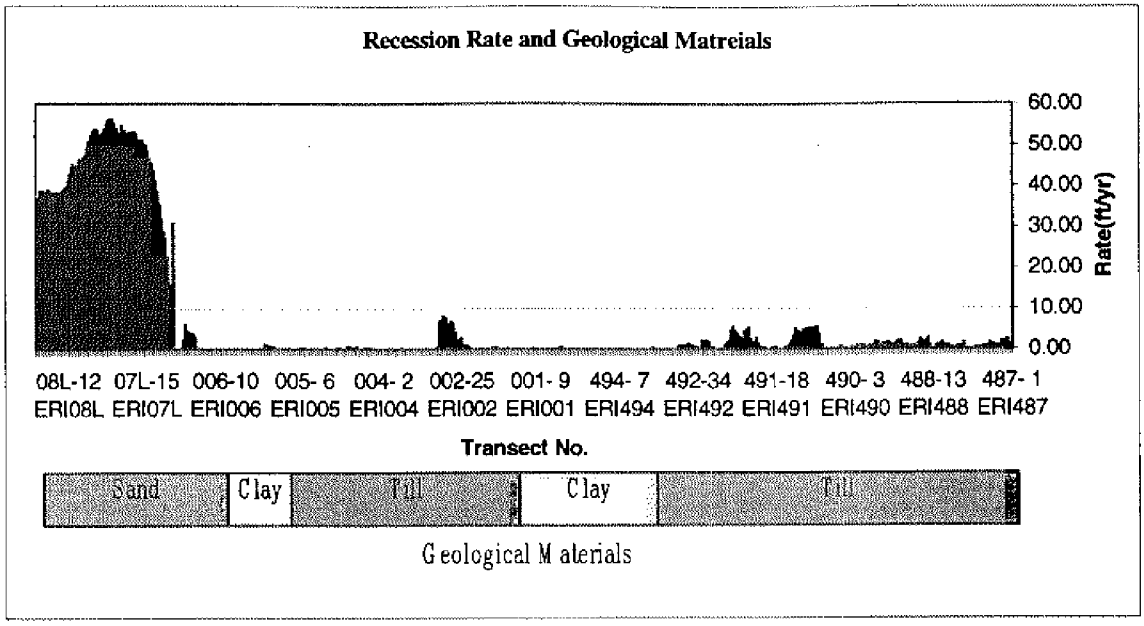

Figure 41. Recession rate and geological materials of the study area.

7.5.2 Terrain/bathymetric slopes

The slope angles (Figure 42) for terrain can be derived based on the DEM theme by using *slope* calculation function in ArcView™. Derived slope identifies the slope, or maximum rate of change, from each cell to its neighbors. The output slope grid theme represents the degree of slope (e.g., 5 degree slope) for each cell location.

Basically, slope angles are a measure of gradient magnitude and influences. For coastal GIS, it can be employed to analyze the relationships between recession rate and near-shore slope angles (Figure 43). Generally, reaches of coastline with higher slope should have higher recession rate. But, by inspecting Figure 43 we can not definitely tell whether transects with higher near-shore slope angles have higher recession rates. The possible reasons for this are: a) the bathymetry data could not support detailed analysis, both because of the poor accuracy and low resolution; b) the bathymetry slope difference is not so high and thus its influence with respect to other factors (wind direction, geology structure, human structures etc.) is negligible. This Figure will be reinvestigated in the next phase of the research using a better terrain model.

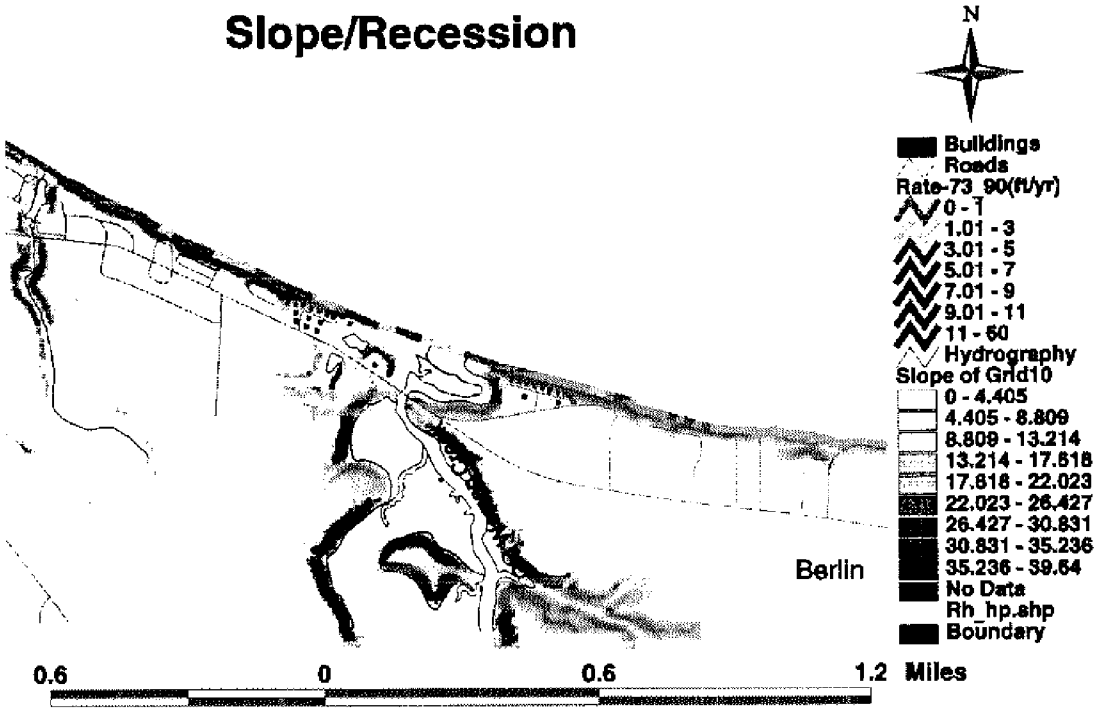

Figure 42. Terrain slope of the study area

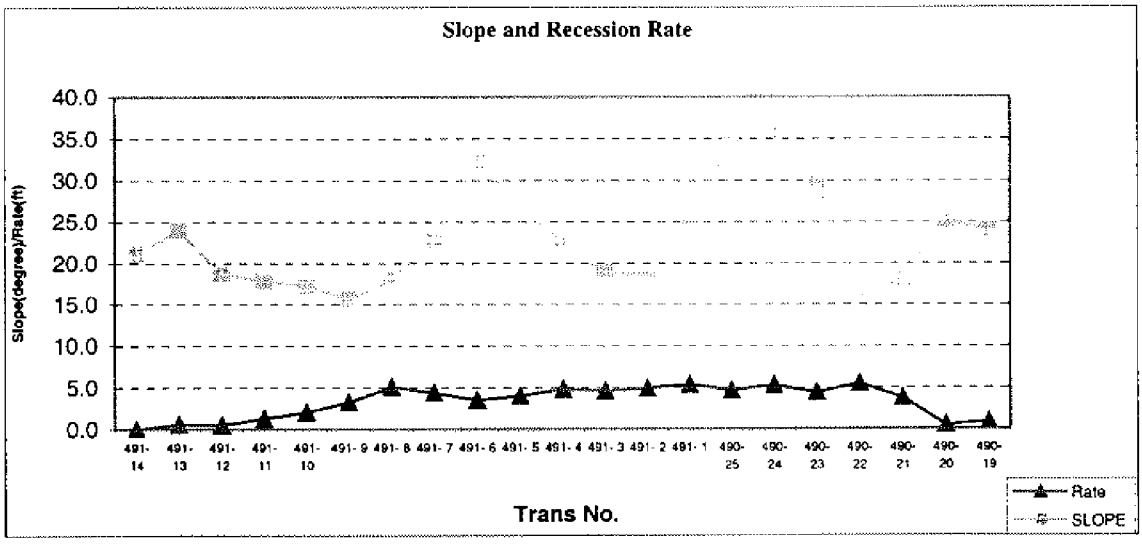

Figure 43. Recession rate and terrain slope angle

7.5.3 Structural protection and Erosion Monitoring

Structural protection against coastal erosion can have a significant consequence on the erosion process. Knowledgeable professionals can help to ensure successful protection against erosion. Poorly designed or improperly installed devices may actually accelerate erosion by changing the ways in which the coastline can be used. For instance, the groins have produced tiny pocket beaches; seawalls have reduced the amount of sand leaching from the bluff, slowing beach formation. Larger projects, such as Huron jetties and breakwater, have built crescent beaches, but in turn, have started the down-drift shore of sand. So, structural protection should be attempted only after the site has been carefully evaluated and appropriate control measures designed.

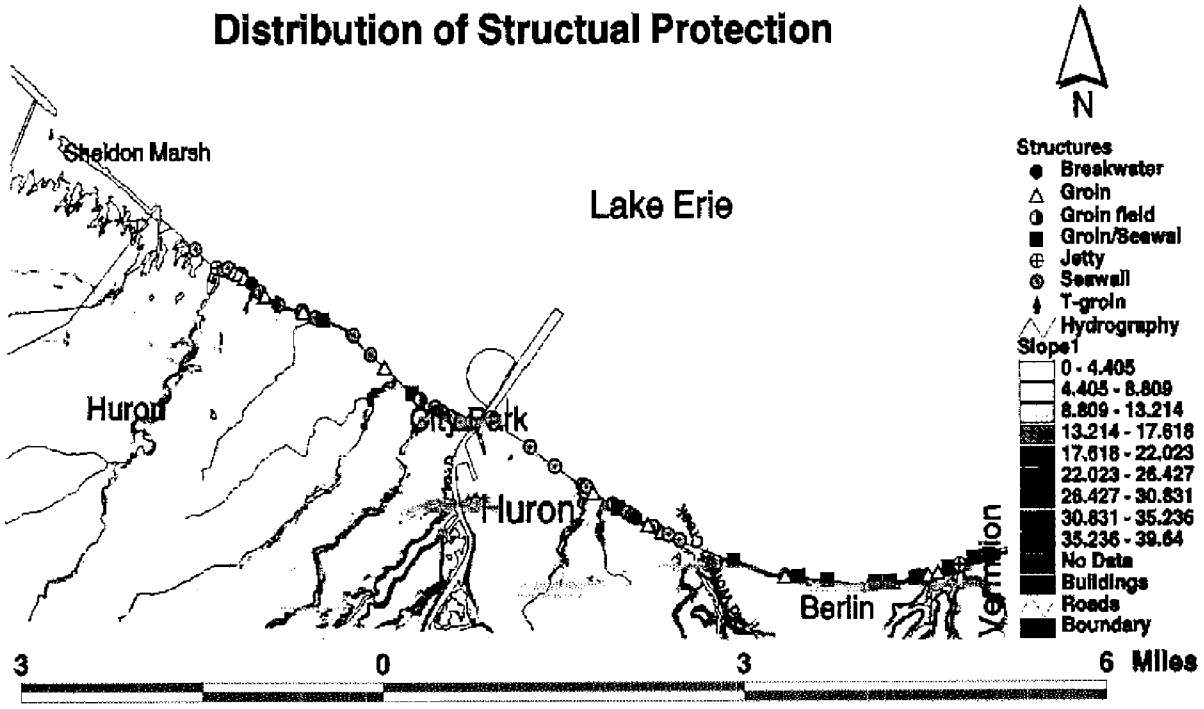

Figure 44. Distribution of coastline protection in the study area

Our system presents the protection structure along the shore with their type (Groin, seawalls, jetty, breakwater etc). Comparing this data with the erosion information we could easily observe that transects without structural protection like Sheldon Marsh had a very rapid recession rate. Figure 45 demonstrates the overall effect of human activities. Though there are more areas with very slow erosion the new protection structures have also created areas with rapid erosion. These results should be reexamined with new and accurate data due to the following reasons: The 1973-1990 period is

shorter compared with the two other time spans and it may be that erosion effect should be compared on two equal time intervals. The accuracy of the data from early years 1937-177 is low and did not have any quality control.

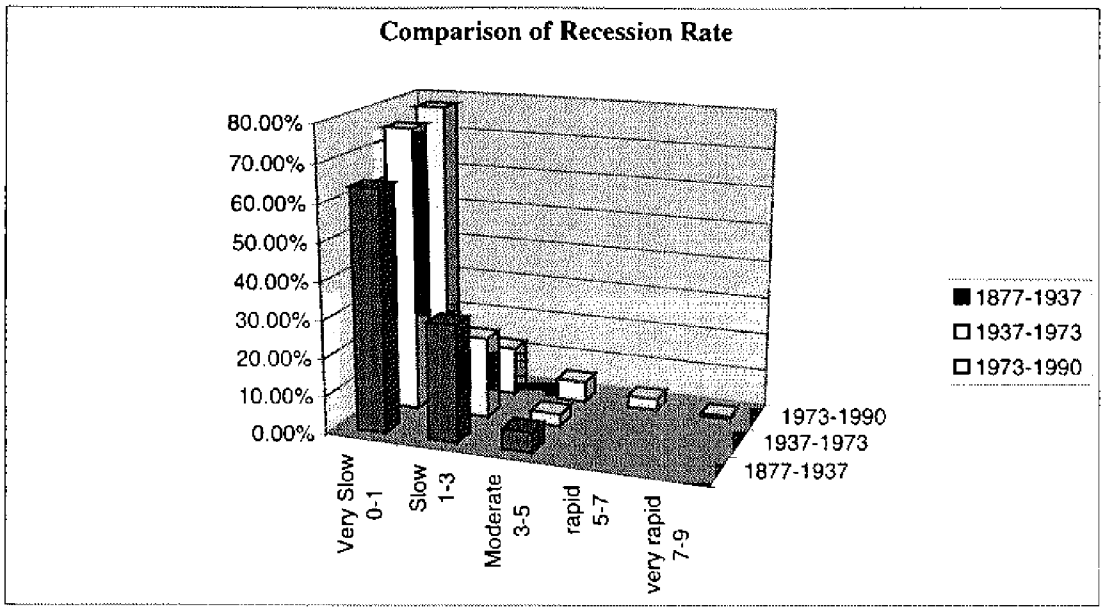

Figure 45. Comparison of recession rate between 3 time intervals

8. Conclusions

Processing of high resolution airborne and satellite imagery has been studied in this research. The simulation study provides a tool for examining overall accuracy potential of the one-meter resolution satellite imagery. One to four GCPs are recommended for computing high accurate ground points and reducing costs. Distribution of GCPs along a straight line is not to increase accuracy of ground points. Estimated ground point accuracy through the simulation is 3m (X and Y) and 2m (Z) with 24 GCPs, and 12m (X and Y) and 12m (Z) without GCPs. Based on the experimental results of HRSC and MOMS-02P data processing, it is to conclude that the first version of bundle adjustment software system for processing high resolution satellite imagery is appropriately designed and implemented. In addition, higher precision navigation data is largely helpful to geometric accuracy of ground points in the case of weak distributions of GCPs and/or few or no GCPs. A well spread distribution of even a few GCPs is still more beneficial to accuracy improvement than a dense but poorly spread distribution. The model and software system will be improved and completed in the second project year for

IKONOS-I data processing. Algorithms for extracting coastlines and change detection in Lake Erie area will be developed.

We have prepared the first set of tools that can automatically predict coastline positions and analyze different parameters and factors influencing erosion rates. Many of the methods presented here were performed manually. In the next phase of the research we will put more emphasis on automating the series of commands in a better user interface. This will allow us to handle data more efficiently and to analyze a larger database, which can yield more significant results. The Great Lakes Forecasting System provides an excellent on-line source of data. We learnt the data format of GLFS and we presented how we are to use water level data and the extended CTM for digital coastline determination. We will verify the above and future results with one-meter resolution satellite imagery. This requires us to continue to develop specifically designed methods and tools. Impact analysis of coastline changes will be performed based on the data collected from the updated images.

Acknowledgment

We appreciate the funding from Sea Grant–NOAA National Partnership Program. Funding and assistance from CSC, OCS, and NGS of NOAA are appreciated. We would like to acknowledge the assistance in GPS survey from Mr. David Albrecht of Ohio Department of Transportation (ODOT) and Dr. Dorota Grejner-Brezezinska of Center for Mapping. We thank Dr. Scudder Mackey and Dr. Don Guy of Division of Geological Survey/ODNR for providing erosion and spatial data and Beth Pratt of Division of Engineering/ODNR for participation in the project. Discussion with Mr. David Conner, NOAA geodetic advisor to Ohio, on geodetic datum issues was very helpful. Our thanks go to Dr. Charle Toth and Mr. Panny Zafiropoulos of Center for Mapping, Dr. Franz Wewel and Dr. Yun Zhang of Institute of Planetary Exploration/DLR, and Dr. Dieter Fritsch and Mr. Michael Kiefner of University of Stuttgart for providing data and assistance in handling AIMS, HRSC and MOMS-02P, respectively.

References

Bartlett, D., R. Devoy, S. Mccall and I. O'Connor 1997, A Dynamically Segmented Linear Data Model of the Coast, *Marine Geodesy*, Vol. 20, pp. 137-151.

Bossler, J. D. 1996, Airborne Integrated mapping System, *GIM*, July, pp. 32-35.

Carter, C. H. and Guy, D.E. Jr. 1980, Lake Erie Shore Erosion and Flooding, Erie and Sandusky Counties, *OHIO: Setting, Process and Recession Rates From 1877 to 1973*, pp. 1-129.

CHS 1996, Fluctuations in Lake Erie – Types, Department of Fisheries and Oceans, Canadian Hydrographic Service, *http://chswww.bur.dfo.ca/danp/fluctuations.html*.

Corbley, K. 1996, One Meter Satellites: Practical Applications by Spatial Data Users, *GeoInfo System*, Vol. 6, No.7, pp. 28-33.

Dusen, C. V. 1997, Vector Based Shoreline Change Analysis, *ESRI'97 User Conference Proceedings*, ESRI, http: //www.esri.com /base /common /userconf /proc97 /proc97 /home.htm.

Ebner, H. and G. Strunz 1988, Combined Point Determination Using Digital Terrain Models As Control Information, *Int. Arch. Of Photogrammetry and Remote Sensing*, Vol. 27, Part B11, pp. III/578- 587.

Ebner, H., W. Kornus and G. Strunz 1991, A Simulation Study on Point Determination Using MOMS-02/D2 imagery, *Int. Journal of PE & RS*, Vol.57 No.10, pp.1315-1320.

Ebner, H., W. Kornus and T. Ohlhof 1992, A Simulation Study on Point Determination For The MOMS-02/D2 Space Project Using An Extended Functional Model, *Int. Arch. of Photogrammetry and Remote Sensing*, Vol.29, Part B4, pp.458- 464.

Ebner, H., T. Ohlhof and E. Putz 1996, Orientation of MOMS-02/D2 and MOMS-2P Imagery, *Int. Arch. of Photogrammetry and Remote Sensing*, Vol. XXXI, Part B2, Wien, pp. 158- 164.

ERSI 1997, Understanding GIS The Arc/Info Method, self-study workbook, version 7.1 for Unix and Windows NT, *ESRI*, Redlands, CA.

ERSI 1992, Arc/Info Use's Guide, V 6.0 GRID Command References, *ESRI*, Redlands, CA.

Fenster, M. S., R. Dolan and J. F. Elder 1993, A New Method for Predicting Shoreline Positions from Historical Data, *Journal of Coastal Research*, Vol. 9, pp.147-171.

Folchi, W. 1996, Satellite Orthoimagery: Mapping the Future Today, The Space Imaging Approach, *Proceedings of ACSM/ASPRS Annual Convention & Exposition*, Baltimore, MD, Vol. 2, pp.74-81.

Fraser, C. and J. Shao 1996, Exterior Orientation Determination of MOMS-02 Three-Line Imagery: Experiences with the Australian Testified Area, *Int. Archives of Photogrammetry and Remote Sensing*, Vol. XXXI, Part B3, pp.207-214.

Fritsch, D., M. Kiefner, D. Stallman and M. Hahn 1998, Improvement of the Automatic MOMS02-P DTM Reconstruction, *Int. Archive of Photogrammetry and Remote Sensing*, Vol. 32, Part 4, GIS-Between Visions and Applications, Stuttgart, Germany, pp.170-175.

Fritz, L.W. 1996, Commercial Earth Observation Satellite, *Int. Archives of Photogrammetry and Remote Sensing*, Vol. XXXI Part. B4, pp.273-282.

Gonzalez, R.A. 1998, Horizontal Accuracy Assessment of the New Generation of High-resolution Satellite Imagery for Mapping Purposes, July 1998, M.S. Thesis, Graduate Program of Geodetic Science and Surveying, *The Ohio State University*.

Great Lakes Forecasting System (GLFS), http://superior.eng.ohio-state.edu/

Habib, A. and B. Beshah 1997, Modeling Panoramic Linear Array Scanner, Department of Civil and Environmental Engineering and Geodetic Science, *The Ohio State University*, Columbus, OH, Report No. 443.

Hansen, M. C. 1997, The History of Lake Erie, http://www.dnr.ohio.gov/odnr/geo_survey/lakeerie/lefact1.htm.

Herdendorf, C.E. and S.J. Bolsenga 1993, Lake Erie and Lake St. Clair Handbook, *Wayne State University Press*, Detroit, pp.11-91 and pp.355-380.

Hutchinson, M. F. 1996, A locally adaptive Approach to the Interpolation of Digital Elevation Models, *Proceeding on Third international Conference on integrating GIS and environomental Modeling*, Santa Barbara, CA, http://www. ncgia.ucsb.edu /conf/santa_fe_ cd-rom/sf_papers /hutchinson_michael_dem/local.htm.

Ingham, A. E. 1992, Hydrography for the Surveyors and Engineer, *Blackwell Scientific Publications*, London, 132p.

Kornus, W. 1996, MOMS-2P Geometric Calibration Report (Version 1.1) - Results of laboratory calibration, *DLR, Institute of Optoelectron-ics*.

Kornus, W. 1997, MOMS-2P Geometric Calibration Report (Version 1.3) - Results of channel 5A/5B registration, *Institute of Opto-electronics*, DLR.

Kornus, W. and M. Lehner 1998, Photogrammetric point determination and DEM Generation Using MOMS-2P/PRIRODA three-line Imagery, *International Archives of Photogrammetry and Remote Sensing*, Vol. 32, Part 4, Stuttgart, Germany, pp.321-328.

Lapine, L.A. 1991, Analytical Calibration of the Airborne Photogrammetric System Using A Priori Knowledge of the Exposure Station Obtained by Kinematic GPS Techniques, Report No. 411, 1991, Department of Geodetic Science and Surveying, *The Ohio State University*.

Li, R. 1995, Institutional Strengthening for Shoreline Management, Second report by the GIS Specialist, *AGRA Earth & Environmental Limited*, Calgary, Alberta.

Li, R. 1996, Institutional Strengthening for Shoreline Management, Third report by the GIS Specialist, *AGRA Earth & Environmental Limited*, Calgary, Alberta.

Li, R. 1998, Potential of High-Resolution Satellite Imagery for National Mapping Products, *PE&RS*, Vol.64, No.12, pp.1165-1170.

Liu, L.-K. 1998, Developing Geographic Information System Applications in Analysis of Responses to Lake ERIE Shoreline Changes, M.S. Thesis, Graduate Program of Geodetic Science and Surveying, *The Ohio State University*.

Mackey, S.D. and D.E. Jr. Guy 1994, Comparison of Long- And Short-term Recession Rate Along Ohio's Central Basin Shore of Lake Erie, 2^{ND} *Annual Lake Erie Coastal Erosion Study Workshop*, USGS.

Maslen, J., J. Peltenburg and S. Atkins 1996, Focusing in on the Firths: Can GIS fulfil its potential for Coastal Zone Management? *ESRI'96 (European) User Conference Proceedings*, ESRI, Http://www.esri.com/base/common/userconf/eruoproc96/toplevl/title1.htm.

Merchant, D.C. 1994, Airborne GPS-Photogrammetry for Transportation System, *Proceedings of ASPRS/ACSM 1994*.

Ohio Geologic Survey 1993, The Lake Erie Coastal Erosion Problem in Ohio, http://www.dnr.ohio. gov/odnr/geo_survey/lakeerie/.

Ohio Coastal Management Program 1997, Coastal Erosion Area Management, ODNR, http://www. dnr.state.oh.us/odnr/relm/coastal/erosion.htm.

Parker, J. 1997, The Advantages of In-Track Stereo Acquisition from High-Resolution Earth Resources Satellites. *Proceedings of ACSM/ASPRS Annual convention & Exposition*, Seattle, WA, Vol.3, pp.276-282.

Pincus, H.J. 1960, Engineering Geology of the Ohio Shore Line of Lake Erie, Maps, *Ohio Department of Natural Resource*, Columbus, Ohio.

Platt, C.V. 1998, Land-Eating Lake, Erosion Along Lake Erie, Timeline, January – February 1998, *Ohio Historical Society*, pp.42-53.

Seige P., P. Reinartz and M. Schroeder 1998, The MOMS-2P Mission on the MIR station, *Int. Archives of Photogrammetry and Remote Sensing*, Vol.32, Part 1, Bangalore, India.

Shaw, B. and J.R. Allen 1995, Analysis of a Dynamic Shoreline at Sandy Hook, New Jersey Using a Geographic Information System, *Proceedings of ASPRS/ACSM*, pp.382-391.

Slama, C., C. Theurer and S.W. Henriksen 1980, Manual of Photogrammetry, *American Society of Photogrammetry*, Falls Church, Va.

Trenhaile, A.S. 1997, Coastal Dynamics and Landforms, *Clarendon Press*, Oxford, pp.13-86.

US Army Corps of Engineers 1993, Great Lakes Erosion Fact Sheet, Great Lakes Hydraulics and Hydrology Branch, http://sparky.nce.usace.army.mil/hes/erosfact.html; Low Cost Shore Protection, http://sparky.nce.usace.army.mil/shore.protection /lcshmpg.html.

Wewel, F. 1996, Determination of Conjugate Points of Stereoscopic Three Line Scanner Data of Mars'96 Mission, *International Archives of Photogrammetry and Remote Sensing*. Vol.XXXI, Part B3. Vienna, PP.936-939.

Wu, J. 1986, Geometrische Analyse fuer Bilddaten stereoskopischer Dreifach-Linearzeilenabtaster, Wiss. Arbeiten der Fachrichtung Vermessungswesen der *Univ. Hannover*, Heft Nr. 146.

Attachment I. Partial Derivatives of Observation Equations

I.a Collinearity equations of GCPs for the aft-looking strip are

$$x_R^7 = z_R^7 \frac{r_{11}(X_G - X_S(t)) + r_{12}(Y_G - Y_S(t)) + r_{13}(Z_G - Z_S(t))}{r_{31}(X_G - X_S(t)) + r_{32}(Y_G - Y_S(t)) + r_{33}(Z_G - Z_S(t))} = z_R^7 \frac{\overline{X}}{\overline{Z}}$$

$$y_R^7 = z_R^7 \frac{r_{21}(X_G - X_S(t)) + r_{22}(Y_G - Y_S(t)) + r_{23}(Z_G - Z_S(t))}{r_{31}(X_G - X_S(t)) + r_{32}(Y_G - Y_S(t)) + r_{33}(Z_G - Z_S(t))} = z_R^7 \frac{\overline{Y}}{\overline{Z}}$$

where

$$\overline{X} = r_{11}(X_G - X_S(t)) + r_{12}(Y_G - Y_S(t)) + r_{13}(Z_G - Z_S(t))$$
$$\overline{Y} = r_{21}(X_G - X_S(t)) + r_{22}(Y_G - Y_S(t)) + r_{23}(Z_G - Z_S(t))$$
$$\overline{Z} = r_{31}(X_G - X_S(t)) + r_{32}(Y_G - Y_S(t)) + r_{33}(Z_G - Z_S(t))$$

Partial differentials of (x_R^7, y_R^7) with respect to $(X_s(t), Y_s(t), Z_s(t))$ and $(\omega_s(t), \phi_s(t), \kappa_s(t))$ are

$$\frac{\partial x_R^7}{\partial X_S(t)} dX_S(t) = \frac{\partial x_R^7}{\partial X_S(t)} (da_0 + tda_1 + t^2 da_2 + t^3 da_3)$$
$$\frac{\partial x_R^7}{\partial Y_S(t)} dY_S(t) = \frac{\partial x_R^7}{\partial Y_S(t)} (db_0 + tdb_1 + t^2 db_2 + t^3 db_3)$$
$$\frac{\partial x_R^7}{\partial Z_S(t)} dZ_S(t) = \frac{\partial x_R^7}{\partial Z_S(t)} (dc_0 + tdc_1 + t^2 dc_2 + t^3 dc_3)$$
$$\frac{\partial x_R^7}{\partial \varphi_S(t)} d\varphi_S(t) = \frac{\partial x_R^7}{\partial \varphi_S(t)} (dd_0 + tdd_1 + t^2 dd_2 + t^3 dd_3)$$
$$\frac{\partial x_R^7}{\partial \omega_S(t)} d\omega_S(t) = \frac{\partial x_R^7}{\partial \omega_S(t)} (de_0 + tde_1 + t^2 de_2 + t^3 de_3)$$
$$\frac{\partial x_R^7}{\partial k_S(t)} dk_S(t) = \frac{\partial x_R^7}{\partial k_S(t)} (df_0 + tdf_1 + t^2 df_2 + t^3 df_3)$$
$$\frac{\partial y_R^7}{\partial X_S(t)} dX_S(t) = \frac{\partial y_R^7}{\partial X_S(t)} (da_0 + tda_1 + t^2 da_2 + t^3 da_3)$$
$$\frac{\partial y_R^7}{\partial Y_S(t)} dY_S(t) = \frac{\partial y_R^7}{\partial Y_S(t)} (db_0 + tdb_1 + t^2 db_2 + t^3 db_3)$$
$$\frac{\partial y_R^7}{\partial Z_S(t)} dZ_S(t) = \frac{\partial y_R^7}{\partial Z_S(t)} (dc_0 + tdc_1 + t^2 dc_2 + t^3 dc_3)$$
$$\frac{\partial y_R^7}{\partial \varphi_S(t)} d\varphi_S(t) = \frac{\partial y_R^7}{\partial \varphi_S(t)} (dd_0 + tdd_1 + t^2 dd_2 + t^3 dd_3)$$
$$\frac{\partial y_R^7}{\partial \omega_S(t)} d\omega_S(t) = \frac{\partial y_R^7}{\partial \omega_S(t)} (de_0 + tde_1 + t^2 de_2 + t^3 de_3)$$
$$\frac{\partial y_R^7}{\partial k_S(t)} dk_S(t) = \frac{\partial y_R^7}{\partial k_S(t)} (df_0 + tdf_1 + t^2 df_2 + t^3 df_3)$$

The partial derivatives are the following:

$$\frac{\partial x_R^7}{\partial X_S(t)} = z_R^7 \frac{\frac{\partial \overline{X}}{\partial X_S(t)}\overline{Z} - \frac{\partial \overline{Z}}{\partial X_S(t)}\overline{X}}{\overline{Z}\overline{Z}} = z_R^7 \frac{-r_{11}\overline{Z} + r_{31}\overline{X}}{\overline{Z}\overline{Z}} = \frac{1}{\overline{Z}}(-z_R^7 r_{11} + r_{31} x_R^7) \qquad \text{(unit: mm/m)}$$

$$\frac{\partial x_R^7}{\partial Y_S(t)} = z_R^7 \frac{\frac{\partial \overline{X}}{\partial Y_S(t)}\overline{Z} - \frac{\partial \overline{Z}}{\partial Y_S(t)}\overline{X}}{\overline{Z}\overline{Z}} = z_R^7 \frac{-r_{12}\overline{Z} + r_{32}\overline{X}}{\overline{Z}\overline{Z}} = \frac{1}{\overline{Z}}(-z_R^7 r_{12} + r_{32} x_R^7)$$

$$\frac{\partial x_R^7}{\partial Z_S(t)} = z_R^7 \frac{\frac{\partial \overline{X}}{\partial Z_S(t)}\overline{Z} - \frac{\partial \overline{Z}}{\partial Z_S(t)}\overline{X}}{\overline{Z}\overline{Z}} = z_R^7 \frac{-r_{13}\overline{Z} + r_{33}\overline{X}}{\overline{Z}\overline{Z}} = \frac{1}{\overline{Z}}(-z_R^7 r_{13} + r_{33} x_R^7)$$

$$\frac{\partial x_R^7}{\partial \varphi_S(t)} = z_R^7 \frac{\frac{\partial \overline{X}}{\partial \varphi_S(t)}\overline{Z} - \frac{\partial \overline{Z}}{\partial \varphi_S(t)}\overline{X}}{\overline{Z}\overline{Z}} = \frac{z_R^7}{\overline{Z}\overline{Z}}\{\overline{Z}[\frac{\partial r_{11}}{\partial \varphi_S(t)}(X_G - X_S) + \frac{\partial r_{12}}{\partial \varphi_S(t)}(Y_G - Y_S) + \frac{\partial r_{13}}{\partial \varphi_S(t)}(Z_G - Z_S)] -$$

$$\overline{X}[\frac{\partial r_{31}}{\partial \varphi_S(t)}(X_G - X_S) + \frac{\partial r_{32}}{\partial \varphi_S(t)}(Y_G - Y_S) + \frac{\partial r_{33}}{\partial \varphi_S(t)}(Z_G - Z_S)]\}$$

$$= \frac{z_R^7}{\overline{Z}\overline{Z}}\{\overline{Z}[-\sin\varphi\cos k(X_G - X_S) + \sin\omega\cos\varphi\cos k(Y_G - Y_S) - \cos\omega\cos\varphi\cos k(Z_G - Z_S)] -$$

$$\overline{X}[\cos\varphi(X_G - X_S) + \sin\omega\sin\varphi(Y_G - Y_S) - \cos\omega\sin\varphi(Z_G - Z_S)]\}$$

$$= \frac{z_R^7}{\overline{Z}\overline{Z}}\{\overline{Z}[-\sin\varphi\cos k(X_G - X_S) + r_{11}\sin\omega(Y_G - Y_S) - r_{33}\cos k(Z_G - Z_S)] -$$

$$\overline{X}[\cos\varphi(X_G - X_S) + \sin\omega\sin\varphi(Y_G - Y_S) - \cos\omega\sin\varphi(Z_G - Z_S)]\}$$

$$\frac{\partial x_R^7}{\partial \omega_S(t)} = z_R^7 \frac{\frac{\partial \overline{X}}{\partial \omega_S(t)}\overline{Z} - \frac{\partial \overline{Z}}{\partial \omega_S(t)}\overline{X}}{\overline{Z}\overline{Z}} = \frac{z_R^7}{\overline{Z}\overline{Z}}\{\overline{Z}[\frac{\partial r_{11}}{\partial \omega_S(t)}(X_G - X_S) + \frac{\partial r_{12}}{\partial \omega_S(t)}(Y_G - Y_S) + \frac{\partial r_{13}}{\partial \omega_S(t)}(Z_G - Z_S)] -$$

$$\overline{X}[\frac{\partial r_{31}}{\partial \omega_S(t)}(X_G - X_S) + \frac{\partial r_{32}}{\partial \omega_S(t)}(Y_G - Y_S) + \frac{\partial r_{33}}{\partial \omega_S(t)}(Z_G - Z_S)]\}$$

$$= \frac{z_R^7}{\overline{Z}\overline{Z}}\{\overline{Z}[0\cdot(X_G - X_S) + (-\sin\omega\sin k + \cos\omega\sin\varphi\cos k)(Y_G - Y_S) + (\cos\omega\sin k + \sin\omega\sin\varphi\cos k(Z_G - Z_S)] -$$

$$\overline{X}[0\cdot(X_G - X_S) - \cos\omega\cos\varphi(Y_G - Y_S) - \sin\omega\cos\varphi(Z_G - Z_S)]\}$$

$$= \frac{z_R^7}{\overline{Z}\overline{Z}}\{\overline{Z}[-r_{13}(Y_G - Y_S) + r_{12}(Z_G - Z_S)] - \overline{X}[-r_{33}(Y_G - Y_S) + r_{32}(Z_G - Z_S)]\}$$

$$\frac{\partial x_R^7}{\partial k_S(t)} = z_R^7 \frac{\frac{\partial \overline{X}}{\partial k_S(t)}\overline{Z} - \frac{\partial \overline{Z}}{\partial k_S(t)}\overline{X}}{\overline{Z}\overline{Z}} = \frac{z_R^7}{\overline{Z}\overline{Z}}\{\overline{Z}[-\cos\varphi\sin k(X_G - X_S) + (\cos\omega\cos k - \sin\omega\sin\varphi\sin k)$$

$$(Y_G - Y_S) + (\sin\omega\cos k + \cos\omega\sin\varphi\sin k)(Z_G - Z_S)] - \overline{X}[0\cdot(X_G - X_S) + 0\cdot(Y_G - Y_S) + 0\cdot(Z_G - Z_S)]\}$$

$$= \frac{z_R^7}{\overline{Z}\overline{Z}}\{\overline{Z}[r_{21}(X_G - X_S) + r_{22}(Y_G - Y_S) + r_{23}(Z_G - Z_S)]\}$$

$$= \frac{z_R^7}{\overline{Z}}(\overline{Y}) = y_R^7$$

$$\frac{\partial y_R^7}{\partial X_S(t)} = z_R^7 \frac{\frac{\partial \overline{Y}}{\partial X_S(t)}\overline{Z} - \frac{\partial \overline{Z}}{\partial X_S(t)}\overline{Y}}{\overline{Z}\overline{Z}} = z_R^7 \frac{-r_{21}\overline{Z} + r_{31}\overline{Y}}{\overline{Z}\overline{Z}} = \frac{1}{\overline{Z}}(-z_R^7 r_{21} + r_{31} y_R^7)$$

$$\frac{\partial y_R^7}{\partial Y_S(t)} = z_R^7 \frac{\frac{\partial \overline{Y}}{\partial Y_S(t)}\overline{Z} - \frac{\partial \overline{Z}}{\partial Y_S(t)}\overline{Y}}{\overline{Z}\overline{Z}} = z_R^7 \frac{-r_{22}\overline{Z} + r_{32}\overline{Y}}{\overline{Z}\overline{Z}} = \frac{1}{\overline{Z}}(-z_R^7 r_{22} + r_{32} y_R^7)$$

$$\frac{\partial y_R^7}{\partial Z_S(t)} = z_R^7 \frac{\frac{\partial \overline{Y}}{\partial Z_S(t)}\overline{Z} - \frac{\partial \overline{Z}}{\partial Z_S(t)}\overline{Y}}{\overline{Z}\overline{Z}} = z_R^7 \frac{-r_{23}\overline{Z} + r_{33}\overline{X}}{\overline{Z}\overline{Z}} = \frac{1}{\overline{Z}}(-z_R^7 r_{23} + r_{33} y_R^7)$$

$$\frac{\partial y_R^7}{\partial \varphi_S(t)} = z_R^7 \frac{\frac{\partial \overline{Y}}{\partial \varphi_S(t)}\overline{Z} - \frac{\partial \overline{Z}}{\partial \varphi_S(t)}\overline{Y}}{\overline{Z}\overline{Z}} = \frac{z_R^7}{\overline{Z}\overline{Z}}\{\overline{Z}[\frac{\partial r_{21}}{\partial \varphi_S(t)}(X_G - X_S) + \frac{\partial r_{22}}{\partial \varphi_S(t)}(Y_G - Y_S) + \frac{\partial r_{23}}{\partial \varphi_S(t)}(Z_G - Z_S)] -$$

$$\overline{Y}[\frac{\partial r_{31}}{\partial \varphi_S(t)}(X_G - X_S) + \frac{\partial r_{32}}{\partial \varphi_S(t)}(Y_G - Y_S) + \frac{\partial r_{33}}{\partial \varphi_S(t)}(Z_G - Z_S)]\}$$

$$= \frac{z_R^7}{\overline{Z}\overline{Z}}\{\overline{Z}[\sin\varphi\sin k(X_G - X_S) - \sin\omega\cos\varphi\sin k(Y_G - Y_S) + \cos\omega\cos\varphi\sin k(Z_G - Z_S)] -$$

$$\overline{Y}[\cos\varphi(X_G - X_S) + \sin\omega\sin\varphi(Y_G - Y_S) - \cos\omega\sin\varphi(Z_G - Z_S)]\}$$

$$= \frac{z_R^7}{\overline{Z}\overline{Z}}\{\overline{Z}[\sin\varphi\sin k(X_G - X_S) + r_{21}\sin\omega(Y_G - Y_S) + r_{33}\sin k(Z_G - Z_S)] -$$

$$\overline{Y}[\cos\varphi(X_G - X_S) + \sin\omega\sin\varphi(Y_G - Y_S) - \cos\omega\sin\varphi(Z_G - Z_S)]\}$$

$$\frac{\partial y_R^7}{\partial \omega_S(t)} = z_R^7 \frac{\frac{\partial \overline{Y}}{\partial \omega_S(t)}\overline{Z} - \frac{\partial \overline{Z}}{\partial \omega_S(t)}\overline{Y}}{\overline{Z}\overline{Z}} = \frac{z_R^7}{\overline{Z}\overline{Z}}\{\overline{Z}[\frac{\partial r_{21}}{\partial \omega_S(t)}\cdot(X_G - X_S) + \frac{\partial r_{22}}{\partial \omega_S(t)}(Y_G - Y_S) + \frac{\partial r_{23}}{\partial \omega_S(t)}(Z_G - Z_S)] -$$

$$\overline{Y}[\frac{\partial r_{31}}{\partial \varphi_S(t)}(X_G - X_S) + \frac{\partial r_{32}}{\partial \varphi_S(t)}(Y_G - Y_S) + \frac{\partial r_{33}}{\partial \varphi_S(t)}(Z_G - Z_S)]\}$$

$$= \frac{z_R^7}{\overline{Z}\overline{Z}}\{\overline{Z}[0\cdot(X_G - X_S) + (-\sin\omega\cos k - \cos\omega\sin\varphi\sin k)(Y_G - Y_S) + (\cos\omega\cos k - \sin\omega\sin\varphi\sin k)(Z_G - Z_S)] -$$

$$\overline{Y}[0\cdot(X_G - X_S) - \cos\omega\cos\varphi(Y_G - Y_S) - \sin\omega\cos\varphi(Z_G - Z_S)]\}$$

$$= \frac{z_R^7}{\overline{Z}\overline{Z}}\{\overline{Z}[-r_{23}(Y_G - Y_S) + r_{22}(Z_G - Z_S)] - \overline{Y}[-r_{33}(Y_G - Y_S) + r_{32}(Z_G - Z_S)]\}$$

$$\frac{\partial y_R^7}{\partial k_S(t)} = z_R^7 \frac{\frac{\partial \overline{Y}}{\partial k_S(t)}\overline{Z} - \frac{\partial \overline{Z}}{\partial k_S(t)}\overline{Y}}{\overline{Z}\overline{Z}} = \frac{z_R^7}{\overline{Z}\overline{Z}}\{\overline{Z}[-\cos\varphi\cos k(X_G - X_S) + (-\cos\omega\sin k - \sin\omega\sin\varphi\cos k)$$

$$(Y_G - Y_S) + (-\sin\omega\sin k + \cos\omega\sin\varphi\cos k)(Z_G - Z_S)] - \overline{Y}[0\cdot(X_G - X_S) + 0\cdot(Y_G - Y_S) + 0\cdot(Z_G - Z_S)]\}$$

$$= \frac{z_R^7}{\overline{Z}\overline{Z}}\{\overline{Z}[-r_{11}(X_G - X_S) - r_{12}(Y_G - Y_S) - r_{13}(Z_G - Z_S)]\}$$

$$= \frac{z_R^7}{\overline{Z}}(-\overline{X}) = -x_R^7$$

Finally, the coefficients of observation equations are

$$\beta_{11} = \frac{\partial x_R^7}{\partial X_S(t)},\ \beta_{12} = \frac{\partial x_R^7}{\partial Y_S(t)},\ \beta_{13} = \frac{\partial x_R^7}{\partial Z_S(t)},\ \beta_{14} = \frac{\partial x_R^7}{\partial \varphi_S(t)},\ \beta_{15} = \frac{\partial x_R^7}{\partial \omega_S(t)},\ \beta_{16} = \frac{\partial x_R^7}{\partial k_S(t)},\ \beta_{17} = t\cdot\beta_{11}$$

$$\beta_{18} = t\cdot\beta_{12},\ \beta_{19} = t\cdot\beta_{13}$$

$$\beta_{110} = t\cdot\beta_{14},\ \beta_{111} = t\cdot\beta_{15},\ \beta_{112} = t\cdot\beta_{16},\ \beta_{113} = t^2\cdot\beta_{11},\ \beta_{114} = t^2\cdot\beta_{12},\ \beta_{115} = t^2\cdot\beta_{13},\ \beta_{116} = t^2\cdot\beta_{14}$$

$$\beta_{117} = t^2\cdot\beta_{15},\ \beta_{118} = t^2\cdot\beta_{16},\ \beta_{119} = t^3\cdot\beta_{11},\ \beta_{120} = t^3\cdot\beta_{12},\ \beta_{121} = t^3\cdot\beta_{13},\ \beta_{122} = t^3\cdot\beta_{14},\ \beta_{123} = t^3\cdot\beta_{15}$$

$$\beta_{124} = t^3\cdot\beta_{16}$$

$$\beta_{21} = \frac{\partial y_R^7}{\partial X_S(t)},\ \beta_{22} = \frac{\partial y_R^7}{\partial Y_S(t)},\ \beta_{23} = \frac{\partial y_R^7}{\partial Z_S(t)},\ \beta_{24} = \frac{\partial y_R^7}{\partial \varphi_S(t)},\ \beta_{25} = \frac{\partial y_R^7}{\partial \omega_S(t)},\ \beta_{26} = \frac{\partial y_R^7}{\partial k_S(t)},\ \beta_{27} = t\cdot\beta_{21}$$

$$\beta_{28} = t\cdot\beta_{22},\ \beta_{29} = t\cdot\beta_{23}$$

$$\beta_{210} = t\cdot\beta_{24},\ \beta_{211} = t\cdot\beta_{25},\ \beta_{212} = t\cdot\beta_{26},\ \beta_{213} = t^2\cdot\beta_{21},\ \beta_{214} = t^2\cdot\beta_{22},\ \beta_{215} = t^2\cdot\beta_{23},\ \beta_{216} = t^2\cdot\beta_{24}$$

$$\beta_{217} = t^2\cdot\beta_{25},\ \beta_{218} = t^2\cdot\beta_{26},\ \beta_{219} = t^3\cdot\beta_{21},\ \beta_{220} = t^3\cdot\beta_{22},\ \beta_{221} = t^3\cdot\beta_{23},\ \beta_{222} = t^3\cdot\beta_{24},\ \beta_{223} = t^3\cdot\beta_{25}$$

$$\beta_{224} = t^3\cdot\beta_{26}$$

I.b Collinearity equations of unknown ground points for the aft-looking strip are

$$x_M^7 = z_R^7 \frac{r_{11}(X_M - X_S(t)) + r_{12}(Y_M - Y_S(t)) + r_{13}(Z_M - Z_S(t))}{r_{31}(X_M - X_S(t)) + r_{32}(Y_M - Y_S(t)) + r_{33}(Z_M - Z_S(t))} = z_R^7 \frac{\overline{X}}{\overline{Z}}$$

$$y_M^7 = z_R^7 \frac{r_{21}(X_M - X_S(t)) + r_{22}(Y_M - Y_S(t)) + r_{23}(Z_M - Z_S(t))}{r_{31}(X_M - X_S(t)) + r_{32}(Y_M - Y_S(t)) + r_{33}(Z_M - Z_S(t))} = z_R^7 \frac{\overline{Y}}{\overline{Z}}$$

where

$$\overline{X} = r_{11}(X_M - X_S(t)) + r_{12}(Y_M - Y_S(t)) + r_{13}(Z_M - Z_S(t))$$
$$\overline{Y} = r_{21}(X_M - X_S(t)) + r_{22}(Y_M - Y_S(t)) + r_{23}(Z_M - Z_S(t))$$
$$\overline{Z} = r_{31}(X_M - X_S(t)) + r_{32}(Y_M - Y_S(t)) + r_{33}(Z_M - Z_S(t))$$

Partial differentials of (x_R^7, y_R^7) with respect to ($X_s(t)$, $Y_s(t)$, $Z_s(t)$) and ($\omega_s(t)$, $\phi_s(t)$, $\kappa_s(t)$) are

$$\frac{\partial x_M^7}{\partial X_S(t)} dX_S(t) = \frac{\partial x_M^7}{\partial X_S(t)} (da_0 + tda_1 + t^2 da_2 + t^3 da_3)$$
$$\frac{\partial x_M^7}{\partial Y_S(t)} dY_S(t) = \frac{\partial x_M^7}{\partial Y_S(t)} (db_0 + tdb_1 + t^2 db_2 + t^3 db_3)$$
$$\frac{\partial x_M^7}{\partial Z_S(t)} dZ_S(t) = \frac{\partial x_M^7}{\partial Z_S(t)} (dc_0 + tdc_1 + t^2 dc_2 + t^3 dc_3)$$
$$\frac{\partial x_M^7}{\partial \varphi_S(t)} d\varphi_S(t) = \frac{\partial x_M^7}{\partial \varphi_S(t)} (dd_0 + tdd_1 + t^2 dd_2 + t^3 dd_3)$$
$$\frac{\partial x_M^7}{\partial \omega_S(t)} d\omega_S(t) = \frac{\partial x_M^7}{\partial \omega_S(t)} (de_0 + tde_1 + t^2 de_2 + t^3 de_3)$$
$$\frac{\partial x_M^7}{\partial k_S(t)} dk_S(t) = \frac{\partial x_M^7}{\partial k_S(t)} (df_0 + tdf_1 + t^2 df_2 + t^3 df_3)$$
$$\frac{\partial y_M^7}{\partial X_S(t)} dX_S(t) = \frac{\partial y_M^7}{\partial X_S(t)} (da_0 + tda_1 + t^2 da_2 + t^3 da_3)$$
$$\frac{\partial y_M^7}{\partial Y_S(t)} dY_S(t) = \frac{\partial y_M^7}{\partial Y_S(t)} (db_0 + tdb_1 + t^2 db_2 + t^3 db_3)$$
$$\frac{\partial y_M^7}{\partial Z_S(t)} dZ_S(t) = \frac{\partial y_M^7}{\partial Z_S(t)} (dc_0 + tdc_1 + t^2 dc_2 + t^3 dc_3)$$
$$\frac{\partial y_M^7}{\partial \varphi_S(t)} d\varphi_S(t) = \frac{\partial y_M^7}{\partial \varphi_S(t)} (dd_0 + tdd_1 + t^2 dd_2 + t^3 dd_3)$$
$$\frac{\partial y_M^7}{\partial \omega_S(t)} d\omega_S(t) = \frac{\partial y_M^7}{\partial \omega_S(t)} (de_0 + tde_1 + t^2 de_2 + t^3 de_3)$$
$$\frac{\partial y_M^7}{\partial k_S(t)} dk_S(t) = \frac{\partial y_M^7}{\partial k_S(t)} (df_0 + tdf_1 + t^2 df_2 + t^3 df_3)$$

The partial derivatives are the following:

$$\frac{\partial x_M^7}{\partial X_S(t)} = z_R^7 \frac{\frac{\partial \overline{X}}{\partial X_S(t)} \overline{Z} - \frac{\partial \overline{Z}}{\partial X_S(t)} \overline{X}}{\overline{Z}\overline{Z}} = z_R^7 \frac{-r_{11}\overline{Z} + r_{31}\overline{X}}{\overline{Z}\overline{Z}} = \frac{1}{\overline{Z}}(-z_R^7 r_{11} + r_{31} x_M^7) \qquad \text{(unit: mm/m)}$$

$$\frac{\partial x_M^7}{\partial Y_S(t)} = z_R^7 \frac{\frac{\partial \overline{X}}{\partial Y_S(t)}\overline{Z} - \frac{\partial \overline{Z}}{\partial Y_S(t)}\overline{X}}{\overline{Z}\overline{Z}} = z_R^7 \frac{-r_{12}\overline{Z} + r_{32}\overline{X}}{\overline{Z}\overline{Z}} = \frac{1}{\overline{Z}}(-z_R^7 r_{12} + r_{32} x_M^7)$$

$$\frac{\partial x_M^7}{\partial Z_S(t)} = z_R^7 \frac{\frac{\partial \overline{X}}{\partial Z_S(t)}\overline{Z} - \frac{\partial \overline{Z}}{\partial Z_S(t)}\overline{X}}{\overline{Z}\overline{Z}} = z_R^7 \frac{-r_{13}\overline{Z} + r_{33}\overline{X}}{\overline{Z}\overline{Z}} = \frac{1}{\overline{Z}}(-z_R^7 r_{13} + r_{33} x_M^7)$$

$$\frac{\partial x_M^7}{\partial \varphi_S(t)} = z_R^7 \frac{\frac{\partial \overline{X}}{\partial \varphi_S(t)}\overline{Z} - \frac{\partial \overline{Z}}{\partial \varphi_S(t)}\overline{X}}{\overline{Z}\overline{Z}} = \frac{z_R^7}{\overline{Z}\overline{Z}}\{\overline{Z}[\frac{\partial r_{11}}{\partial \varphi_S(t)}(X_M - X_S) + \frac{\partial r_{12}}{\partial \varphi_S(t)}(Y_M - Y_S) + \frac{\partial r_{13}}{\partial \varphi_S(t)}(Z_M - Z_S)] -$$

$$\overline{X}[\frac{\partial r_{31}}{\partial \varphi_S(t)}(X_M - X_S) + \frac{\partial r_{32}}{\partial \varphi_S(t)}(Y_M - Y_S) + \frac{\partial r_{33}}{\partial \varphi_S(t)}(Z_M - Z_S)]\}$$

$$= \frac{z_R^7}{\overline{Z}\overline{Z}}\{\overline{Z}[-\sin\varphi\cos k(X_M - X_S) + \sin\omega\cos\varphi\cos k(Y_M - Y_S) - \cos\omega\cos\varphi\cos k(Z_M - Z_S)] -$$

$$\overline{X}[\cos\varphi(X_M - X_S) + \sin\omega\sin\varphi(Y_M - Y_S) - \cos\omega\sin\varphi(Z_M - Z_S)]\}$$

$$= \frac{z_R^7}{\overline{Z}\overline{Z}}\{\overline{Z}[-\sin\varphi\cos k(X_M - X_S) + r_{11}\sin\omega(Y_M - Y_S) - r_{33}\cos k(Z_M - Z_S)] -$$

$$\overline{X}[\cos\varphi(X_M - X_S) + \sin\omega\sin\varphi(Y_M - Y_S) - \cos\omega\sin\varphi(Z_M - Z_S)]\}$$

$$\frac{\partial x_M^7}{\partial \omega_S(t)} = z_R^7 \frac{\frac{\partial \overline{X}}{\partial \omega_S(t)}\overline{Z} - \frac{\partial \overline{Z}}{\partial \omega_S(t)}\overline{X}}{\overline{Z}\overline{Z}} = \frac{z_R^7}{\overline{Z}\overline{Z}}\{\overline{Z}[\frac{\partial r_{11}}{\partial \omega_S(t)}(X_M - X_S) + \frac{\partial r_{12}}{\partial \omega_S(t)}(Y_M - Y_S) + \frac{\partial r_{13}}{\partial \omega_S(t)}(Z_M - Z_S)] -$$

$$\overline{X}[\frac{\partial r_{31}}{\partial \omega_S(t)}(X_M - X_S) + \frac{\partial r_{32}}{\partial \omega_S(t)}(Y_M - Y_S) + \frac{\partial r_{33}}{\partial \omega_S(t)}(Z_M - Z_S)]\}$$

$$= \frac{z_R^7}{\overline{Z}\overline{Z}}\{\overline{Z}[0\cdot(X_M - X_S) + (-\sin\omega\sin k + \cos\omega\sin\varphi\cos k)(Y_M - Y_S) + (\cos\omega\sin k + \sin\omega\sin\varphi\cos k(Z_M - Z_S)] -$$

$$\overline{X}[0\cdot(X_M - X_S) - \cos\omega\cos\varphi(Y_M - Y_S) - \sin\omega\cos\varphi(Z_M - Z_S)]\}$$

$$= \frac{z_R^7}{\overline{Z}\overline{Z}}\{\overline{Z}[-r_{13}(Y_M - Y_S) + r_{12}(Z_M - Z_S)] - \overline{X}[-r_{33}(Y_M - Y_S) + r_{32}(Z_M - Z_S)]\}$$

$$\frac{\partial x_M^7}{\partial k_S(t)} = z_R^7 \frac{\frac{\partial \overline{X}}{\partial k_S(t)}\overline{Z} - \frac{\partial \overline{Z}}{\partial k_S(t)}\overline{X}}{\overline{Z}\overline{Z}} = \frac{z_R^7}{\overline{Z}\overline{Z}}\{\overline{Z}[-\cos\varphi\sin k(X_M - X_S) + (\cos\omega\cos k - \sin\omega\sin\varphi\sin k)$$

$$(Y_M - Y_S) + (\sin\omega\cos k + \cos\omega\sin\varphi\sin k)(Z_M - Z_S)] - \overline{X}[0\cdot(X_M - X_S) + 0\cdot(Y_M - Y_S) + 0\cdot(Z_M - Z_S)]\}$$

$$= \frac{z_R^7}{\overline{Z}\overline{Z}}\{\overline{Z}[r_{21}(X_M - X_S) + r_{22}(Y_M - Y_S) + r_{23}(Z_M - Z_S)]\}$$

$$= \frac{z_R^7}{\overline{Z}}(\overline{Y}) = y_M^7$$

$$\frac{\partial y_M^7}{\partial X_S(t)} = z_R^7 \frac{\frac{\partial \overline{Y}}{\partial X_S(t)}\overline{Z} - \frac{\partial \overline{Z}}{\partial X_S(t)}\overline{Y}}{\overline{Z}\overline{Z}} = z_R^7 \frac{-r_{21}\overline{Z} + r_{31}\overline{Y}}{\overline{Z}\overline{Z}} = \frac{1}{\overline{Z}}(-z_R^7 r_{21} + r_{31} y_M^7)$$

$$\frac{\partial y_M^7}{\partial Y_S(t)} = z_R^7 \frac{\frac{\partial \overline{Y}}{\partial Y_S(t)}\overline{Z} - \frac{\partial \overline{Z}}{\partial Y_S(t)}\overline{Y}}{\overline{Z}\overline{Z}} = z_R^7 \frac{-r_{22}\overline{Z} + r_{32}\overline{Y}}{\overline{Z}\overline{Z}} = \frac{1}{\overline{Z}}(-z_R^7 r_{22} + r_{32} y_M^7)$$

$$\frac{\partial y_M^7}{\partial Z_S(t)} = z_R^7 \frac{\frac{\partial \overline{Y}}{\partial Z_S(t)}\overline{Z} - \frac{\partial \overline{Z}}{\partial Z_S(t)}\overline{Y}}{\overline{Z}\overline{Z}} = z_R^7 \frac{-r_{23}\overline{Z} + r_{33}\overline{X}}{\overline{Z}\overline{Z}} = \frac{1}{\overline{Z}}(-z_R^7 r_{23} + r_{33} y_M^7)$$

$$\frac{\partial y_M^7}{\partial \varphi_S(t)} = z_R^7 \frac{\frac{\partial \overline{Y}}{\partial \varphi_S(t)}\overline{Z} - \frac{\partial \overline{Z}}{\partial \varphi_S(t)}\overline{Y}}{\overline{Z}\overline{Z}} = \frac{z_R^7}{\overline{Z}\overline{Z}}\{\overline{Z}[\frac{\partial r_{21}}{\partial \varphi_S(t)}(X_M - X_S) + \frac{\partial r_{22}}{\partial \varphi_S(t)}(Y_M - Y_S) + \frac{\partial r_{23}}{\partial \varphi_S(t)}(Z_M - Z_S)] -$$

$$\overline{Y}[\frac{\partial r_{31}}{\partial \varphi_S(t)}(X_M - X_S) + \frac{\partial r_{32}}{\partial \varphi_S(t)}(Y_M - Y_S) + \frac{\partial r_{33}}{\partial \varphi_S(t)}(Z_M - Z_S)]\}$$

$$= \frac{z_R^7}{\overline{Z}\overline{Z}}\{\overline{Z}[\sin\varphi\sin k(X_M - X_S) - \sin\omega\cos\varphi\sin k(Y_M - Y_S) + \cos\omega\cos\varphi\sin k(Z_M - Z_S)] -$$

$$\overline{Y}[\cos\varphi(X_M - X_S) + \sin\omega\sin\varphi(Y_M - Y_S) - \cos\omega\sin\varphi(Z_M - Z_S)]\}$$

$$= \frac{z_R^7}{\overline{Z}\overline{Z}}\{\overline{Z}[\sin\varphi\sin k(X_M - X_S) + r_{21}\sin\omega(Y_M - Y_S) + r_{33}\sin k(Z_M - Z_S)] -$$

$$\overline{Y}[\cos\varphi(X_M - X_S) + \sin\omega\sin\varphi(Y_M - Y_S) - \cos\omega\sin\varphi(Z_M - Z_S)]\}$$

$$\frac{\partial y_M^7}{\partial \omega_S(t)} = z_R^7 \frac{\frac{\partial \overline{Y}}{\partial \omega_S(t)}\overline{Z} - \frac{\partial \overline{Z}}{\partial \omega_S(t)}\overline{Y}}{\overline{Z}\overline{Z}} = \frac{z_R^7}{\overline{Z}\overline{Z}}\{\overline{Z}[\frac{\partial r_{21}}{\partial \omega_S(t)}\cdot(X_M - X_S) + \frac{\partial r_{22}}{\partial \omega_S(t)}(Y_M - Y_S) + \frac{\partial r_{23}}{\partial \omega_S(t)}(Z_M - Z_S)] -$$

$$\overline{Y}[\frac{\partial r_{31}}{\partial \varphi_S(t)}(X_M - X_S) + \frac{\partial r_{32}}{\partial \varphi_S(t)}(Y_M - Y_S) + \frac{\partial r_{33}}{\partial \varphi_S(t)}(Z_M - Z_S)]\}$$

$$= \frac{z_R^7}{\overline{Z}\overline{Z}}\{\overline{Z}[0\cdot(X_M - X_S) + (-\sin\omega\cos k - \cos\omega\sin\varphi\sin k)(Y_M - Y_S) + (\cos\omega\cos k - \sin\omega\sin\varphi\sin k)(Z_M - Z_S)] -$$

$$\overline{Y}[0\cdot(X_M - X_S) - \cos\omega\cos\varphi(Y_M - Y_S) - \sin\omega\cos\varphi(Z_M - Z_S)]\}$$

$$= \frac{z_R^7}{\overline{Z}\overline{Z}}\{\overline{Z}[-r_{23}(Y_M - Y_S) + r_{22}(Z_M - Z_S)] - \overline{Y}[-r_{33}(Y_M - Y_S) + r_{32}(Z_M - Z_S)]\}$$

$$\frac{\partial y_M^7}{\partial k_S(t)} = z_R^7 \frac{\frac{\partial \overline{Y}}{\partial k_S(t)}\overline{Z} - \frac{\partial \overline{Z}}{\partial k_S(t)}\overline{Y}}{\overline{Z}\overline{Z}} = \frac{z_R^7}{\overline{Z}\overline{Z}}\{\overline{Z}[-\cos\varphi\cos k(X_M - X_S) + (-\cos\omega\sin k - \sin\omega\sin\varphi\cos k)$$

$$(Y_M - Y_S) + (-\sin\omega\sin k + \cos\omega\sin\varphi\cos k)(Z_M - Z_S)] - \overline{Y}[0\cdot(X_M - X_S) + 0\cdot(Y_M - Y_S) + 0\cdot(Z_M - Z_S)]\}$$

$$= \frac{z_R^7}{\overline{Z}\overline{Z}}\{\overline{Z}[-r_{11}(X_M - X_S) - r_{12}(Y_M - Y_S) - r_{13}(Z_M - Z_S)]\}$$

$$= \frac{z_R^7}{\overline{Z}}(-\overline{X}) = -x_M^7$$

Finally, the coefficients of observation equations are

$$\gamma_{11}=\frac{\partial x_M^7}{\partial X_S(t)},\ \gamma_{12}=\frac{\partial x_M^7}{\partial Y_S(t)},\ \gamma_{13}=\frac{\partial x_M^7}{\partial Z_S(t)},\ \gamma_{14}=\frac{\partial x_M^7}{\partial \varphi_S(t)},\ \gamma_{15}=\frac{\partial x_M^7}{\partial \omega_S(t)},\ \gamma_{16}=\frac{\partial x_M^7}{\partial k_S(t)},\ \gamma_{17}=t\cdot\gamma_{11}$$

$$\gamma_{18}=t\cdot\gamma_{12},\ \gamma_{19}=t\cdot\gamma_{13}$$

$$\gamma_{110}=t\cdot\gamma_{14},\ \gamma_{111}=t\cdot\gamma_{15},\ \gamma_{112}=t\cdot\gamma_{16},\ \gamma_{113}=t^2\cdot\gamma_{11},\ \gamma_{114}=t^2\cdot\gamma_{12},\ \gamma_{115}=t^2\cdot\gamma_{13},\ \gamma_{116}=t^2\cdot\gamma_{14}$$

$$\gamma_{117}=t^2\cdot\gamma_{15},\ \gamma_{118}=t^2\cdot\gamma_{16},\ \gamma_{119}=t^3\cdot\gamma_{11},\ \gamma_{120}=t^3\cdot\gamma_{12},\ \gamma_{121}=t^3\cdot\gamma_{13},\ \gamma_{122}=t^3\cdot\gamma_{14},\ \gamma_{123}=t^3\cdot\gamma_{15}$$

$$\gamma_{124}=t^3\cdot\gamma_{16}$$

$$\gamma_{125}=-\gamma_{11},\ \gamma_{126}=-\gamma_{12},\ \gamma_{127}=-\gamma_{13}$$

$$\gamma_{21}=\frac{\partial y_M^7}{\partial X_S(t)},\ \gamma_{22}=\frac{\partial y_M^7}{\partial Y_S(t)},\ \gamma_{23}=\frac{\partial y_M^7}{\partial Z_S(t)},\ \gamma_{24}=\frac{\partial y_M^7}{\partial \varphi_S(t)},\ \gamma_{25}=\frac{\partial y_M^7}{\partial \omega_S(t)},\ \gamma_{26}=\frac{\partial y_M^7}{\partial k_S(t)},\ \gamma_{27}=t\cdot\gamma_{21}$$

$$\gamma_{28}=t\cdot\gamma_{22},\ \gamma_{29}=t\cdot\gamma_{23}$$

$$\gamma_{210}=t\cdot\gamma_{24},\ \gamma_{211}=t\cdot\gamma_{25},\ \gamma_{212}=t\cdot\gamma_{26},\ \gamma_{213}=t^2\cdot\gamma_{21},\ \gamma_{214}=t^2\cdot\gamma_{22},\ \gamma_{215}=t^2\cdot\gamma_{23},\ \gamma_{216}=t^2\cdot\gamma_{24}$$

$$\gamma_{217}=t^2\cdot\gamma_{25},\ \gamma_{218}=t^2\cdot\gamma_{26},\ \gamma_{219}=t^3\cdot\gamma_{21},\ \gamma_{220}=t^3\cdot\gamma_{22},\ \gamma_{221}=t^3\cdot\gamma_{23},\ \gamma_{222}=t^3\cdot\gamma_{24},\ \gamma_{223}=t^3\cdot\gamma_{25}$$

$$\gamma_{224}=t^3\cdot\gamma_{26}$$

$$\gamma_{225}=-\gamma_{21},\ \gamma_{226}=-\gamma_{22},\ \gamma_{227}=-\gamma_{23}$$

Appendix II. The structure of observation equations